Assessment of High-Resolution Methods in Hypersonic Real-Gas Flows

Shiroshana Tissera

Submitted for the Degree of Ph.D.

Fluid Mechanics and Computational Group

School of Engineering

Cranfield University

Cranfield, UK

Cranfield University

School of Engineering

PhD

Year: 2010

Shiroshana Tissera

Assessment of High-Resolution Methods in Hypersonic Real-Gas Flows

Professor Dimitris Drikakis (First Supervisor) and

Dr Vladimir Titarev (Second Supervisor)

July 2010

Acknowledgements

I wish to thank many individuals who helped me over the years directly and indirectly, and without their help, advice, and support, the completion of this thesis would not be a rewarding experience. Firstly, I would like to thank Professor Drikakis for his advice and supervision, for encouraging me to take on additional challenges, patience, and endless enthusiasm for the undertaking, and development of hypersonic flow modelling. I am also extremely grateful to my second supervisor, and friend Dr Vladimir Titarev, for his insight into all things numerical, support, constructive criticism, and general chats about tea. I would also like to thank Dr Marie-Claude Druguet, and Dr I Nompelis for answering my endless questions, and their advice about the double-cone flow all the way from the USA.

Furthermore I would also like to thank Professor John Stollery, Andrew Mosedale, Evgeniy Shapiro, Marco Hann, Ben Thornber, and Les Oswald for their help, support, and advice about the hypersonics, coding, and numerical issues. Thanks to my friends at Cranfield, Ranga-Dinesh, Maximus (Max), Philip, Inok, and Ioannis for all the fruitful discussions we had, and for all their help. I am also grateful to my friends at CMDC, and specially mention Ms Jo Price, and Mr Stewart Elsmore for their support and understanding.

On a more personal note, I would like to thank my friends Ranal and Amal for just being there, and making the life in London (and UK) a more enjoyable one. Himali, thank you for feeding me all things Sri Lankan, whenever I visit. I must also mention my buddy Dilan for the endless discussions about everything, inspiration and just making me see things in a different light. I also would like to express my deepest gratitude to Nancy for her endless support, cooking me the most delicious mousaka, and pasta, making me better acquainted with all things Greek, for great companionship, and simply making the past few months most memorable.

Finally, a great *thankyou* to my Mother, Father, and Brother. I would like to dedicate this thesis to my Parents for their enormous support, and constant encouragement and belief that I would always make the right choice. Simply everything was, and would be possible only because of you.

Abstract

The interest in hypersonic flow phenomena has peaked in recent years where number of experimental and computational work has been carried out. The Computational Fluid Dynamics (CFD) is fast becoming an invaluable tool to investigate compressible hypersonic flow phenomena that are extremely complex in nature. Mathematical models employed to describe complex physical phenomena that take place at hypersonic speeds inherit varying degrees of accuracy and reliability. Therefore, further studies, numerical and experimental, are needed to clarify and improve these models. Numerical computation is one of the tasks that are vital in the overall hypersonic flow research effort.

This work investigated the applicability and performance of higher resolution methods to simulate high enthalpy real gas flows. Furthermore, gas-surface interaction and ablation effects are also investigated. In order to achieve the set task, it is imperative that the numerical code (CNS3D) used is equipped with necessary numerical and physical models to tackle flow behaviour typically unique to hypersonic flow. Therefore, the implementation of mathematical models that describe the real gas phenomena, such as vibrational effects, chemical dissociation, diffusion, and high enthalpy effects, has been carried out.

The test cases, the HB-2 flare and the double-cone have been considered for the purposes of verification and validation. The experimental data for heat transfer and pressure are compared with numerical predictions to assess the behaviour of modified CNS3D overall and each numerical scheme with regards to reconstruction methods. The overall agreement between the predicted results for both cases and the experimental data is satisfactory. The stagnation point values of pressure and heat flux for HB-2 flare testcase at varying Mach numbers from 5 to 17.8 has been established; these values are expected aid future validation efforts. It was also found that very high-order schemes, such as WENO 5^{th} and 9^{th}-order methods, may provide slightly better results for free stream Mach numbers less than 10; however, there are no obvious benefits over second-order methods for Mach numbers greater than 10. Furthermore, it has been substantiated that increasing order of accuracy compared to increments in the grid resolution is much more effective way of gaining accuracy in the case of real gas flows.

CONTENTS

LIST OF FIGURES

Nomenclature

A_{ir} curve fit constants for evaluating $K_{eq,r}$

A_s constant for calculating τ_s^{MW}

a frozen speed of sound

a_{sr} nondimensional parameter for collision of species s and r

C_s mass fraction of species s

C_p^s specific heat capacity at constant pressure for species s, J/kg-K

$C_{p,r}^s$ specific heat capacity at constant pressure for species s for rotational enthalpy, J/kg-K

$C_{p,t}^s$ specific heat capacity at constant pressure for species s for translational enthalpy, J/kg-K

$C_{p,v}^s$ specific heat capacity at constant pressure for species s for vibrational enthalpy, J/kg-K

C_v^s specific heat capacity at constant volume for species s, J/kg-K

$C_{v,r}^s$ specific heat capacity at constant volume for species s for rotational energy, J/kg-K

$C_{v,t}^s$ specific heat capacity at constant volume for species s for translational energy, J/kg-K

$C_{v,tr}^s$ specific heat capacity at constant volume for species s for translational-rotational energy, J/kg-K

c_s mass fraction of species s

$\bar{c}_s$ average molecular velocity of species s, m/s

D_s effective diffusion coefficient for species s,m^2/s

$\hat{D}_s$ average vibrational energy per unit mass of molecule s and created or destroyed at rate $\dot{w}_s$, J/kg

$\tilde{D}_s$ dissociation energy per unit mass of molecules s, J/kg or eV

D_{sr} binary diffusion coefficient for species s and r, m^2/s

E total energy per unit mass of the mixture, J/kg

E total vibrational energy per unit mass of the mixture, J/kg

$E_{b,r}$ activation energy for backward reaction r, J

$E_{f,r}$ activation energy for backward reaction r, J

$e_{v,s}$ vibrational energy per unit mass of species s, J/kg

H total enthalpy per unit mass of mixture, J/kg

h_s enthalpy per unit mass of species s, J/kg

$h_{s,o}$ enthalpy of formation of species s, J/kg

$h_{v,s}$ vibrational enthalpy per unit mass of species s, J/kg

$K_{eq,r}$ equilibrium constant for reaction r

$k_{b,r}$ backward reaction rate coefficient for reaction r, units in cgs

$k_{f,r}$ forward reaction rate coefficient for reaction r, units in cgs

M_∞ free stream Mach number

M_s molecular weight of the species s $kg/kg-mole$

m_s mass of species s per particle, kg

N_r number of reactions in chemical kinetic model

$n_{b,r}$ exponent of temperature in preexponential term for backward reaction, r

$n_{f,r}$ exponent of temperature in preexponential term for forward reaction, r

p pressure, Pa

p_s partial pressure due to species s, Pa

Q_{rad} radiative energy transfer rate, J/m^3-s

$\bar{R}$ universal gas constant, 8314.3 $J/kg-mole-K$

$R_{b,r}$ backward reaction rate for reaction r, $kg-mole/m^3-s$

$R_{f,r}$ forward reaction rate for reaction r, $kg-mole/m^3-s$

Re_m local Reynolds number, $1/m$

T_∞ free stream temperature, K

T translational-rotational temperature, K

T_d rate-controlling temperature for dissociation reactions, K

T_{ref} reference temperature for thermodynamic relations, K

T_v vibrational temperature K

T_w wall temperature K

t time, s

U velocity components taken at the cell centre, m/s

u velocity component in x-direction, m/s

v velocity component in y-direction, m/s

w velocity component in z-direction, m/s

$\dot{w}_s$ mass rate of production of species s per unit volume, $kg/m^3 - s$

y_s mole fraction of species s

x Cartesian coordinates

y Cartesian coordinates

z Cartesian coordinates

Greek Symbols

$\alpha_{s,r}$ stoichiometric coefficient for reactants in reaction, r

$\beta_{s,r}$ stoichiometric coefficient for production in reaction, r

γ_s molar concentration of species s, $kg - mole/m^3$

$\Delta_{sr}^{(1)}$ modified collision integrals for species s and r, $m - s$

$\Delta_{sr}^{(2)}$ modified collision integrals for species s and r, $m - s$

κ Boltzmann's constant, 1.380622×10^{-23} J/K

ξ curvilinear coordinate direction; normal to the body

ζ curvilinear coordinate direction; along the body

η curvilinear coordinate direction; normal to the ξ and ζ plane

η_r frozen thermal conductivity for rotational energy, $J/m-s$

η_t frozen thermal conductivity for translational energy, $J/m-s$

η_v frozen thermal conductivity for vibrational energy, $J/m-s$

μ mixture viscosity, $N-s/m^2$

ρ mixture density, kg/m^3

ρ_∞ free-stream mixture density, kg/m^3

ρ_s free-stream mixture density, kg/m^3

$\langle\tau_s\rangle$ translational-vibrational energy (T-V) relaxation time

$\Omega_{sr}^{(1,1)}$ collision integral for species s and r

$\Omega_{sr}^{(2,2)}$ collision integral for species s and r

Subscripts

b backward rate quantity

f forward rate quantity

p at a constant pressure

ns number of species

mol number of molecules

Acronyms

CNS3D Compressible Navier Stokes 3D

DSMC Direct Simulation Monte Carlo

LHS Left Hand Side

RHS Right Hand Side

TPS Thermal Protection System

TPM Thermal Protection Material

US United States

UK United Kingdom

CHAPTER 1

Introduction to Non-equilibrium Hypersonic Flow and Review of Related Research

Believe nothing, no matter where you read it,
or who said it, no matter if I have said it,
unless it agrees with your own reason,
and your own common sense.

Lord Gautama Buddha (Founder of Buddhism; Lumbini, 536 BC)

1.1 Historical Perspective

Over the years the typical cruising speed and altitude of an aeroplane has increased from a mere 35 *mph* and barely taking off in 1903 to 1200*mph* at 60000*ft* in the 1960s. The highly classified X-planes project initiated by the United States used new technologies to design manned airplanes that reached speeds past Mach number seven. The experimental Hyper-X$(X-43)$ unmanned space vehicle (see Figure 1.1) powered by a scram-jet made history by achieving sustained atmospheric flight at Mach number 10 for 10*s*. Furthermore, space race between the United States and the Soviet Union fuelled the desire to design reusable hypersonic vehicles that can withstand extreme conditions during re-entry. The highest Mach number achieved by a manned flight is held by the space shuttle with Mach number 25 re-entry from a 200-mile low earth orbit.

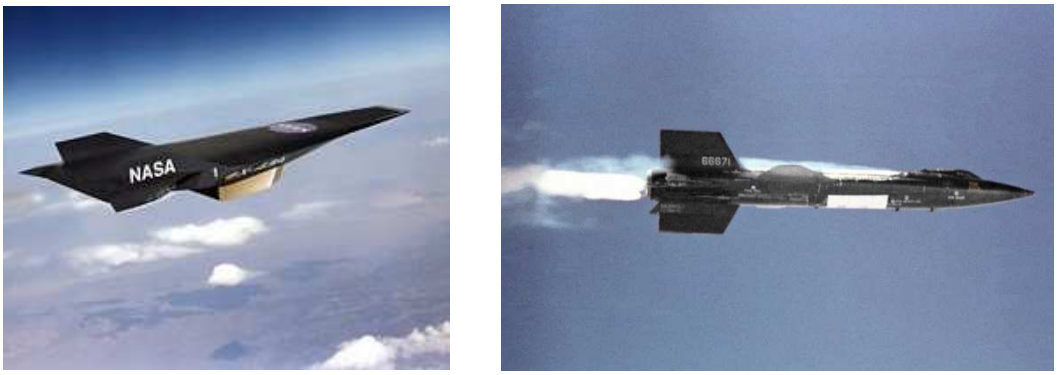

(a) X-43A (b) X-15

Figure 1.1 — *NASA Hypersonic Aerospace Vehicles.*[145]

The costs involved in meeting the design requirements for high speed aerospace vehicles typically tend to be extremely high. One of the key reasons for this dearer price tag is the lack of understanding of the extreme physical conditions present within the flow field around the hypersonic vehicle. This means that large safety factors had to be incorporated into the design of vital components such as the Thermal Protection System (TPS). The additional weight inevitably makes such vehicles commercially non-viable as it results in payload reduction. All these factors pointed towards the conclusion that the costs associated with hypersonic vehicle design far outweigh the immediate benefits they bring, and most projects were discontinued.

The interest in hypersonic flow phenomena has been rekindled in recent years and additional experimental and computational work has been carried out. This is a useful trend that will lead to identifying the factors affecting the complex flows that surround hypersonic objects [2,9,11,76,138,143], though this is not straight-forward. Due to the complex physical processes that take place at high Mach numbers, the experimental methods are still difficult to conduct and obtain accurate results. The advances have been much greater in the numerical field; however, the physical and chemical models used in the simulations are inadequate to fully describe the physics at high Mach numbers.

Computational fluid dynamics (CFD) is a strategic tool that continues to reduce the design and development time required for aerospace vehicle design [108]. The accumulative effect of reasons, such as increased robustness in CFD codes, lower computational costs, improvement in hardware as well grid generation, and easy to use post processing tools, has provided the necessary environment for increase in popularity and rapid growth of CFD [108]. One of the main objectives of hypersonic CFD research is to classify physical and numerical models that have been validated, and could amply characterise the various extreme flow phenomena with optimum accuracy [12]. From the research carried out so far, it is evident that this is a mammoth task proving to be extremely difficult. Therefore, continuation of hypersonic flow research is essential to clarify many unknowns, which would assist in designing new, even faster, efficient and safe aerospace vehicles that will propel mankind into the future [11,32,126].

1.2 High Temperature Compressible Flows

Typically hypersonic flow regime is identified as those flows, where Mach number is greater than 5. Phenomena such as viscous interaction, high temperature, and low density effects have a more dominating influence within the hypersonic regime. In addition, with the increase in Mach number, shock wave stand-off distance becomes much smaller. Also, the thickness of the boundary layer becomes relatively large compared to the shock layer. The shock layer is defined as the region between the bow shock wave and the surface of the hypersonic object. Within the boundary layer kinetic energy is transferred into internal energy generating very high temperatures, which trigger dissociation and even ionisation of molecules. The chemically reacting flow dominates the shock layer, forcing the assumption of perfect gas and the familiar observation of $\gamma = \frac{C_p}{C_v} = 1.4$ to be invalid [2,20]. Therefore, a flow field where phenomena such as

vibrational and chemical excitation, dissociation, ionisation, adsorption and radiation prevail, is referred to as a ***high temperatures gas*** or ***real gas*** (see Figure 1.2)[2,9].

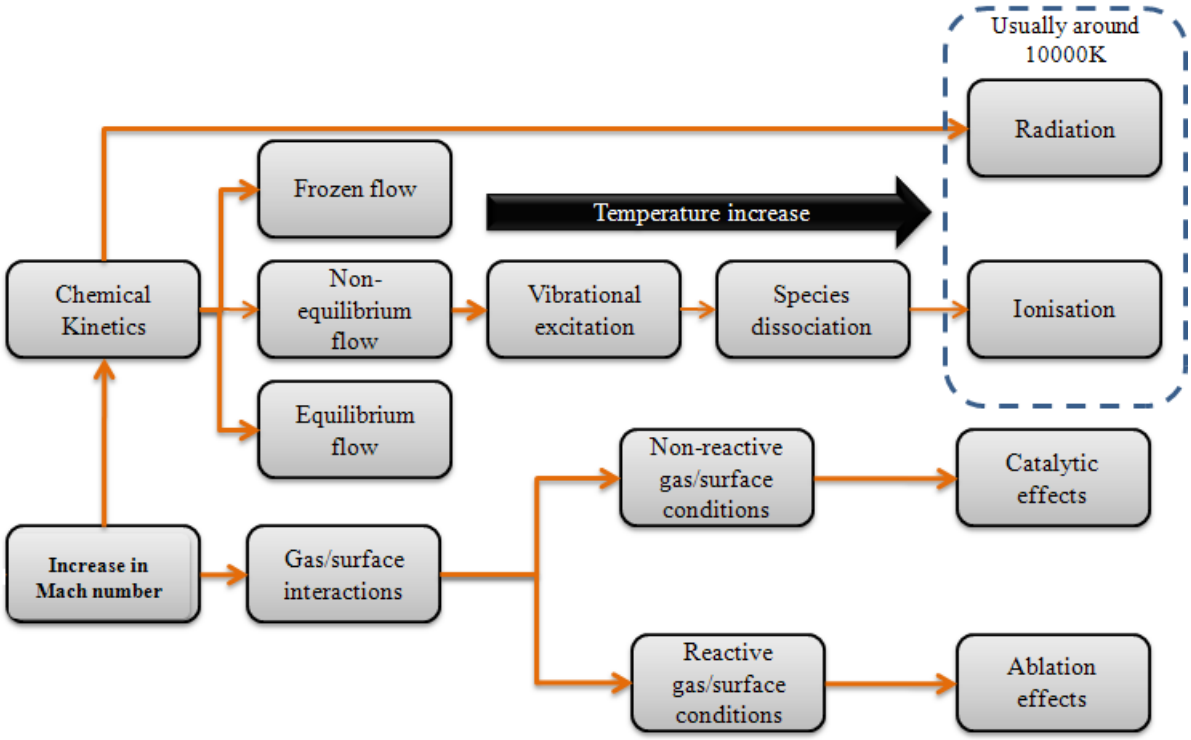

Figure 1.2 — *Hypersonic flow phenomena that may be present within the flow.*

The non-equilibrium effects that may be present during real gas conditions is the primary focus of this work. To make the investigation easier, it is convenient to introduce a scale by which the flow can be classified into categories. The Damköhler number (*Da*) is such a scale, where *Da* is defined as t_f/t_c; the flow time, t_f, is defined as the characteristic time taken by the fluid element to transverse the flow domain; the characteristic time for the chemical reaction or vibrational energy to approach equilibrium is represented by t_c[2]. If the speed of the chemical reactions is higher than the speed at which the fluid element moves through the flow field, the flow is considered to be in *equilibrium* and $Da \gg 1$[129,138]. If the typical characteristic time scales associated with processes such as chemical reactions to reach equilibrium is orders of magnitude higher than the characteristics flow time, that is $Da \ll 1$, then the gas is typically referred to as being *frozen*. In between these two extremes, *non-equilibrium* flow takes place.

The *non-equilibrium* flow occurs when an insufficient number of collisions take place when

flow particles pass through a strong shock wave or undergo a rapid expansion during the time period of the fluid motion. The high temperature chemically reacting flow features can have a dramatic influence over the aerodynamic characteristics and must be taken into account during the design and development stage of aerospace vehicles[128,138]. Figure 1.3 presents the various effects of high speed flow phenomena coming into effect at different speeds and altitudes.

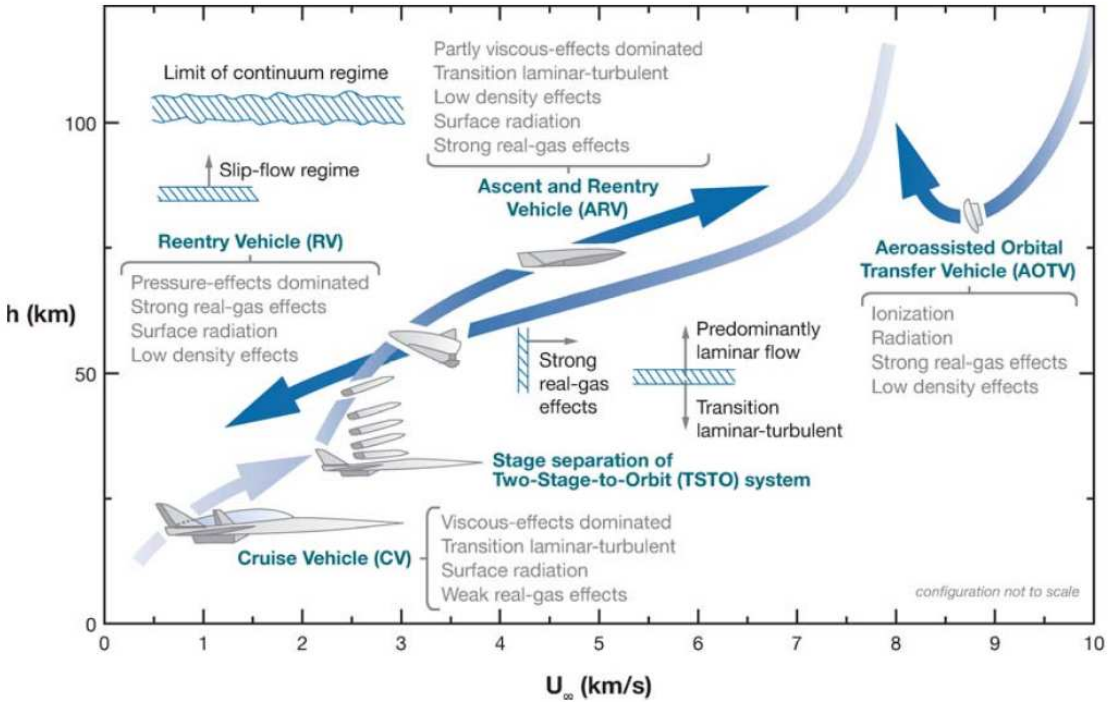

Figure 1.3 — *Trajectories of various space vehicles.* *after* [11]

The chemical species within the high temperature flow field not only react with each other, but also interact with the TPS. It is entirely possible for the wall material to aid or even take part in chemical reactions taking place occurring near vicinity of the surface. Gas-surface interactions are an important aspect of hypersonic flows as it can influence the flow physics to change drastically with potentially undesired consequences.

Gas-surface interaction in the form of catalytic recombination aids the reactions, such as two Oxygen atoms O, coming together to form an Oxygen molecule O_2. The effect of the catalyst alters, or in this case reduces the activation energy of the reaction and aids the process without taking part. The reactive flow interaction would defer depending on state of oxidisation of the TPS material. A number of catalytic models are available in the literature[3,8,141] with a varying

degree of accuracy to be applied at specific conditions to increase the effectiveness of the (CFD) simulations[1,4,62,130,136,155].

Recombination reactions are usually classified as exothermic and as a result, a fully catalytic wall would significantly increase the heat transfer to the wall. However, in most cases the wall can be classified as partially catalytic[62,67,142]. Earlier designs of TPS assumed fully catalytic conditions and used very high safety factors during design to compensate. This practice may be justified for low cost non-reusable vehicle design. However, more accurate estimations of heat transfer to the surface are essential for the design of the space shuttle and other reusable aerospace vehicles in order to save weight while providing optimum safety to the crew and vital components. With the involvement of CFD, and by employing a catalytic wall boundary model for materials such as SiO_2 it is possible to achieve a better estimate than previously possible.

If the surface is considered to be ablating, surface material actively reacts with the species within the flow. The process of ablation results in mass loss from the surface which creates ablation-product layer in the immediate vicinity of the TPS. This reduces the conductive heat flux from the hotter regions in the flow field reaching the wall. It is important that accurate predictions are made regarding the thickness and the thermo-chemical state of the ablation-product layer which would assist in estimating the total heat transfer to the wall. The radiation fluxes directed towards the wall are also partly absorbed by the ablation-product layer[28,60,112,131,159]. Also, there are models available to describe ablation over the surface considering variables such as the materials and temperatures involved[17]. These models have been developed under various assumptions and predict ablation effects with varying degrees of accuracy[61,117,137]. Further details of catalytic and ablating wall effects will be discussed in chapter 6.

1.3 Review of Related Research

The outcome of studies conducted via the means of computational methods is an integral part of the validation process. The ultimate goal of these studies is to improve the existing models (numerical or physical) to duplicate the conditions in reality. The calculated results are compared with data obtained via the experimental method to ascertain the validity of the mathematical models. These avenues of investigation have been used by many researchers to explore various

aspects of hypersonic flow; several examples of such attempts are presented within the course of this thesis.

The experimental data for a number of test cases conducted under a range of conditions are available in the literature[80,81,86,105,110,116,124]. These included research areas such as real gas flows[105,123], laminar hypersonic viscous-inviscid interactions[73], shock-shock interactions[75], and boundary layer instabilities and transition[96,97,140]. The experiments were carried out using a range of flow conditions across laminar, transitional and turbulent regimes with varying Mach numbers and angles of attack. For instance, the investigators Holden and Wadhams(2001) carried out extensive investigations into high speed flows using the double-cone configuration under laminar flow conditions in the shock tunnels at Calspan University Buffalo Research Center (CUBRC). This was part of an extensive validation study carried by the Research Technology Organisation (RTO) Advanced Vehicle Technology (AVT), a Working Group; designated number 10 (NATO-RTO-AVT-10). One of the goals of carrying out such experimental work has been the construction of a database containing experimental measurements for well-defined model configurations[78,79,157].

The increase in computational work also has been a significant factor in supporting the experimental data. Such research has explored numerous physical and numerical models for hypersonic flows. On the physical side, this has required simulations to range from a typical perfect gas model to a multi-species, high temperature, chemically reacting thermally perfect gas model, including chemical and vibrational non-equilibrium relaxation. Phenomena such as radiation[51,59], ionization[65,72], and with magneto-hydrodynamics[83] have also been included in some studies to investigate the properties of flow regimes under continuum and rarefied conditions[10,53,138]. In addition, dissociation[50], recombination[64], and vibrational relaxation[20,83] are also taken into consideration through the use of vibrational temperature[15,19,57,128,129]. Determining the physics over a given flow regime and geometry is an iterative process that continues to develop alongside these physical models.

A wide range of numerical methods were also employed in these studies. Riemann solvers, such as ROE and HLLC [†], are most commonly used[56,84,132,133,139]. However, there have been studies done in the past which employed flux vector splitting and hybrid schemes[16,43]. These studies have reported that[25,43] second-order accurate modified Steger-Warming methods and hybrid schemes are quite effective for the purposes of simulating hypersonic flow problems

[†]Further details of the HLLC Riemann solver will be explained in detail in chapter3

under perfect and non-equilibrium assumptions. Most of these problems were investigated under laminar conditions and with little or no turbulent effects. The time integration scheme used depends mostly on the type of problem, and more specifically on the resolution of the grid. The explicit multi-stage Runge-Kutta scheme was widely utilised which improved accuracy beyond the typical second order[88,89,158] and has been coupled with a multi-grid method as an acceleration scheme[91]. In addition to the explicit approach, implicit time marching schemes have also been used[43,48,119]. To achieve convergence over grids with very high resolution, it is imperative that either a fully implicit scheme or an explicit scheme coupled with an acceleration technique should be used, as it would be impractical to use simple explicit schemes and retain any hope of achieving convergence[48].

With regards to the accuracy of reconstruction, methods used previously range from second to fifth order. Typical second-order reconstruction methods are the Monotone Upstream-centred Schemes for Conservation Laws (MUSCL). These are formulated so as to gain optimal accuracy in smooth regions of the flow while being limited in the presence of discontinuities through non-linear limiting functions. A number of limiting functions are presented in the literature[38,103] and many have been used to investigate hypersonic problems[144].

Another approach to construct high-order methods is provided by the Essentially Non-Oscillatory (ENO) method[70]. Third-order ENO schemes were used by[29] to study the effects of shockwave-free stream interactions of transient hypersonic flow. The ENO methods have not found widespread use, partly because they were quickly superseded by the weighted ENO (WENO) schemes[85]. Fifth-order WENO schemes have been employed to study the boundary layer over a blunt cone [88,89,125,158]. These studies included variants of the WENO scheme, such as a preconditioned (P-WENO) scheme for solving the Navier-Stokes equations consisting of a 1^{st}-order component in conjunction with the preconditioned Roe solver and a 3^{rd}-order component based on a preconditioned WENO scheme.

The standard WENO reconstruction of Jiang and Shu[85] (WENO-JS) has been successfully applied to many problems featuring discontinuities[7,85,107,150]. There have also been efforts to improve the efficiency and robustness of the original WENO scheme. Henrick *et al.*[74] introduced the mapped WENO (WENO-M) scheme, which was capable of achieving optimal order of accuracy near critical points. More recently, Borges *et al.*[18] presented a new WENO scheme (WENO-Z) by implementing higher-order smoothness indicators with a new set of non-oscillatory weights which gives less dissipation and higher resolution than the original

WENO-JS scheme. The results obtained for the fifth-order reconstruction for this scheme are as sharp as the ones obtained using the mapped WENO (WENO-M) scheme with the computational cost being lower when the mapping is not performed.

Oliveira *et al.*[125] used the hypersonic double-cone flow under perfect gas conditions to validate the modified weighted compact scheme (MWCS) which is very similar to WENO. It was observed that MWCS outperforms WENO scheme by achieving sixth order accuracy of reconstruction in the smooth regions and forth order near the shocks. In contrast WENO fifth-order achieves only fifth-order in the smooth regions and only third-order near discontinuities. Even though flow features are not predicted accurately, the results obtained are encouraging and further development is under way[†].

1.4 Aim and Structure of the Thesis

*The **aim** of this thesis is to investigate the behaviour and effectiveness of the high-order methods when utilised to simulate hypersonic flow phenomena.* Using the test cases HB-2 and double-cone flow, mentioned below, it has been attempted to ascertain the functionality of high-resolution and high-order schemes within the reconstruction element of the numerical schemes. The use of these techniques in non-equilibrium hypersonic flows to resolve HB-2 and double-cone flows with ablating wall boundary conditions is state of the art. Furthermore, to the best of this author's knowledge, this is one of the first computation studies that has been carried out at low and high enthalpy conditions for the HB-2 flare test case and the numerical results obtained have been referred to as *ground-breaking*[‡].

The current investigation employs the compressible Navier-Stokes solver (CNS3D) developed over a number of years by Drikakis *et al*[6,162]; the code has been validated for high Mach number ideal gas flows.

The main aim of this work has been to facilitate the application of higher-order methods in non-equilibrium hypersonic flow, in the way of implementing numerous physical models and additional governing equations. Therefore, to extend the capability of CNS3D to handle non-equilibrium high temperature flows at high Mach numbers, during the course of this study,

[†]Further details of MUSCL and WENO reconstruction techniques are presented in chapter3

[‡]Personal communication: Dr Grant Palmer, Associate Editor, Journal of Spacecraft and Rockets, Email-Grant.E.Palmer@nasa.gov

additional equations and models describing chemical dissociation, surface chemistry, thermal diffusion, vibrational effects and other high temperature phenomena have been implemented

The need for the additional terms arises from the complex phenomena that become dominant due to high energy present within the flow. Various effects, such as diffusion, thermal and chemical non-equilibrium, and the activation of additional energy modes, are not present or dominant in a typical ideal gas flow. Further details of the models and equations implemented are presented in the following chapters. Furthermore, CNS3D has been compared with the commercial software FLUENT; the objective of this study was to establish and compare the capabilities of both codes.

1.4.1 Test Cases

The present investigation employed two test cases, namely blunted-cone-cylinder-flare designated HB-2 and double-cone, for validation purposes. A brief description of these test cases is available below. Both double-cone and HB-2 are regarded as excellent test cases for code validation purposes.

Double-cone Flare

Although the geometry of the double-cone appears simple enough (see Figure 1.4), it gives rise to complex flow features including strong viscous-inviscid and shock-shock interactions leading to boundary layer separation[24,48,119]. The interaction between the shock generated by the first cone and the strong detached shock formed by the second cone yields a transmission shock which impinges on the wall, downstream of the junction of the two cones. The adverse pressure gradient created as a result of these interactions forces the boundary layer to separate while forming its own shock, which in turn interacts with the triple point of the existing shocks. While this process continues, the territory of the separation region oscillates until the flow reaches the steady state. Downstream of the point where transmitted shock impinges and along the surface of the second cone a supersonic jet, exhibiting isentropic compressions and expansions conditions, is formed. In addition, immediately behind the triple point a subsonic region is also materialised. When the steady shear layer cannot eject enough mass, flow tends to become unsteady, leading to oscillations[48,93].

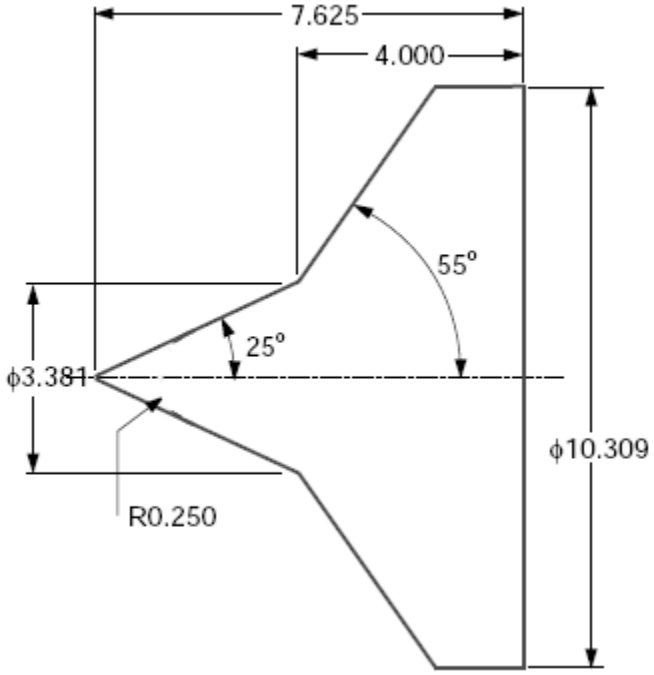

Figure 1.4 — *Double-cone geometry.*

The double-cone test case was used by Candler[25], Nompelis[119,121], Druguet[48] and Gnoffo[57], to investigate low and high enthalpy flows involving real gas effects and related phenomena using computational methods. Also, comparison studies between the use of Navier-Stokes equations and the Direct Simulation Monte Carlo (DSMC) codes were carried out by Inger and Moss[14,83]. Nompelis *et al*[119,122,123] used a second-order accurate modified Steger-Warming method to simulate the double-cone flow, under laminar flow conditions to examine the effects of real-gas chemistry on hypersonic flows with laminar viscous-inviscid interactions. The work was carried out to establish quality high-enthalpy hypersonic experiments for validation of air chemistry models. It was concluded that a distinct advantage could be gained by characterising the flow through numerical simulation over traditional experimental methods.

The size of the separation zone is dictated by the shock interaction and boundary layer growth and it is essential that the grid utilised is able to adequately capture these effects. The size of the separation zone is the primary indicator of characteristics with the fluid flow over the double-cone. For instance, Druguet *et al.*[48] observed that making alterations to aspects such as forward chemical reaction rate or angle of attack would alter the size of the recirculation zone. It is also a flow feature that is comparatively easier to track and observe. The length of the

separation zone can be accurately determined experimentally using surface measurements and flow visualisation techniques, which makes the double-cone test case ideal for code validation purposes[25,93]. The axi-symmetric nature double-cone flow allows for a 2D simulation which enables the computational costs to be kept comparatively low[119].

Hypervelocity Ballistic Test Case: HB-2 Flare

The flow features that develop around the HB-2 flare are simpler than the double-cone flow; a typical bow shock originates upstream of the nose region and a separation bubble can form at the cylinder-flare junction. However, the shock interactions are not intrinsically linked. The separation bubble is an indicator of the effect of Reynolds No. on the flow - which only exists for a limited range. As the Mach number is increased, the flow becomes firmly attached to the wall and does not show any signs of separation. The geometry of the HB-2 flare is available in Figure 1.5.

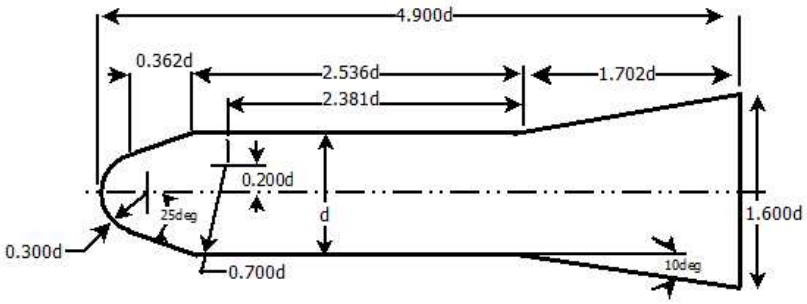

Figure 1.5 — *Schematic of the HB-2 geometry.*

Although only few experiential studies have been carried out, a fair amount of data gathered under axi-symmetric and three dimensional conditions is available in the literature. Most notable are experiments conducted in various wind tunnels such as ONERA in France, to measure quantities such as force coefficients and pressure with varying Mach numbers and angle of attacks[54,63,86,87]. At the current time, there is very limited computational work published for the HB-2[14]. Overall, not as extreme a case as the double-cone, HB-2 flare does form a convenient test case for validation of numerical methods.

1.4.2 Structure of the Thesis

Chapters 2 and 3 map out the aspect of physical and numerical models that have been used to simulate hypersonic flows. The details of the computational experiments carried out in several stages and the results obtained are presented from chapters 4 through 6. The HB-2 flare and the double-cone flow have been investigated under the perfect and real gas assumption in Chapters 4 and 5 respectively. The study includes the 5^{th}- and 9^{th}-order WENO-M schemes as well as the 2^{nd}- and 5^{th}-order MUSCL schemes. Comparisons are performed against experimental data for the wall pressure and heat transfer distributions. It is the first time that several numerical reconstruction schemes have been tested for a range of Mach numbers for the HB-2 geometry.

The runs are carried out on several different structured grid resolutions. This is to compare the improvement made by increasing the grid resolution to that obtained via increasing the order of accuracy. In Chapter 6 the numerical components implemented to describe the ablation effects are validated to further expand the applicability of the computational code. Finally, in Chapter 7 the summary and conclusions of this work have been presented.

1.5 List of Journal and Conference Publications

The results of the thesis have been presented in the following publications

- Tissera.S., Drikakis,D., Birch, T., 'Computational Fluid Dynamics Methods for Hypersonic Flow Around Blunted-Cones-Cylider-Flare', *Journal of Spacecrafts and Rockets*, 2010, 0022-4650 vol.47 no.4 (563-570) doi: 10.2514/1.46722

- Tissera.S., Titarev, V., Drikakis,D.,'Chemically Reacting Flows Around a Double Cone, Including Ablation Effects (Invited)',*AIAA Paper* 2010-1285', 2010.

- Tissera.S., Titarev, V., Drikakis,D., 'Real Gas Hypersonic Flow Modeling Using High Order Methods', *Journal of Spacecrafts and Rockets*, in review, 2010.

  In addition the results obtained via Hypersonic-CNS3D, have been submitted to the joint publication by NATO-RTO-AVT Working group 10 highlighting the joint validation efforts by Knight and Longo (2010).

• Knight,D. and Longo,J., 'Shock Interactions Investigations Associated With AVT-136', *AIAA Paper 2010-1465*, 2010.

CHAPTER 2

Governing Equations for High Temperature Real Gas and Supplemental Models

It is said that despite its many glaring (and occasionally fatal) inaccuracies, the Hitchhiker's Guide to the Galaxy itself has outsold the Encyclopedia Galactica because it is slightly cheaper, and because it has the words

"Don't Panic"

in large, friendly letters on the cover.

The Hitchhiker's Guide to the Galaxy,
Douglas Adams (English science fiction novelist,1952)

2.1 Introduction

In this chapter governing equations and additional formulation for multi-species chemically reacting perfect gas are introduced. The governing equations for a perfect gas, typically referred to as Navier-Stokes (NS) equations, consist of mathematical expressions for conservation of mass, momentum, and energy. Due to the complex mechanisms involved, to adequately describe the flow physics, the governing equations are supplemented with additional terms and formulae.

Instead of the single global continuity equation, s number of species continuity equations are employed, where s is equivalent to the maximum number of species that may be present within the flow field. In this work it has been assumed that nine species N_2, O_2, N, O, NO, C, CO, CO_2, and CN, may be present within the system. This type of set up makes it convenient to keep track of the creation and destruction of species within the flow. In addition, a conservation equation for vibrational energy relaxation is also introduced, which is used to obtain the total vibrational temperature within the flow. To accurately describe the chemical reactions and energy mode relaxation, source terms are introduced which are not available in typical perfect gas formulation. Additional terms are also included in energy and continuity equations to account for diffusion within the flow. It is also assumed that ionisation does not take place during chemical reactions at hyper-velocity.

Assumptions and Limitations

The governing equations and related models that are employed to describe the physics at high temperature non-equilibrium flow field have been constructed on the foundation of several assumptions. These hypotheses allow the researches to employ these models subjected to their inherit limitations.

Can only be applied within the confines of continuity : It is assumed that the flow-fields are accurately described by a continuum formulation. To evaluate if it is plausible, to apply continuum formulation, the dimensionless parameter Kn (Knudsen number) is used. The Knudsen number, defined as *mean-free-path*/*characteristic length scale of the body or flow*,

has be to $\ll 1$. It is required that Kn be much less than one, in order for continuum formulation to function correctly; typically the value of Kn falls within the limits of 0.1-0.001. This, requirement ensures that there is a large number of molecules present within the computational volume; moreover, it is postulated that the statistical variation is minute at any point inside the domain and as a result the continuum description of the viscous fluxes is consistent. Furthermore, with regards to the interaction between the gas and the solid surface of the vehicle, a small Knudsen number ensures that there are a large enough number of collisions of the gas molecules with the wall. This factor leads to the fulfilment of the condition that there is no velocity or temperature slip at the wall.

Separate independent temperatures are employed to describe the thermal state of gas : The internal energy modes, translational, rotational, and vibrational energy are characterised by translational (T_t), rotational (T_r), and vibrational (T_v) temperatures respectively. The temperatures T_t and T_r are assumed to be in equilibrium with each other, hence a single temperature T is used to define both translational-rotational energy modes. The vibrational temperature T_v represents the vibrational energy mode of diatomic species, and in this work only a single vibrational temperature is applied for all diatomic species.

It must be noted that the vibrational states of each diatomic molecular species could be significantly different from each other; therefore, using a single vibrational temperature could cause inaccuracies within the simulations. Park[128] suggests that using the two temperature model is adequate; if chemical reactions are modelled simply using the translational-rotational temperature T_r, then it is possible that the sudden jump in the temperature can cause chemical reactions to proceed much faster than in reality; where, not being able to accurately model the relaxation between each vibrational state has been pointed out as the short coming in the multi-temperature model. Also, simulation of flow field with 9 species and high-order reconstruction techniques alone is computationally very expensive; employing additional vibrational temperatures will increase the burden on the computational resources even more. Due to these reasons, the author has decided against using individual vibrational temperatures corresponding to different species of diatomic molecules.

2.2 Governing Equations in Conservative Form

The NS equations are the backbone of the computation and dictate the shift of gases within the flow filed through the domain in space and time. The flow field is initiated with a set of free stream variables and allowed to evolve in time to yield a solution at steady state. The governing equations of Navier Stokes are presented below.

$$\frac{\partial \boldsymbol{U}}{\partial t}+\frac{\partial \boldsymbol{F}}{\partial x}+\frac{\partial \boldsymbol{G}}{\partial y}+\frac{\partial \boldsymbol{H}}{\partial z}=\frac{\partial \boldsymbol{F}_v}{\partial x}+\frac{\partial \boldsymbol{G}_v}{\partial y}+\frac{\partial \boldsymbol{H}_v}{\partial z}+\boldsymbol{W} \tag{2.2.1}$$

Here, $\boldsymbol{U}$ is the vector of conserved quantities: $\boldsymbol{F}$, $\boldsymbol{G}$, $\boldsymbol{H}$ are the inviscid fluxes; $\boldsymbol{F}_v$, $\boldsymbol{G}_v$, $\boldsymbol{H}_v$ are the viscous fluxes, and $\boldsymbol{W}$ is the source term accounting for chemical reactions and vibrational relaxation. The conserved vector $\boldsymbol{U}$ is expressed as

$$\boldsymbol{U}=\left[\begin{array}{c}\rho_{N_2},\rho_{O_2},\ldots,\rho_{CN},\rho u,\rho v,\rho w,E,E_v\end{array}\right]^T. \tag{2.2.2}$$

The species density is ρ_s and the Cartesian velocity components in x, y, and z are represented by u, v, and w respectively. The total energy and total vibrational energy per unit volume are represented by E and E_v respectively. The total energy of the system can be calculated by adding components of all energy storage modes, namely translational-rotational, kinetic, vibrational, and chemical energy, which are relevant to this study[23].

The total energy per unit volume E is defined as

$$E=\overbrace{\sum_{s=1}^{ns}\rho_s C_v^s T}^{translational-rotational}+\overbrace{\frac{1}{2}\rho U^2}^{kinetic}+\overbrace{E_v}^{vibrational}+\overbrace{\sum_{s=1}^{ns}\rho_s h_s^0}^{chemical}, \tag{2.2.3}$$

The enthalpy of formation is h_s^0 and C_v^s represents the translational-rotational specific heat ca-

pacity at constant volume for a particular species s and U is defined as[23]

$$U = \sqrt{u^2 + v^2 + w^2}. \tag{2.2.4}$$

The vibrational energy E_v, is used to determine the vibrational temperature per species T_v. In this work it is assumed that a single vibrational temperature is present and

$$e_{vs} = \frac{R}{M_s} \sum_r \frac{\theta_{vrs}}{\exp(\theta_{vrs}/T_v) - 1}, \tag{2.2.5}$$

where θ_{vrs} is the characteristic temperature of vibration. The value for θ_{vrs} is listed in Appendix A (also see Candler(1995)[23] and Golovachov(1995)[60]).

$$E_v = \sum_{s=mol} \rho_s e_{vs}. \tag{2.2.6}$$

The value of C_v^s, that is the specific heat capacity at constant volume is defined as

$$C_v^s = C_{v,t}^s + C_{v,r}^s, \tag{2.2.7}$$

where

$$C_{v,t}^s = \frac{3}{2}\frac{\bar{R}}{M_s}, \quad C_{v,r}^s = \frac{\bar{R}}{M_s}. \tag{2.2.8}$$

2.3 Inviscid Fluxes

The inviscid fluxes $\boldsymbol{F}$, $\boldsymbol{G}$, and $\boldsymbol{H}$ in x, y, and z directions respectively can be expressed as follows

$$\boldsymbol{F} = \begin{bmatrix} \rho_{N_2} u \\ \rho_{O_2} u \\ \vdots \\ \rho_{CN} u \\ \rho u^2 + p \\ \rho uv \\ \rho uw \\ (E+p)u \\ E_v u \end{bmatrix}, \quad \boldsymbol{G} = \begin{bmatrix} \rho_{N_2} v \\ \rho_{O_2} v \\ \vdots \\ \rho_{CN} v \\ \rho vu \\ \rho v^2 + p \\ \rho vw \\ (E+p)v \\ E_v v \end{bmatrix}, \quad \boldsymbol{H} = \begin{bmatrix} \rho_{N_2} v \\ \rho_{O_2} v \\ \vdots \\ \rho_{CN} v \\ \rho wu \\ \rho wv \\ \rho w^2 + p \\ (E+p)v \\ E_v v \end{bmatrix}. \tag{2.3.1}$$

The equation of state is used to calculate pressure p and the total pressure is taken as the sum of partial pressures

$$p = \sum_{s=1}^{ns} \rho_s \frac{R}{M_s} T. \tag{2.3.2}$$

The mixture density ρ of species s and the molar fraction y_s can be written as

$$\rho = \sum_{s=1}^{ns} \rho_s, \tag{2.3.3}$$

$$y_s = \frac{\left(\frac{\rho_s}{M_s}\right)}{\sum_{k=1}^{ns} \left(\frac{\rho_k}{M_k}\right)}, \tag{2.3.4}$$

respectively. Here, ns is the number of chemical species within the flow regime, where s and k

represents a particular species.

2.4 Viscous Component

The viscous fluxes $\boldsymbol{F}_v$, $\boldsymbol{G}_v$, and $\boldsymbol{H}_v$ in x, y, and z directions respectively can be expressed as follows:

$$\boldsymbol{F}_v = \begin{bmatrix} \rho D_{\mathrm{N2}} \frac{\partial}{\partial x} y_{\mathrm{N2}} \\ \rho D_{\mathrm{O2}} \frac{\partial}{\partial x} y_{\mathrm{O2}} \\ \vdots \\ \rho D_{\mathrm{CN}} \frac{\partial}{\partial x} y_{\mathrm{CN}} \\ \tau_{xx} \\ \tau_{yx} \\ \tau_{zx} \\ \Theta_x \\ \Phi_x \end{bmatrix}, \quad \boldsymbol{G}_v = \begin{bmatrix} \rho D_{\mathrm{N2}} \frac{\partial}{\partial y} y_{\mathrm{N2}} \\ \rho D_{\mathrm{O2}} \frac{\partial}{\partial y} y_{\mathrm{O2}} \\ \vdots \\ \rho D_{\mathrm{CN}} \frac{\partial}{\partial y} y_{\mathrm{CN}} \\ \tau_{xy} \\ \tau_{yy} \\ \tau_{zy} \\ \Theta_y \\ \Phi_y \end{bmatrix}, \quad \boldsymbol{H}_v = \begin{bmatrix} \rho D_{\mathrm{N2}} \frac{\partial}{\partial z} y_{\mathrm{N2}} \\ \rho D_{\mathrm{O2}} \frac{\partial}{\partial z} y_{\mathrm{O2}} \\ \vdots \\ \rho D_{\mathrm{CN}} \frac{\partial}{\partial z} y_{\mathrm{CN}} \\ \tau_{xz} \\ \tau_{yz} \\ \tau_{zz} \\ \Theta_z \\ \Phi_z \end{bmatrix}, \tag{2.4.1}$$

where

$$\Theta_x = u\tau_{xx} + u\tau_{xy} + u\tau_{xz} + k\frac{\partial T}{\partial x} + k_v\frac{\partial T_v}{\partial x} + \left(\rho \sum_{s=1}^{ns} h_s D_s \frac{\partial y_s}{\partial x}\right), \tag{2.4.2}$$

$$\Theta_y = u\tau_{yx} + u\tau_{yy} + u\tau_{yz} + k\frac{\partial T}{\partial y} + k_v\frac{\partial T_v}{\partial y} + \left(\rho \sum_{s=1}^{ns} h_s D_s \frac{\partial y_s}{\partial y}\right), \tag{2.4.3}$$

$$\Theta_z = u\tau_{zx} + u\tau_{zy} + u\tau_{zz} + k\frac{\partial T}{\partial z} + k_v\frac{\partial T_v}{\partial z} + \left(\rho \sum_{s=1}^{ns} h_s D_s \frac{\partial y_s}{\partial z}\right), \tag{2.4.4}$$

$$\Phi_x = k_v \frac{\partial T_v}{\partial x} + \rho \sum_{s=1}^{ns} h_{v,s} D_s \frac{\partial y_s}{\partial x}, \tag{2.4.5}$$

$$\Phi_y = k_v \frac{\partial T_v}{\partial y} + \rho \sum_{s=1}^{ns} h_{v,s} D_s \frac{\partial y_s}{\partial y}, \tag{2.4.6}$$

$$\Phi_z = k_v \frac{\partial T_v}{\partial z} + \rho \sum_{s=1}^{ns} h_{v,s} D_s \frac{\partial y_s}{\partial z}. \tag{2.4.7}$$

In the Equations 2.4.2 through 2.4.4, y_s denotes the mole fraction, h_s and $h_{v,s}$, the species translational and vibrational enthalpy, and D_s, the effective binary diffusivity of species s, respectively; further details are presented in the subsections 2.4.1 ~2.4.3. The various terms in the governing equations, that represent shear stresses, are defined as

$$\tau_{xx} = \mu\left(\frac{4}{3}\frac{\partial u}{\partial x} - \frac{2}{3}\frac{\partial v}{\partial y} - \frac{2}{3}\frac{\partial w}{\partial z}\right), \quad \tau_{yy} = \mu\left(\frac{4}{3}\frac{\partial v}{\partial y} - \frac{2}{3}\frac{\partial u}{\partial x} - \frac{2}{3}\frac{\partial w}{\partial z}\right),$$
$$\tau_{zz} = \mu\left(\frac{4}{3}\frac{\partial w}{\partial z} - \frac{2}{3}\frac{\partial u}{\partial x} - \frac{2}{3}\frac{\partial v}{\partial y}\right), \quad \tau_{xy} = \tau_{yz} = \mu\left(\frac{\partial u}{\partial y} + \frac{\partial v}{\partial x}\right),$$
$$\tau_{xz} = \tau_{zx} = \mu\left(\frac{\partial u}{\partial z} + \frac{\partial w}{\partial x}\right), \quad \tau_{yz} = \tau_{zy} = \mu\left(\frac{\partial v}{\partial z} + \frac{\partial w}{\partial y}\right).$$

The term μ will be expressed in the subsection 2.4.2.

To describe hypersonic flow features adequately, additional terms are included in the energy conservation and continuity equations. In addition, the expressions used to calculate transport properties also become more complicated. The transport properties as well as thermodynamic relations used in this thesis are defined below.

2.4.1 Transport Properties: Diffusion Terms

The heat conduction by means of diffusion in x, y, and z directions for each species is defined by $\rho D_s \frac{\partial y_s}{\partial x}$, $\rho D_s \frac{\partial y_s}{\partial y}$, and $\rho D_s \frac{\partial y_s}{\partial z}$ respectively. The effective mixture diffusion coefficient D_s

is defined through the binary diffusion coefficient D_{sr} between heavy particles s and r. The molecular weight of species s is denoted by M_s

$$D_s = \frac{\gamma_t^2 M_s \left(1 - M_s \gamma_s\right)}{\sum_{r=1}^{ns} \left(\frac{\gamma_r}{D_{sr}}\right)}, \tag{2.4.8}$$

$$D_{sr} = \frac{\kappa T}{p \Delta_{sr}^{(1,1)}(T)}, \tag{2.4.9}$$

where $r \neq s$ and κ is the Boltzmann's constant. The molar concentration of species s is expressed as $\gamma_s = \frac{\rho_s}{\rho M_s}$ and $\gamma_t = \sum_{s=1}^{n} \gamma_s$. The modified collision integrals $\Delta_{sr}^{(1,1)}(T)$ is defined as

$$\Delta_{sr}^{(1,1)}(T) = \frac{8}{3}\left[\frac{2M_s M_r}{\pi \bar{R} T \left(M_s + M_r\right)}\right]^{\frac{1}{2}} \pi \bar{\Omega}^{(1,1)}. \tag{2.4.10}$$

The collision intregal for species s and r is identified as $\pi\bar{\Omega}^{(1,1)}$.

2.4.2 Transport Properties: Thermal Conduction and Viscosity Terms

The thermal conductivity coefficient for T and T_v is denoted by k and k_v respectively, while μ and ψ represent the viscosity coefficients. The Stokes' hypothesis states that $\psi = -\left(\frac{2}{3}\right)\mu$. The translational thermal conduction coefficient k_t and rotational thermal conduction k_r are defined as

$$k_t = \frac{15}{4}\kappa \sum_{s=1}^{ns} \frac{\gamma_s}{\sum_{r=1}^{ns} a_{sr} \gamma_r \Delta_{sr}^{(2,2)}(T)}, \tag{2.4.11}$$

$$k_r = \kappa \sum_{s=mol} \frac{\gamma_s}{\sum_{r=1}^{n} \gamma_r \Delta_{sr}^{(1,1)}(T)}, \tag{2.4.12}$$

and

$$a_{sr} = 1 + \frac{\left[1 - \left(\frac{m_s}{m_r}\right)\right]\left[0.45 - 2.54\left(\frac{m_s}{m_r}\right)\right]}{\left[1 + \left(\frac{m_s}{m_r}\right)\right]^2}, \tag{2.4.13}$$

where m_s is mass of species s. The vibrational thermal conduction k_v is equal to the rotational thermal conduction[55]. Thus,

$$k_r = k_v. \tag{2.4.14}$$

The total translational-rotational thermal conduction k is defined as

$$k = k_t + k_r. \tag{2.4.15}$$

The mixture viscosity μ can be expressed as

$$\mu = \sum_{s=1}^{n} \frac{m_s \gamma_s}{\sum_{s=1}^{n} \gamma_r \Delta_{sr}^{(2,2)}(T)}, \tag{2.4.16}$$

where modified collision integral $\Delta_{sr}^{(2,2)}(T)$ is expressed as

$$\Delta_{sr}^{(2,2)}(T) = \frac{16}{5}\left[\frac{2M_s M_r}{\pi \bar{R} T (M_s + M_r)}\right]^{\frac{1}{2}} \pi \bar{\Omega}^{(2,2)}. \tag{2.4.17}$$

The tabulated values of the collision integrals $\pi\bar{\Omega}^{(1,1)}$and $\pi\bar{\Omega}^{(2,2)}$ used in the above equations are available in[55,66].

2.4.3 Thermodynamic Relations

The species enthalpy and vibrational enthalpy per unit mass are identified as h_s and $h_{v,s}$ respectively. To obtain the vibrational enthalpy for a species s, the specific enthalpy of species s has to

be evaluated using vibrational temperature T_v and take away the contributions from rotational and translational enthalpies evaluated at T_V and enthalpy of formation $h_{s,o}$ [55,66]

$$h_{v,s}(T_v) = h_s(T) - \left(C^s_{p,t} + C^s_{p,r}\right)\left(T_v + T_{ref}\right) - h_{s,o}. \tag{2.4.18}$$

To calculate the specific enthalpy from the contribution of all energy modes, translational-rotational enthalpies (calculated using translational-rotational temperature), vibrational enthalpy, and enthalpy of formation are added together

$$h_s(T, T_v) = h_{v,s}(T_v) + \left(C^s_{p,t} + C^s_{p,r}\right)\left(T_v + T_{ref}\right) + h_{s,o}. \tag{2.4.19}$$

The tabulated values required to calculate the enthalpies were presented by Gnoffo *et al*[55,66]. The rotational and translational specific heat capacities at constant pressure for species s are denoted as $C^s_{p,r}$ and $C^s_{p,t}$. Here, it is assumed that translational and rotational energy modes are at fully excited state and this approach could only be used with one or two temperature models [154].

2.5 Real Gas Source Term Formulation

The source term W can be expressed as

$$\boldsymbol{W} = \left[\, \dot{w}_{\mathrm{N_2}}, \dot{w}_{\mathrm{O_2}}, \ldots, \dot{w}_{\mathrm{CN}}, 0, 0, Q_{rad}, (Q_{t-v} + Q_{\omega}) \,\right]^T \tag{2.5.1}$$

Here, $\dot{w}_s$ represents the chemical source terms. In addition, Q_{t-v} and Q_{ω} describe the vibrational-translational energy relaxation and vibrational energy reactive source term respectively. For a perfect gas flow, the source term $\boldsymbol{W}$ is identically zero. However, to adequately assess the characteristics of high temperature flows, thermal and chemical non-equilibrium source terms are a necessity [16,55].

2.5.1 Chemical Reacting Source Term

As explained earlier, the environment around an aerospace vehicle is subjected to extreme temperatures at hypersonic speeds. Under these circumstances, the process of mass transfer between species, which is the creation of species s from species r, occurs. The source term $\dot{w}_s$, located in the RHS of the species continuity equation, accounts for the various chemical species present within the system during this process.

The mass production rate $\dot{w}_s$ is

$$\dot{w}_s = \sum_{r=1}^{N_r} \left(\beta_{s,r} - \alpha_{s,r}\right)\left(R_{f,r} - R_{b,r}\right) \ . \tag{2.5.2}$$

Here, the number of reactions considered is denoted by N_r, the stoichiometric coefficients for reactants and products in the r reaction are represented by $\alpha_{s,r}$ and $\beta_{s,r}$ respectively and the forward and backward reaction rates for the r reaction are denoted by $R_{f,r}$ and $R_{b,r}$ respectively. The forward and backward rates $R_{f,r}$ and $R_{b,r}$ respectively are defined as

$$R_{f,r} = 1000 \left[k_{f,r} \prod_{s=1}^{n} \left(0.001 \frac{\rho_s}{M_s} \right)^{\alpha_{s,r}} \right] , \tag{2.5.3}$$

$$R_{b,r} = 1000 \left[k_{b,m} \prod_{s=1}^{n} \left(0.001 \frac{\rho_s}{M_s} \right)^{\beta_{s,r}} \right] . \tag{2.5.4}$$

The reaction rate coefficient data, which is usually available in cgs units in literature, has to be converted to SI (mks) units. The factors 1000 and 0.001 are required for this conversion.

Types of Reactions

Before providing further information about the mechanics of Equation2.5.3 and 2.5.4, it is prudent to inform the reader of the nature of chemical reactions and related issues relevant to this thesis.

When the processes of dissociation and ionisation take place, the following types of reactions are likely to take place within the flow[128]:

Type 1 : Dissociation due to high temperature of O_2, N_2, and NO in the form: $O_2 + M \rightleftharpoons O + O + M$. Here, M is taken as a random body that would be either one of nine heavy particles mentioned earlier.

Type 2 : Zeldovich reactions, which are effectively exchange reactions involving; NO:

$$O + N_2 \rightleftharpoons NO + N,$$

$$NO + O \rightleftharpoons O_2 + N.$$

Type 3 : N_2 would dissociate due to collisions with electrons and is called electron impact dissociation:

$$N_2 + e^- \rightleftharpoons N + N + e^-.$$

Type 4 : Reaction associated with ionisation and the reverse dissociative recombination reaction:

$$N + O \rightleftharpoons NO^+ + e^-,$$

$$O + O \rightleftharpoons O_2^+ + e^-,$$

$$N + N \rightleftharpoons N_2^+ + e^-.$$

Type 5 : O and N undergo electron impact ionisation

$$O + e^- \rightleftharpoons O^+ + e^- + e^-.$$

Type 6 : Charge exchange reactions

$$NO^+ + O \rightleftharpoons N^+ + O_2.$$

The reactions above can occur both ways and are mostly binary in nature. Also, in most applications it is customary to write the equations in the endothermic form.

It is assumed that ionisation is not present ; this is not an unreasonable assumption as the flow fields of interest in this thesis are bounded by this limitation. The mass fractions of ions present within the flow-fields are expected to be negligible. Therefore, reactions of the **Type 3** through **6** will not be present within the system.

Species Interactions

Within the subject matter covered in this thesis, it is possible to witness *heterogeneous* and *homogeneous* reactions. It was necessary to incorporate nine species, in order to consider the flow properties of various test cases investigated in Chapters 4, 5, and 6. Therefore, the reactions that are likely to occur fully in the homogeneous regime, consisting of reactions in air, are identified below. In a typical hypersonic flow, the following reactions are most likely to occur between the chemical species N_2, O_2, N, O, and NO.

$$N_2 + M \rightleftharpoons 2N + M, \tag{2.5.5}$$

$$O_2 + M \rightleftharpoons 2O + M, \tag{2.5.6}$$

$$NO + M \rightleftharpoons N + O + M, \tag{2.5.7}$$

$$N_2 + O \rightleftharpoons NO + N, \tag{2.5.8}$$

$$NO + O \rightleftharpoons O_2 + N, \tag{2.5.9}$$

When a process such as ablation is present, a number of species present within the flow increases as the air begins to react with the surface materials. The chemical reactions presented above in Section 2.5.1 have focused on homogeneous reactions that occur within the flow field; it was assumed that the interaction of particles with the solid wall does not yield any activity in terms of chemistry. To extend this work, the ablation model was implemented in the computational code CNS3D; this allow the heavy particles O_2, O, and N to interact with the wall and form new species. These reactions are referred to as heterogeneous reactions. A complete

description the heterogeneous reactions and validation of the ablating wall model have been presented in Chapter 6.

As the reactions take place, materials from the surface begin to enter into the flow field. The products of such reactions diffuse into the boundary layer and continue to interact with other species present within the flow field. Assuming ablating surface is carbon based and non-charring, the following additional *homogeneous* reactions are most likely to occur[28,112].

$$CO_2 + M \rightleftharpoons CO + O + M, \tag{2.5.10}$$

$$CO + M \rightleftharpoons C + O + M, \tag{2.5.11}$$

$$CN + M \rightleftharpoons C + N + M, \tag{2.5.12}$$

$$N_2 + C \rightleftharpoons CN + N, \tag{2.5.13}$$

$$CO + N \rightleftharpoons CN + O, \tag{2.5.14}$$

$$CO_2 + N \rightleftharpoons CN + O_2, \tag{2.5.15}$$

$$N2 + CO \rightleftharpoons CN + NO, \tag{2.5.16}$$

$$CO + NO \rightleftharpoons CO_2 + N, \tag{2.5.17}$$

$$CO_2 + O \rightleftharpoons CO + O_2, \tag{2.5.18}$$

$$2CO \rightleftharpoons CO + C, \tag{2.5.19}$$

$$CO + N \rightleftharpoons C + NO, \tag{2.5.20}$$

$$CN + O \rightleftharpoons C + NO. \tag{2.5.21}$$

The species M represent a particle that is unchanged during the process but acts as the collision partner in the reaction. The reactions in Equations 2.5.5, 2.5.6, and 2.5.7, and 2.5.10 $\sim$ 2.5.12 are dissociation reactions (**Type 1**); the 2.5.13 through 2.5.21 are exchange reactions (**Type 2**).

Now referring back to Equations 2.5.3 and 2.5.4, the forward and backward reaction rates that

are $k_{f,r}$ and $k_{b,r}$ respectively, govern production and destruction of species by initiating the reactions; they are temperature dependent (see equations 2.5.22 and 2.5.23).

The reaction rates in Equations 2.5.3 and 2.5.4 can be expressed in the modified Arrhenius form in the following manner

$$k_{f,r}(T) = C_{f,r} T_a^{n_{f,r}} \exp(-E_{f,r}/\kappa T_a), \tag{2.5.22}$$

$$k_{b,r}(T) = C_{b,r} T^{n_{b,r}} \exp(-E_{b,r}/\kappa T), \tag{2.5.23}$$

The value of pre-exponential parameter $C_{f,r}$ and $n_{f,r}$, and $E_{f,r}/\kappa$ is available in literature[66]. The tabulated values of $k_{f,r}$ and $k_{b,r}$ are available in A.3. The reaction rates presented in table A.3 are only applicable for flow velocities up to $8km/sec$ (space shuttle re-entry). However, if the calculation required demands flow velocities higher than the specified value, the backward reaction rate can be calculated using the forward reaction rate and the equilibrium constant $K_{eq,r}$. That is

$$k_{b,r} = \frac{k_{f,r}(T)}{K_{eq,r}(T)}, \tag{2.5.24}$$

and using the expression provided by Park (1985)[127,128] $K_{eq,r}$ can be calculated

$$K_{eq,r} = \exp(A_{1r} + A_{2r}Z + A_{3r}Z^2 + A_{4r}Z^3 + A_{5r}Z^4) \tag{2.5.25}$$

In order to provide the reader with a clear notion of the use of Equations 2.5.2 through 2.5.4, they have been employed to calculate the reaction rates and source terms for non-cabon species N_2, O_2, N, O, and NO.

The reaction rates of the reactions presented earlier in Equations 2.5.5 through 2.5.9 can be written as (see Candler (1988)[22])

$$R_1 = \sum_r \left[-k_{f_{1r}} \frac{\rho_{N_2}}{M_{N_2}} \frac{\rho_r}{M_r} + \frac{\rho_N}{M_N} \frac{\rho_N}{M_N} \frac{\rho_r}{M_r} \right], \tag{2.5.26}$$

$$R_2 = \sum_r \left[-k_{f_{2r}} \frac{\rho_{O_2}}{M_{O_2}} \frac{\rho_r}{M_r} + k_{b_{2r}} \frac{\rho_O}{M_O} \frac{\rho_O}{M_O} \frac{\rho_r}{M_r} \right], \tag{2.5.27}$$

$$R_3 = \sum_r \left[-k_{f_{3r}} \frac{\rho_{NO}}{M_{NO}} \frac{\rho_r}{M_r} + k_{b_{3r}} \frac{\rho_N}{M_N} \frac{\rho_O}{M_O} \frac{\rho_r}{M_r} \right], \tag{2.5.28}$$

$$R_4 = \sum_r \left[-k_{f_4} \frac{\rho_{N_2}}{M_{N_2}} \frac{\rho_O}{M_O} + k_{b_4} \frac{\rho_{NO}}{M_{NO}} \frac{\rho_N}{M_N} \right], \tag{2.5.29}$$

$$R_5 = \sum_r \left[-k_{f_5} \frac{\rho_{NO}}{M_{NO}} \frac{\rho_O}{M_O} + k_{b_5} \frac{\rho_{O_2}}{M_{O_2}} \frac{\rho_N}{M_N} \right]. \tag{2.5.30}$$

Now using the equations 2.5.26 through 2.5.30, it become possible to calculate the source terms described earlier as

$$\dot{w}_{N_2} = M_{N_2} (R_1 + R_4), \tag{2.5.31}$$

$$\dot{w}_{O_2} = M_{O_2} (R_2 - R_5), \tag{2.5.32}$$

$$\dot{w}_N = M_N (-2R_1 - R_3 - R_4 - R_5), \tag{2.5.33}$$

$$\dot{w}_O = M_O (-2R_2 - R_3 + R_4 + R_5), \tag{2.5.34}$$

$$\dot{w}_{NO} = M_{O_2} (R_3 - R_4 + R_5). \tag{2.5.35}$$

Park's Model

Depending on the type of interaction, reaction rates can be functions of different temperatures. In dissociation type reactions between heavy particles rate coefficient is a function of both translational-rotational T and vibrational temperature T_v. Park argues that forward reaction rate k_f is function only of T_a, which is a geometrically averaged temperature between T and T_v.

Therefore, T_a can be defined for all reactions that include molecules as

$$T_a = T_v^q T^{1-q}, \tag{2.5.36}$$

where value of q is between 0.3 and 0.5. The backward reaction rates on the other hand will depend only on translational temperature of impacting particles.

The forward and backward reaction rates used in this thesis were taken from Gupta (1990)[66]. Candler(1988) also presented the coefficients needed to calculate $k_{f,r}$; to calculate the k_b, r the Equation A.3.1 has been used. Both versions are presented in Appendix A.

2.5.2 Internal Energy Relaxation

In this section, the terms that are located on the RHS of the vibrational energy conservation equation, which describes the internal energy exchange processes, are discussed. The energy relaxation between translational and vibrational energy modes, as a result of collisions are taken into consideration via the term Q_{t-v} defined as

$$Q_{t-v} = \sum_{s=mol} \rho_s \left(\frac{e^*_{v_s} - e_{v_s}}{< \tau_s >} \right) \tag{2.5.37}$$

The vibrational energy of species energy per unit mass evaluated at local translational-rotational temperature is denoted by e^*_{vs}. The translational-vibrational energy relaxation time for molecular species s is given by $< \tau_s >$. An expression of vibrational relaxation time valid for a temperature range of 300 K to 8000 K is available in Millikan and White[21,55,128], where

$$p\,\tau_s^{MW} = \frac{\sum_{j=1}^{n} n_j \exp\left[A_s \left(T^{\frac{1}{3}} - 0.015 \mu_{sj}^{\frac{1}{4}} \right) - 18.42 \right]}{\sum_{j=1}^{n} n_j}, \qquad p \quad \text{in atm.} \tag{2.5.38}$$

The reduced molecular weight of the colliding species s and j is represented by μ_{sj}. Also, n_j represents the number density of species j, and p is pressure in atmospheres (atm). The values of A_s for different molecules are available in Appendix A. For temperatures above 8000 K, Park

recommends the use of a different expression for vibrational relaxation time, where τ_s^P

$$\tau_s^P = (\sigma_s \bar{c}_s n_s)^{-1}, \tag{2.5.39}$$

where average molecular velocity is denoted by $\bar{c}_s$ and expressed as,

$$\bar{c}_s = \left(\frac{8kT}{\pi\, m_s} \right)^{\frac{1}{2}}. \tag{2.5.40}$$

The number density and the effective cross section for vibrational relaxation are represented by n_s and σ_s respectively. By combining the two above relationships, it is possible to achieve a more accurate value for $\langle \tau_s \rangle$

$$\langle \tau_s \rangle = \tau_s^{MW} + \tau_s^P. \tag{2.5.41}$$

The vibrational energy per unit mass of the diatomic molecules, which are created or destroyed at a rate of $\dot{w}_s$, is represented as $\hat{D}_s$. The calculation of $\hat{D}_s$ is under some debate and several models exist that could be used for the calculation. In this thesis, the author has selected to define the vibrational energy reactive source term, which was introduced in 2.5.1 as

$$Q_\omega = \sum_{s=mol} \dot{w}_s \hat{D}_s. \tag{2.5.42}$$

where $\hat{D}_s = e_{vs}$.

2.6 Summary

In this chapter, an overview of the physical models required for the investigation of hypersonic flow phenomena has been presented. Clearly, there is a substantial increase in complexity of the models and expressions used in this case, compared to the typical equations encountered in ideal gas flow problems. The implementation of these models has been a challenging task; yet,

stated otherwise, all these models have been implemented in computational code CNS3D. In the next chapter, the numerical models and techniques utilised in this work are presented.

CHAPTER 3

Numerical Methods

Hope is the thing with feathers,
That perches in the soul,
And sings the tune without the words,
And never stops at all.

Emily Elizabeth Dickinson (American Poet,1830 to 1886)

3.1 Introduction

Over the years a wide range of numerical methods has been utilised to investigate hypersonic flow phenomena. In general, the solution is of the Navier-Stokes equations. In this chapter the numerical framework adopted for the investigation of real gas effect under non-equilibrium conditions is discussed. The calculations have been carried out using several space and time discretisation techniques within the block-structured finite volume framework. Instead of a Cartesian coordinate system, a curvilinear coordinate system has been employed for the calculation process.

3.1.1 Governing Equations in Curvilinear Form

All simulations performed in support of this thesis have been carried out using body fitted grids [38]. Therefore, the curvilinear (ξ, η, ζ) coordinate system has been employed for the calculation process in lieu of a Cartesian (x, y, z) coordinate system. The transformed system in curvilinear coordinates is shown below

$$\xi = \xi(x,y,z), \quad \eta = \eta(x,y,z), \quad \zeta = \zeta(x,y,z). \tag{3.1.1}$$

$$\xi_x = J\left(\frac{\partial y}{\partial \eta}\frac{\partial z}{\partial \zeta} - \frac{\partial y}{\partial \zeta}\frac{\partial z}{\partial \eta}\right), \quad \xi_y = J\left(\frac{\partial z}{\partial \eta}\frac{\partial x}{\partial \zeta} - \frac{\partial z}{\partial \zeta}\frac{\partial x}{\partial \eta}\right), \quad \xi_z = J\left(\frac{\partial x}{\partial \eta}\frac{\partial y}{\partial \zeta} - \frac{\partial x}{\partial \zeta}\frac{\partial y}{\partial \eta}\right),$$

$$\eta_x = J\left(\frac{\partial y}{\partial \zeta}\frac{\partial z}{\partial \xi} - \frac{\partial y}{\partial \xi}\frac{\partial z}{\partial \zeta}\right), \quad \eta_y = J\left(\frac{\partial z}{\partial \zeta}\frac{\partial x}{\partial \xi} - \frac{\partial z}{\partial \xi}\frac{\partial x}{\partial \zeta}\right), \quad \zeta_x = J\left(\frac{\partial y}{\partial \xi}\frac{\partial z}{\partial \eta} - \frac{\partial y}{\partial \eta}\frac{\partial z}{\partial \xi}\right),$$

$$\zeta_x = J\left(\frac{\partial y}{\partial \xi}\frac{\partial z}{\partial \eta} - \frac{\partial y}{\partial \eta}\frac{\partial z}{\partial \xi}\right), \quad \zeta_y = J\left(\frac{\partial z}{\partial \xi}\frac{\partial x}{\partial \eta} - \frac{\partial z}{\partial \eta}\frac{\partial x}{\partial \xi}\right), \quad \zeta_z = J\left(\frac{\partial x}{\partial \xi}\frac{\partial y}{\partial \eta} - \frac{\partial x}{\partial \eta}\frac{\partial y}{\partial \xi}\right).$$

where

$$\begin{aligned} \xi_x &= \frac{\partial \xi}{\partial x}, \quad \xi_y = \frac{\partial \xi}{\partial y}, \quad \xi_z = \frac{\partial \xi}{\partial z}, \\ \eta_x &= \frac{\partial \eta}{\partial x}, \quad \eta_y = \frac{\partial \eta}{\partial y}, \quad \eta_z = \frac{\partial \eta}{\partial z}, \\ \zeta_x &= \frac{\partial \zeta}{\partial x}, \quad \zeta_y = \frac{\partial \zeta}{\partial y}, \quad \zeta_z = \frac{\partial \zeta}{\partial z} \end{aligned} \tag{3.1.2}$$

The volume of the cell or the Jacobian determinant of the transformation is defined as,

$$J = \frac{\partial (x,y,z)}{\partial (\xi,\eta,\zeta)} = \begin{vmatrix} x_\xi & x_\eta & x_\zeta \\ y_\xi & y_\eta & y_\zeta \\ z_\xi & z_\eta & z_\zeta \end{vmatrix}.$$

Therefore, transformed Navier-Stokes equations in curvilinear form can be written as

$$\frac{\partial \widehat{\boldsymbol{U}}}{\partial t} + \frac{\partial \widehat{\boldsymbol{F}}}{\partial \xi} + \frac{\partial \widehat{\boldsymbol{G}}}{\partial \eta} + \frac{\partial \widehat{\boldsymbol{H}}}{\partial \zeta} = \frac{\partial \widehat{\boldsymbol{F}_v}}{\partial \xi} + \frac{\partial \widehat{\boldsymbol{G}_v}}{\partial \eta} + \frac{\partial \widehat{\boldsymbol{H}_v}}{\partial \zeta} + \boldsymbol{W}, \tag{3.1.3}$$

where

$$\widehat{\boldsymbol{U}} = \frac{1}{J}\boldsymbol{U}$$

$$\widehat{\boldsymbol{F}} = \frac{1}{J}\begin{bmatrix} \rho_s U \\ \rho U u + p\xi_x \\ \rho U v + p\xi_y \\ \rho U w + p\xi_z \\ (E+p)U \\ E_v U \end{bmatrix}, \quad \widehat{\boldsymbol{G}} = \frac{1}{J}\begin{bmatrix} \rho_s V \\ \rho V u + p\eta_x \\ \rho V v + p\eta_y \\ \rho V w + p\eta_z \\ (E+p)V \\ E_v V \end{bmatrix} \quad \widehat{\boldsymbol{H}} = \frac{1}{J}\begin{bmatrix} \rho_s W \\ \rho W u + p\varsigma_x \\ \rho W v + p\varsigma_y \\ \rho W w + p\varsigma_z \\ (E+p)W \\ E_v W \end{bmatrix}.$$

The contra-variant velocities U, V, and W in ξ, η, ζ directions are defined as

$$\begin{aligned} U &= \xi_x u + \xi_y v + \xi_z w, \quad V = \eta_x u + \eta_y v + \eta_z w, \\ W &= \zeta_x u + \zeta_y v + \zeta_z w. \end{aligned} \tag{3.1.4}$$

The viscous fluxes converted from Cartesian form to the curvilinear form in ξ,η, and ζ directions can be expressed as

$$\widehat{\boldsymbol{F}}_v = \frac{1}{J}\begin{bmatrix} \xi_x\psi_x + \xi_y\psi_y + \xi_z\psi_z \\ \xi_x\tau_{xx} + \xi_y\tau_{xy} + \xi_z\tau_{xz} \\ \xi_x\tau_{yx} + \xi_y\tau_{yy} + \xi_z\tau_{yz} \\ \xi_x\tau_{zx} + \xi_y\tau_{zy} + \xi_z\tau_{zz} \\ \xi_x\Theta_x + \xi_y\Theta_y + \xi_x\Theta_z \\ \xi_x\Phi_x + \xi_y\Phi_y + \xi_x\Phi_z \end{bmatrix}, \quad \widehat{\boldsymbol{G}}_v = \frac{1}{J}\begin{bmatrix} \eta_x\psi_x + \eta_y\psi_y + \eta_z\psi_z \\ \eta_x\tau_{xx} + \eta_y\tau_{xy} + \eta_z\tau_{xz} \\ \eta_x\tau_{yx} + \eta_y\tau_{yy} + \eta_z\tau_{yz} \\ \eta_x\tau_{zx} + \eta_y\tau_{zy} + \eta_z\tau_{zz} \\ \eta_x\Theta_x + \eta_y\Theta_y + \eta_x\Theta_z \\ \eta_x\Phi_x + \eta_y\Phi_y + \eta_x\Phi_z \end{bmatrix},$$

$$\widehat{\boldsymbol{H}}_v = \frac{1}{J}\begin{bmatrix} \zeta_x\psi_x + \zeta_y\psi_y + \zeta_z\psi_z \\ \zeta_x\tau_{xx} + \zeta_y\tau_{xy} + \zeta_z\tau_{xz} \\ \zeta_x\tau_{yx} + \zeta_y\tau_{yy} + \zeta_z\tau_{yz} \\ \zeta_x\tau_{zx} + \zeta_y\tau_{zy} + \zeta_z\tau_{zz} \\ \zeta_x\Theta_x + \zeta_y\Theta_y + \zeta_x\Theta_z \\ \zeta_x\Phi_x + \zeta_y\Phi_y + \zeta_x\Phi_z \end{bmatrix}.$$

The inverse of the determinant of the transformation Jacobian is defined as

$$\frac{1}{J} = \frac{\partial x}{\partial \xi}\frac{\partial y}{\partial \eta}\frac{\partial z}{\partial \zeta} + \frac{\partial x}{\partial \eta}\frac{\partial y}{\partial \zeta}\frac{\partial z}{\partial \xi} + \frac{\partial x}{\partial \zeta}\frac{\partial y}{\partial \xi}\frac{\partial z}{\partial \eta} - \frac{\partial x}{\partial \xi}\frac{\partial y}{\partial \zeta}\frac{\partial z}{\partial \eta} - \frac{\partial x}{\partial \eta}\frac{\partial y}{\partial \xi}\frac{\partial z}{\partial \zeta} - \frac{\partial x}{\partial \zeta}\frac{\partial y}{\partial \eta}\frac{\partial z}{\partial \xi}, \tag{3.1.5}$$

3.1.2 Finite Volume Method

The laws of conservation for fluid motion can be expressed mathematically either in differential or integral form. When the integral form is employed, the conservation laws are applied across small volumes that make up the domain of solution and are referred to as the finite volume method. If the case is of only two dimensions, areas are used instead of volumes. Unlike finite difference methods, finite volume schemes are also capable of handling unstructured meshes and provide far greater flexibility and applicability.

To present a clear account of the mathematical process of applying the integral form of the conservation laws across each cell during each time interval, it is necessary to introduce a terminology to identify each component. In a two dimensional problem, a cell within the domain occupies the space between $\left[x_{i+1/2}, x_{i-1/2}\right]$ and $\left[y_{j+1/2}, y_{j-1/2}\right]$, where i, j denote the indices of the cell centre, and $x = x_{i \pm 1/2}$ and $y = y_{i \pm 1/2}$ are referred to as the cell edges (see Figure.3.1).

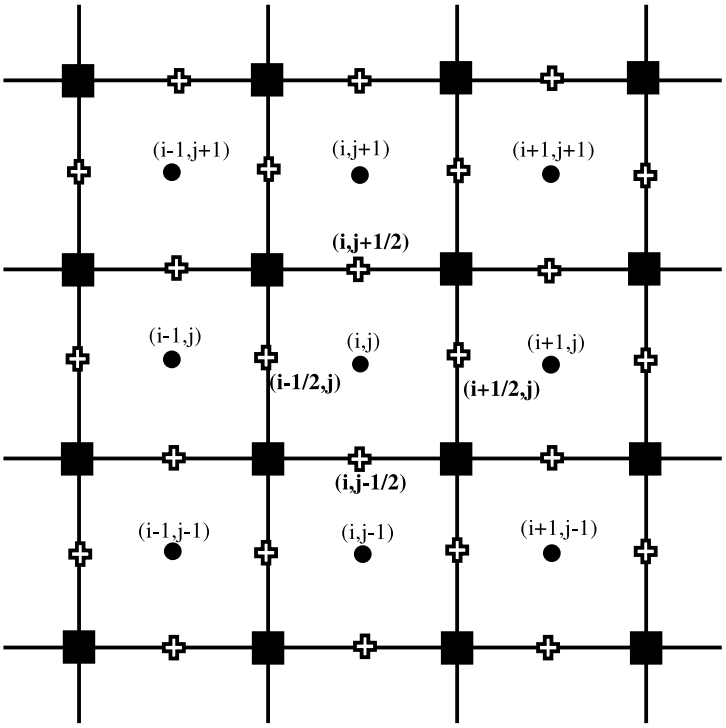

Figure 3.1 — *Notation for control volume discretisation.*

Also, time is divided into time intervals $\left[t^n, t^{n+1}\right]$. To present the expression in a simplified

manner, the integral form in one dimensional form can be expressed as

$$\int_{x_{i-\frac{1}{2}}}^{x_{i+\frac{1}{2}}} \left\{ \boldsymbol{u}\left(x,t^{n+1}\right) - \boldsymbol{u}\left(x,t^{n}\right) \right\} dx = \\ - \int_{t^n}^{t^{n+1}} \left\{ \boldsymbol{f}\left[\boldsymbol{u}\left(x_{i+\frac{1}{2}},t\right)\right] - \boldsymbol{f}\left[\boldsymbol{u}\left(x_{i-\frac{1}{2}},t\right)\right] \right\} dt. \tag{3.1.6}$$

The conservation form of the above equation can be written as

$$\overline{\boldsymbol{u}}_i^{n+1} = \overline{\boldsymbol{u}}_i^{n} - \lambda \left\{ \widehat{\boldsymbol{f}}_{i+\frac{1}{2}}^{n} - \widehat{\boldsymbol{f}}_{i-\frac{1}{2}}^{n} \right\}, \tag{3.1.7}$$

where

$$\lambda = \frac{\Delta t}{\Delta x}, \tag{3.1.8}$$

$$\widehat{\boldsymbol{f}}_{i+\frac{1}{2}}^{n} \approx \frac{1}{\Delta x} \int_{t^n}^{t^{n+1}} \boldsymbol{f}\left\{ \boldsymbol{u}\left(x_{i+\frac{1}{2}},t\right) \right\} dt, \tag{3.1.9}$$

$$\overline{\boldsymbol{u}}_i^{n} \approx \frac{1}{\Delta x} \int_{x_{i-\frac{1}{2}}}^{x_{i+\frac{1}{2}}} \boldsymbol{u}\left(x,t^{n}\right) dx. \tag{3.1.10}$$

The spatial cell integral averages, identified with overbar, are taken across the cell, where $\Delta x = x_{i+1/2} - x_{i-1/2}$, while hat represents the time integral averages taken across $\Delta t = t^{n+1} - t^n$.

3.1.3 Finite Volume Discretisation of Navier-Stokes Equations

The inviscid component of the NS equations can be written in the form demonstrated in Equation 3.1.6 in curvilinear co-ordinate system as follows;

$$\iiint_V \frac{\partial \widehat{\boldsymbol{U}}}{\partial t} dV + \iint_{\partial V} \left(\widehat{\boldsymbol{F}} n_\xi + \widehat{\boldsymbol{G}} n_\eta + \widehat{\boldsymbol{H}} n_\zeta \right) dS = \iiint_V \widehat{\boldsymbol{W}} dV \tag{3.1.11}$$

where the outward normal vector at ∂V in ξ, η and ζ space is $\vec{n} = \left(n_\xi + n_\eta + n_\zeta\right)^T$. The finite volume discretisation for a Cartesian grid in ξ, η, and ζ space with disjunct cells becomes

$$\iiint_{V_{i,j,k}} \frac{\partial \widehat{U}}{\partial t} d\xi d\eta d\zeta + \iint_{S_{i+\frac{1}{2},j,k}} \widehat{F} d\eta d\zeta - \iint_{S_{i-\frac{1}{2},j,k}} \widehat{F} d\eta d\zeta + \iint_{S_{i,j+\frac{1}{2},k}} \widehat{G} d\xi d\zeta - \iint_{S_{i,j-\frac{1}{2},k}} \widehat{G} d\xi d\zeta + \iint_{S_{i,j,k+\frac{1}{2}}} \widehat{H} d\xi d\eta - \iint_{S_{i,j,k-\frac{1}{2}}} \widehat{H} d\xi d\eta = \iiint_{V_{i,j,k}} \widehat{W} d\xi d\eta d\zeta \quad (3.1.12)$$

The cell faces of $V_{i,j,k}$ are $S_{i+\frac{1}{2},j,k} \cdots S_{i,j,k-\frac{1}{2}}$. The averaged values of conserved variable $\widehat{U}$ and source term $\widehat{W}$ are taken at the cell centre and flux vectors $\widehat{F}$, $\widehat{G}$, and $\widehat{H}$ are assumed to be constant along the cell face. Therefore, it is possible to write a system of ordinary differential equations with respect to time:

$$\frac{d\widehat{U}_{i,j,k}}{dt} + \frac{\widehat{F}_{i+\frac{1}{2},j,k} - \widehat{F}_{i-\frac{1}{2},j,k}}{\Delta\xi} + \frac{\widehat{G}_{i,j+\frac{1}{2},k} - \widehat{G}_{i,j-\frac{1}{2},k}}{\Delta\eta} + \frac{\widehat{H}_{i,j,k+\frac{1}{2}} - \widehat{H}_{i,j,k-\frac{1}{2}}}{\Delta\zeta} = \widehat{W}_{i,j,k} \quad (3.1.13)$$

3.2 Compressible Navier-Stokes Solver (CNS3D)

As mentioned previously, the numerical simulations presented in this thesis have been carried out using the Computational Fluid Dynamics code (CNS3D)[40,41,42,43,44,45]. This code is a three-dimensional compressible Navier-Stokes code; furthermore, it incorporates a wide variety of high-resolution and very high-order accurate numerical methods as well as various time integration methods. Over a period of 20 years CNS3D has been under constant development extending its capability; the computational methods and models implemented within the CNS3D code have been highlighted in a number of key publications over the past couple of decades by Drikakis *et al*[33,35,36,37,39,40,41,42,43,44,45,162].

To extend the capability of CNS3D, the present work has undertaken to implement the mathematical models required to describe hypersonic flow phenomena, chemical and thermal non-equilibrium effects as well as surface chemistry and ablation effects. The physical models that have been implemented are presented in Chapter 2. In this Section and the Sections that follow, the numerical aspect of the code essential for the calculations process is presented in detail.

The high-resolution methods used in CNS3D essentially employ some non-linear ”recipe” to regulate oscillations that may be present within the solution[38]. The high-resolution methods tailor the stencil employed for the differencing depending on the local solution where oscillations are kept under control via the use of the non-linearity (linear methods utilise the same differencing stencil everywhere regardless of the local solution). Therefore, high-resolution methods show spacial and temporal dependency as well as a function of the nature of the local solution. Furthermore, the employed non-linear principle must ensure that spurious oscillations are removed, allowing a minimum of second- order accuracy in the smooth regions. Accordingly, high-resolution methods obtain an accurate solution which has some physical meaning by selecting the ”best” technique for approximating the solution given the evidence provided by the local solution[34,38,46].

The high-order methods available in the CNS3D code relate to the spatial accuracy achieved over the area of smooth solution. By extrapolating the variables as linear, quadratic or higher-order functions in a cell, it is possible to achieve various degrees of special accuracy; in the CNS3D code, the high-order special accuracy of reconstruction ranges from second-order to ninth-order.

It should be noted that these high-resolution, high-order numerical methods cannot be found in commercially available software. The computational code has been validated and used for a wide variety of simulations featuring flow physics such as low and high speed flows, shock waves, mixing of fluids, unsteady attached and separated flows, multi-component flows to name but a few. In this thesis, high resolution methods are a key aspect of numerics and the use of these techniques in non-equilibrium hypersonic flows to resolve HB-2 and double-cone flows can be considered an important contribution to hypersonic research.

Calculation Process of CNS3D

- As the first step in the calculation process, it is necessary to define the physical domain of the geometry where flow computations need to take place.
- The established domain is then divided into a number of discrete cells which is referred to as a mesh or grid (see Figure 3.1); the grid generated could either be structured or

unstructured. In this thesis all the calculations have been carried out using structured grids.

- Depending on the flow problem, the conditions at the boundary can be defined prior to running the code within problem file (.prb); the problem file is then read at the beginning of the calculation process by CNS3D code, and allocates the desired boundary conditions. In this thesis, the boundary conditions used have been inflow, outflow, and symmetry; in addition, solid wall with fixed wall temperature and ablation wall with variable wall temperature was also utilised. The ablation wall boundary condition was implemented as part of the work carried out to investigate ablating effects and surface chemistry (further details are available in Chapter 6).

- The initial conditions are specified as an initial guess to start the simulation. The initial conditions used depend mostly on the problem analysed; in CNS3D it is possible to initialise with sophisticated initial conditions which have been developed in the past to trigger specific features such as a turbulent boundary layer or a mixing interface[34].

- Once the CNS3D code initiates the calculations process, the equations (Navier-Stokes or Euler equations) are solved iteratively as a steady state or transient. Once sufficient data have been collected various post-processing tools can be employed to analyse and visualise the results.

To solve the system of numerical equations, inviscid and viscous terms are dealt with separately and then added together to obtain the complete effect of all terms. This is a rather convenient way of handling a complex set of equations. The computational code CNS3D solves the inviscid fluxes of the governing equations in two initial consecutive steps as presented in Figure 3.2;

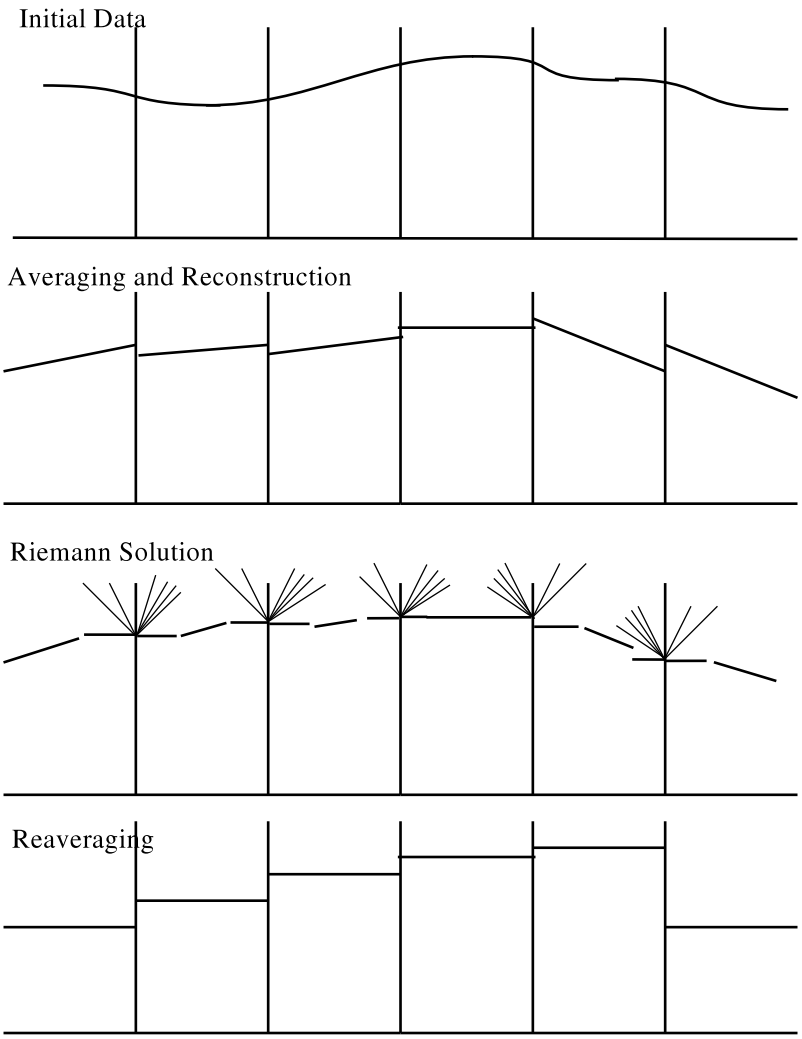

Figure 3.2 — *Calculation procedure observed in high resolution methods*[after 103].

1. **Spatial Reconstruction**: As the initial step, interpolation of "reconstruction" is carried out using a technique such as MUSCL or WENO [†]. In addition, within the first step, solution averaging and solution limiting may occur.

2. **Riemann Solution**: In the next step, the reconstructed values are used in the Riemann solution to generate a physically relevant flux. It allows superior wave capturing and improves the numerical modelling of smooth and non-smooth waves.

The methodical approach, where each step focuses on a specific function, leads to solving the system of equations, and makes the high resolution methods extremely physical and elegant. Also a variety of techniques have been developed to control the capability and accuracy of

[†]these methods will be explained in detail later on in this chapter

TVD methods. The methods and conditions employed for the calculations and subsequently presented here are specifically chosen depending on the existing literature suggesting that the methods may be successfully applied to hypersonic flow analysis. The spatial reconstruction and Riemann solution techniques are discussed further in Sections 3.3 and 3.4 respectively.

3.3 Spatial Reconstruction

Two families of numerical reconstruction have been employed in this study: (i) 2nd- and 5th-order variants of the MUSCL schemes; (ii) 5th- and 9th-order WENO schemes. Reconstruction techniques with accuracy of reconstruction, ranging from second order such as Monotone Upstream-centred Schemes for Conservation Laws (MUSCL) to fifth order such as Essential Non-Oscillatory (ENO) and Weighted Essential Non-Oscillatory (WENO), were used in previous studies[29,107,125]. The second order MUSCL scheme has been formulated to gain optimal accuracy in smooth regions of the flow while being limited in the presence of discontinuities through non-linear limiting functions. There are numerous limiting functions available in literature[6,38,103] and many have been applied to hypersonic flow problems[144]. In this section a fairly detailed account of MUSCL and WENO schemes is presented.

3.3.1 Reconstruction Methods: Conservative, Primitive and Characteristic Form

The reconstruction process can be performed via conservative, primitive or characteristic variables.

Conservative Variable Form

The conservative variable form of the Euler equations can be expressed in vector-matrix form as;

$$\frac{\partial \boldsymbol{U}}{\partial t} + A\frac{\partial \boldsymbol{U}}{\partial x} = 0. \tag{3.3.1}$$

where $\boldsymbol{U}$ and $\boldsymbol{F}$ are defined in Equation 2.2.2 and 2.3.1 respectively. The Jacobian $A=\frac{\partial F}{\partial \boldsymbol{U}}$.

Primitive Variable Form

It is possible to solve the equation using the primitive variable form[23,151]. Mosedale(2009) has demonstrated that by employing primitive variable it is possible to avoid pressure oscillations that may materialise. This is by no means a guaranty to obtain a smooth solution; however, it can be argued that it is a better option that using conserved variables. The primitive variable vector $\boldsymbol{Q}$ is identified as

$$\boldsymbol{Q} = \left[\rho_{N_2}, \rho_{O_2}, \ldots, \rho_{CN}, u, v, P, E_v/\rho \right]^T, \tag{3.3.2}$$

Therefore, Equation 3.3.1 can be expressed in primitive variable vector-matrix form as

$$\frac{\partial \boldsymbol{Q}}{\partial t} + C\frac{\partial \boldsymbol{Q}}{\partial x} = 0. \tag{3.3.3}$$

Here the Jacobian $C = \dfrac{\partial \boldsymbol{F}}{\partial \boldsymbol{Q}}$. The reconstruction stage in CNS3D is in fact carried out using primitive variables.

Characteristic Variable Form

The work carried out by researchers such as Qiu and Shu(2002)[135], and Titarev and Toro(2004)[150] concludes that, when the presence of complex and strong shocks are present it is necessary to perform the reconstruction via the characteristic form. In block structured version of CNS3D, reconstruction using characteristic form is not yet available and was not tackled during the course of this project. However, development and implementation of characteristic variable form in CNS3D is under way. Prior to carrying out the process of spatial reconstruction, the conserved variables need to be transformed into characteristic variables. Once the reconstruction is complete, the variables are transformed back into conserved variables.

To obtain the characteristic form, the vector of conserved variables must be multiplied by L as;

$$\widetilde{\boldsymbol{U}} = L\boldsymbol{U} \tag{3.3.4}$$

where L is the matrix whose rows are left characteristic vectors or left eigenvector of A.

$$L = \{l_{1,1}, l_{2,1}, l_{3,1}, \cdots, l_{n,1}\}^T \tag{3.3.5}$$

By multiplying both sides of the equation by L

$$L\frac{\partial \boldsymbol{U}}{\partial t} + LA\frac{\partial \boldsymbol{U}}{\partial x} = 0, \tag{3.3.6}$$

and combining Equation 3.3.6 and Equation 3.3.4, the characteristic form can be written:

$$\frac{\partial \widetilde{\boldsymbol{U}}}{\partial t} + LAR\frac{\partial \boldsymbol{U}}{\partial x} = 0. \tag{3.3.7}$$

The spatial reconstruction step described earlier inherited with in Godonov scheme can be carried out using the characteristic variables devised in Equation 3.3.7. Once the spacial reconstruction is complete, as the final step, R matrix whose rows are the right characteristic vectors or right eigenvector of A must be multiplied by $\widetilde{\boldsymbol{U}}$, hence

$$\boldsymbol{U} = \widetilde{\boldsymbol{U}}R. \tag{3.3.8}$$

where

$$\frac{\partial \boldsymbol{U}}{\partial t} + \Lambda\frac{\partial \boldsymbol{U}}{\partial x} = 0, \tag{3.3.9}$$

as

$$LAR = \Lambda \tag{3.3.10}$$

3.3.2 MUSCL Type Schemes and Limiting Functions

The MUSCL (Monotone Upwind-centered Scheme for Conservation Laws) scheme of van Leer uses piecewise linear spatial reconstruction, which is second-order accurate in smooth regions of the flow away from extrema[95,152,162]. To control oscillations, slope limiters are used to keep the interpolation within an acceptable range, thereby ensuring a total variation diminishing (TVD) condition.

If $\Delta \boldsymbol{U}_{i-\frac{1}{2}} = \boldsymbol{U}_i - \boldsymbol{U}_{i-1}$, $\Delta \boldsymbol{U}_{i+\frac{1}{2}} = \boldsymbol{U}_i - \boldsymbol{U}_{i+1}$ and $\Delta \boldsymbol{U}_{i+\frac{3}{2}} = \boldsymbol{U}_{i+2} - \boldsymbol{U}_{i+1}$, then [146]

$$\boldsymbol{U}^L_{i+\frac{1}{2}} = \boldsymbol{U}_i + \frac{1}{4}\left[(1-c)\phi^{lim}\left(r_i^{lim,L}\right)\Delta \boldsymbol{U}_{i-\frac{1}{2}} + (1+c)\phi^{lim}\left(\frac{1}{r_i^{lim,L}}\right)\Delta \boldsymbol{U}_{i+\frac{1}{2}}\right], \tag{3.3.11}$$

$$\boldsymbol{U}^R_{i+\frac{1}{2}} = \boldsymbol{U}_{i+1} - \frac{1}{4}\left[(1-c)\phi^{lim}\left(r_i^{lim,R}\right)\Delta \boldsymbol{U}_{i+\frac{3}{2}} + (1+c)\phi^{lim}\left(\frac{1}{r_i^{lim,R}}\right)\Delta \boldsymbol{U}_{i+\frac{1}{2}}\right]. \tag{3.3.12}$$

The limiting function is identified above as $\phi(r)$, and c is a free parameter. The vector of cell average variable presented in conservative or primitive form is denoted by $\boldsymbol{U}$, where integer i represents the cell centre.

If $r_i^{lim,L} = \dfrac{\Delta \boldsymbol{U}_{i+\frac{1}{2}}}{\Delta \boldsymbol{U}_{i-\frac{1}{2}}}$, $\quad r_i^{lim,R} = \dfrac{\Delta \boldsymbol{U}_{i+\frac{1}{2}}}{\Delta \boldsymbol{U}_{i+\frac{3}{2}}}$, then the limiting functions subjected to order of reconstruction accuracy can be defined as follows.

Fifth-order: MUSCL 5^{th} Order: (M5)

The fifth-order MUSCL scheme is defined as

$$\phi*^{lim}_{M5,L} = \frac{-2/r_{i-1}^{lim,L} + 11 + 24 r_i^{lim,L} - 3 r_i^{lim,L} r_{i+1}^{lim,L}}{30} \tag{3.3.13}$$

$$\phi*^{lim}_{M5,R} = \frac{-2/r_{i+2}^{lim,R} + 11 + 24 r_{i+1}^{lim,R} - 3 r_{i+1}^{lim,R} r_i^{lim,R}}{30} \tag{3.3.14}$$

where

$$r_i^{lim,L} = \frac{\Delta U_{i+\frac{1}{2}}}{\Delta U_{i-\frac{1}{2}}}, \quad r_i^{lim,R} = \frac{\Delta U_{i-\frac{1}{2}}}{\Delta U_{i+\frac{1}{2}}}. \tag{3.3.15}$$

To satisfy monotonicity, limiting conditions are enforced on the above extrapolations as follows:

$$\phi_{M5,L}^{lim} = max\left(0, min\left(2, 2r_i^{lim,L}, \phi*_{M5,L}^{lim}\right)\right) \tag{3.3.16}$$

$$\phi_{M5,R}^{lim} = max\left(0, min\left(2, 2r_i^{lim,R}, \phi*_{M5,R}^{lim}\right)\right) \tag{3.3.17}$$

Second-order: van Albada : (VA)

$$\phi_{VA}^{lim} = \frac{r_i^{lim}\left(1 + r_i^{lim}\right)}{1 + \left(r_i^{lim}\right)^2}, \tag{3.3.18}$$

Second-order: van Leer: (VL)

$$\phi_{VL}^{lim} = \frac{2r_i^{lim}}{1 + r_i^{lim}}, \tag{3.3.19}$$

Second-order: Minmod: (MM)

$$\phi_{MM}^{lim} = min\left(1, r_i^{lim}\right), \tag{3.3.20}$$

The free parameter c in Equations 3.3.11 and 3.3.12 is set to 1/3 for third-order limiter. However, it does not affect the accuracy of the second order limiter due to their symmetric status.

3.3.3 Weighted Essentially Non-Oscillatory (WENO) Schemes

The basic principle of a WENO interpolation in finite volume form is to interpolate an interface value for each variable from all available stencils, and to average them with appropriate weighting to achieve the final result which is then entered into the calculation of the flux. Through this approach, a range of three-cell stencils can theoretically produce a 5^{th}-order accurate reconstruction. Non-linearity is introduced through the weights, which are made dependent on

the 'smoothness' of each candidate stencil - those stencils adjudged to contain a discontinuity are given an effective zero weighting. This can be expressed mathematically as

$$U_{j+\frac{1}{2}} = \sum_{m=0}^{2} \omega_m \hat{U}^m_{j+\frac{1}{2}}, \tag{3.3.21}$$

where $\hat{U}^m_{j+\frac{1}{2}}$ is the interpolated value for each stencil, and ω_m is the weight corresponding to stencil m. In the work of Shu, these weights were originally formulated as

$$\omega_m = \frac{\alpha_m}{\sum_{l=0}^{2} \alpha_l}, \text{where} \quad \alpha_m = \frac{\bar{\omega}_m}{(\varepsilon + \beta_m)^p}. \tag{3.3.22}$$

ε is a small parameter to keep α bounded, β_m are the 'smoothness indicators' as laid out in literature[7,107,114]; p is a free parameter, and $\bar{\omega}_m$ are the ideal weights required to reduce to a fifth-order central difference scheme in smooth flow. The value of ε used in this study is 10^{-36}.

More recent work has revealed that the above formulation is not sufficient to maintain the maximum possible accuracy around critical points[74]. They suggest that a simple mapping of the weights calculated as before to bring them closer to the ideal weights, whilst retaining the required behaviour away from these regions, resolves this issue. The modified weights are calculated as

$$\omega_m^{(M)} = \frac{\alpha_m^*}{\sum_{i=0}^{2} \alpha_m^*}, \tag{3.3.23}$$

$$\alpha_m^* = g_m(\omega_m), \tag{3.3.24}$$

$$g_m(\omega_m) = \frac{\omega_m(\bar{\omega}_m + \bar{\omega}_m^2 - 3\bar{\omega}_m\omega_m + \omega_m^2)}{\bar{\omega}_m^2 + \omega_m(1 - 2\bar{\omega}_m)}, \tag{3.3.25}$$

thus, the mapping is relatively cheap. Following the implementation, it was observed that the results obtained are improved gaining greater convergence for a coarse grid. The extension to 9^{th} order follows simply, being built upon a convex combination of 5-cell stencils.

Local Order Reduction

As mentioned earlier, WENO scheme assigns nearly zero weights to a stencil which cross a discontinuity and thereby, avoid generating large oscillations. If the solution contains two discontinuities which are too close to each other, the spurious oscillations would be unavoidable as the reconstruction procedure will not be able to find a smooth stencil. To avert this problem, Titarev *et al*, suggested employing a local domain reduction technique[71,150]; this method is employed in CNS3D computational code.

Consider computation of the left boundary extrapolated values for the cell I_{ijk} used in the evaluation of the numerical flux $F_{i+1/2,j,k}$. For each Gaussian integration point $\left(x_{i+1/2,j,k}-0, y_\alpha, z_\beta\right)$ it is essential to satisfy the following condition:

$$|\rho\left(x_{i+1/2,j,k}-0, y_\alpha, z_\beta\right)-\rho_{ijk}| \leq 0.9\rho_{ijk}, |p\left(x_{i+1/2,j,k}-0, y_\alpha, z_\beta\right)- p_{ijk}| \leq 0.9\rho_{ijk} \quad (3.3.26)$$

If the Equation 3.3.26 is not satisfied the order of reconstruction is decreased in each of the one-dimensional WENO sweeps and the reconstruction step, for the left boundary extrapolated values, is repeated. If the condition is still not satisfied, the order of reconstruction is further reduced, to second or even first order. The left boundary extrapolated values are treated in an entirely similar manner. It must be noted that, by utilising the above procedure does not in anyway degrade the high order of accuracy of the schemes for smooth solutions[71,150].

3.4 Riemann Solver

Most modern numerical methods rely on Riemann solvers to generally improve the modelling of smooth waves as well as non-smooth shocks and contact waves[103]. The exact solution of a Riemann problem incorporated into numerical modelling cannot be considered effective; reason being, the numerical approximations based on Riemann problem may need to solve the Riemann problem thousands of times to arrive at a single solution[84]. Therefore, in modern numerical methods the solution to approximate Riemann problem is widely used, which is in

many ways better than the solution to the true Riemann problem, and could obtain the solution at a fraction of the cost[84,103].

The HLLC, and ROE are two of the most well known approximate Riemann solvers that has been used in previous studies in compressible flows[56,132,133,139]. Even though it is not generally used in recent times, Characteristic Bases Scheme (CBS) scheme has also been employed by research in the past to tackle hypersonic flow problems[49]. In this thesis, Riemann solver HLLC has been used for the purposes of validation.

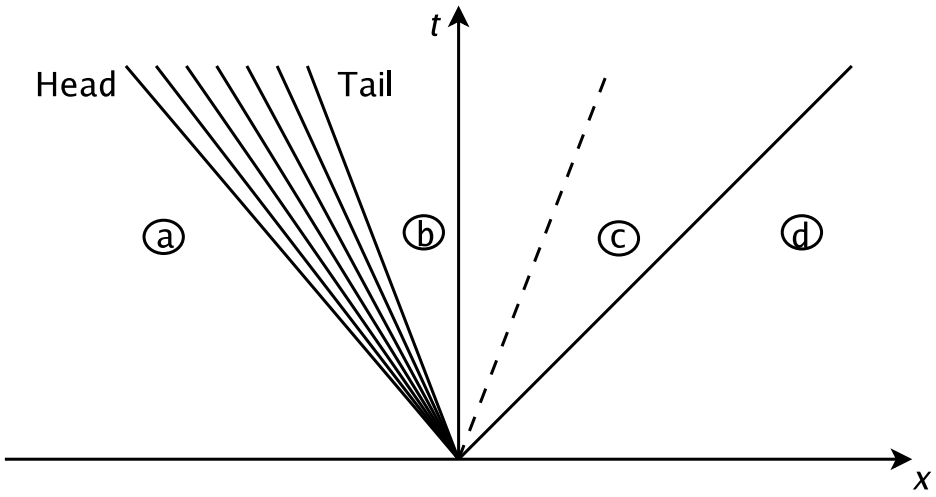

(a)

Figure 3.3 — The typical wave structure of the Riemann problem.

3.4.1 The HLLC Riemann Solver

The inter-cell flux used in the calculations is based on the HLLC approximate Riemann solver devised by Toro *et al*[151]. HLLC is a Godunov-type method that assumes a fixed wave configuration for the solution to the Riemann problem.

The typical wave structure of the Riemann problem is presented in Figure 3.3 and the regions are identified in the following way; between regions a and b -a left-running shock/rarefaction, between regions b and c -a contact/shear wave, and between regions c and d -a right-running shock/rarefaction wave. Each region is in a separate constant state: the left state (region a), the left star state (region b), the right star state (region c), and the right state (region d), and are used to calculate the HLLC flux. The HLLC scheme for the conventional compressible Euler

equations is presented below. The additional equations associated with the chemical reactions are discretised in a similar fashion.

It is necessary to estimate the wave speeds for all three waves. This can be done either by direct estimation using eigenvalues or by means of calculating changes in pressure and velocity with an iterative process. By applying the Rankine-Hugoniot conditions across each of the waves, the fluxes are determined. The HLLC approximate Riemann solver is quite convenient to use and easy to handle[84,151]. The two averaged intermediate states, $\boldsymbol{U}_{*L}$ and $\boldsymbol{U}_{*R}$, are separated by the contact wave of speed S_M [103]. The extension to real gas for HLLC solver is very much similar to the ideal gas version; the density of the additional species and vibrational energy terms are included in order to calculate the flux. The approximate solution to the Riemann problem is outlined below.

As the first step pressure in the star region is estimated as

$$p_* = \frac{1}{2}(p_L + p_R) - \frac{1}{2}(u_R - u_L)(\bar{\rho}\bar{a}) \, . \tag{3.4.1}$$

As the next step, the left and right wave speeds S_L and S_R respectively are calculated as follows

$$S_L = u_L - a_L q_L \, , \quad S_R = u_R - a_R q_R \, ,$$

with

$$q_K = \begin{cases} 1 & \text{if} \quad p_* \leq p_K \\ [1 + \frac{\gamma+1}{2\gamma}(p_*/p_K - 1)]^{\frac{1}{2}} & \text{if} \quad p_* > p_K \end{cases} .$$

The star wave speed is given by

$$S_M = \frac{p_R - p_L + \rho_L u_L(S_L - u_L) - \rho_R u_R(S_R - u_R)}{\rho_L(S_L - u_L) - \rho_R(S_R - u_R)} \, .$$

The left and right star states can be expressed as

$$\mathbf{U}_{*K} = \rho_K \left(\frac{S_K - u_K}{S_K - S_*} \right) \begin{pmatrix} \frac{\rho_{(s)K}}{\rho_K} \\ S_* \\ v_K \\ w_K \\ \frac{E_K}{\rho_K} + (S_* - u_K) \left[S_* + \frac{p_K}{\rho_K (S_K - u_K)} \right] \\ (E_v)_K \end{pmatrix} . \tag{3.4.2}$$

and apply the Rankine-Hugoniot conditions to determine the flux

$$\mathbf{F}_{i+1/2}^{HLLC} = \begin{cases} \mathbf{F}_L, & 0 \leq S_L \\ \mathbf{F}_L + S_L(\mathbf{U}_{*L} - \mathbf{U}_L), & S_L \leq 0 \leq S_* \\ \mathbf{F}_R + S_R(\mathbf{U}_{*R} - \mathbf{U}_R), & S_* \leq 0 \leq S_R \\ \mathbf{F}_R, & 0 \geq S_R \end{cases} . \tag{3.4.3}$$

An additional solver, HLL has also been implemented in the CNS3D code, yet were not employed for the validation effort presented in the following chapters. Details of this solver are presented in Appendix B.

3.5 Time Integration Schemes

The time integration technique and related parameters utilised for a simulation will depend mostly on problem characteristics; more specifically, on the resolution of the grid. A variety of different schemes, which could be classed under explicit[88,158], semi explicit-implicit[91], and fully implicit time integration[23,43,119] methods, have been used to investigate hypersonic problems in the past.

After the calculation of the viscous fluxes, the solution is advanced in time until convergence

is achieved. To capture finer details, it is necessary to employ grids with increasingly finer gird resolutions. In fact, it has been suggested by Druguet *et al.*[48] that to simulate flows similar to double-cone, it is imperative that either fully implicit scheme or any explicit scheme coupled with an acceleration technique are used; it would be impractical to use simple explicit schemes for larger grids and retain any hope for achieving convergence.

As the grid resolution is increased, a significant increase in computational resources and costs become unavoidable. To manage this problem, the simulations are carried out using a method known as domain decomposition. The primary grid is decomposed into multiple sub-grids and the load from each grid is handled by a dedicated processor. The solution generated is communicated between each processor, thereby channelling the information throughout the domain. Therefore, it is possible to accelerate the convergence and reduce the solution time. The formulation relevant for the explicit and implicit time integration methods is presented below.

3.5.1 Explicit Time Integration Scheme

In this thesis, the explicit time marching method, Rung-Kutta (**RK**) time stepping, has been employed for time integration[38]. The second order (**RK**) version method can be defined as:

$$\boldsymbol{U}_j^1 = \boldsymbol{U}_j^n + \frac{1}{2}\frac{\triangle t}{\triangle x}\boldsymbol{F}\left(\boldsymbol{U}_j^n\right), \tag{3.5.1}$$

$$\boldsymbol{U}_j^{n+1} = \boldsymbol{U}_j^n + \frac{\triangle t}{\triangle x}\boldsymbol{F}\left(\boldsymbol{U}_j^1\right). \tag{3.5.2}$$

The second order (**RK**) version with the inclusion of Total Variation Diminishing (TVD) is:

$$\boldsymbol{U}_j^1 = \boldsymbol{U}_j^n + \frac{1}{2}\frac{\triangle t}{\triangle x}\boldsymbol{F}\left(\boldsymbol{U}_j^n\right), \tag{3.5.3}$$

$$\boldsymbol{U}_j^{n+1} = \boldsymbol{U}_j^n + \frac{1}{2}\frac{\triangle t}{\triangle x}\left[\boldsymbol{F}\left(\boldsymbol{U}_j^n\right) + \boldsymbol{F}\left(\boldsymbol{U}_j^1\right)\right]. \tag{3.5.4}$$

The third order (**RK**) version is also presented:

$$\boldsymbol{U}_j^1 = \boldsymbol{U}_j^n + \frac{1}{2}\frac{\triangle t}{\triangle x}\boldsymbol{F}\left(\boldsymbol{U}_j^n\right), \tag{3.5.5}$$

$$\boldsymbol{U}_j^2 = \boldsymbol{U}_j^n + \frac{1}{4}\frac{\triangle t}{\triangle x}\left[\boldsymbol{F}\left(\boldsymbol{U}_j^n\right) + \boldsymbol{F}\left(\boldsymbol{U}_j^1\right)\right], \tag{3.5.6}$$

$$\boldsymbol{U}_j^{n+1} = \boldsymbol{U}_j^n + \frac{1}{6}\frac{\triangle t}{\triangle x}\left[\boldsymbol{F}\left(\boldsymbol{U}_j^n\right) + \boldsymbol{F}\left(\boldsymbol{U}_j^1\right) + 4\boldsymbol{F}\left(\boldsymbol{U}_j^2\right)\right]. \tag{3.5.7}$$

Finally, the third order (**RK**) version with extended stability is defined as

$$\boldsymbol{U}_j^1 = \boldsymbol{U}_j^n + \frac{1}{2}\frac{\triangle t}{\triangle x}\boldsymbol{F}\left(\boldsymbol{U}_j^n\right), \tag{3.5.8}$$

$$\boldsymbol{U}_j^2 = \boldsymbol{U}_j^n + \frac{1}{2}\frac{\triangle t}{\triangle x}\left[\boldsymbol{F}\left(\boldsymbol{U}_j^1\right)\right], \tag{3.5.9}$$

$$\boldsymbol{U}_j^{n+1} = \frac{1}{3}\left(2\boldsymbol{U}_j^2 + \boldsymbol{U}_j^n + \frac{\triangle t}{\triangle x}\left[F\left(\boldsymbol{U}_j^2\right) + \boldsymbol{F}\left(\boldsymbol{U}_j^1\right)\right]\right). \tag{3.5.10}$$

In this approach the upper limit of CFL (Courant-Friedrichs Lewyor) is increased to 2.

3.5.2 Implicit Time Integration

There are many types of implicit time integration schemes employed in the literature. Among these methods, the implicit un-factored method has also been used to obtain results presented in this work. The implicit unfactored time marching scheme available in CNS3D has been developed by Drikakis *et al*[39,41,43]. A detailed description of the implicit unfactored time marching scheme available in CNS3D is presented in Bagabir and Drikakis (2004)[6]; here, perfect gas (non-chemical reacting), two dimensional, inviscid version of the scheme has been presented.

To initiate the implicit discretisation solution at time level $n+1$, corresponding to $(t+\delta T)$, the

equation is written

$$J\frac{\alpha_{n+1}\boldsymbol{U}_{i,k}^{n+1}-\alpha_n\boldsymbol{U}_{i,k}^{n}+\alpha_{n-1}\boldsymbol{U}_{i,k}^{n-1}}{\Delta t}+\boldsymbol{E}_{\xi}^{n+1}+\boldsymbol{G}_{\zeta}^{n+1}=0, \tag{3.5.11}$$

where $\alpha_{n+1}=1.+\frac{1}{2}\theta, \alpha_n=1+\theta$, and $\alpha_{n-1}=\frac{1}{2}\theta$. The order of time discretisation is defined by the parameter θ, which holds the values 0 and 1 for the first and second order respectively. As the values of the variables at time level $n+1$ are unknown, the fluxes $\boldsymbol{E}$ and $\boldsymbol{G}$ are linearised for time level n

$$\boldsymbol{F}^{n+1}=\boldsymbol{F}^{n}+A^{n}\Delta\boldsymbol{U}, \quad \boldsymbol{G}^{n+1}=\boldsymbol{G}^{n}+C^{n}\Delta\boldsymbol{U}. \tag{3.5.12}$$

Here, $A=\dfrac{\partial\boldsymbol{F}}{\partial\boldsymbol{U}}$ and $C=\dfrac{\partial\boldsymbol{G}}{\partial\boldsymbol{U}}$ are the Jacobian matrices of the inviscid fluxes $\boldsymbol{F}$ and $\boldsymbol{G}$. Using this, Equation 3.5.11 is written as,

$$J\frac{\alpha_{n+1}\boldsymbol{U}_{i,k}^{n+1}-\alpha_n\boldsymbol{U}_{i,k}^{n}+\alpha_{n-1}\boldsymbol{U}_{i,k}^{n-1}}{\Delta t}+(A^{n}\Delta\boldsymbol{U})_{\xi}+(C^{n}\Delta\boldsymbol{U})_{\zeta}=-\left(\boldsymbol{F}_{\xi}^{n}+\boldsymbol{G}_{\zeta}^{n}\right) \tag{3.5.13}$$

By using a sequence of approximations, q, between time steps n and $n+1$, an un-factored Newton-type method can be constructed, such that

$$\lim_{v>1} q^{v}\rightarrow\boldsymbol{U}^{n+1}, \tag{3.5.14}$$

where v stands for the Newton-type sub-iterations. Therefore,

$$\begin{aligned} &J\frac{\alpha_{n+1}\boldsymbol{q}_{i,k}^{v+1}}{\Delta t}+\left(A^{v}\Delta q^{v+1}\right)_{\xi}+\left(C^{v}\Delta q^{v+1}\right)_{\zeta}= \\ &-J\frac{\alpha_{n+1}\boldsymbol{q}_{i,k}^{v}-\alpha_n\boldsymbol{U}_{i,k}^{n}-\alpha_{n-1}\boldsymbol{U}_{i,k}^{n-1}}{\Delta t}-\left(\boldsymbol{F}_{\xi}^{n}+\boldsymbol{G}_{\zeta}^{n}\right) \end{aligned} \tag{3.5.15}$$

$$q^{v+1} = q^v + \Delta q^{v+1} \tag{3.5.16}$$

The terms $\left(A^v \Delta q^{v+1}\right)_\xi$ and $\left(C^v \Delta q^{v+1}\right)_\xi$ are discretised on the cell centres;

$$\left(A^v \Delta q^{v+1}\right)_\xi = \left(A^v \Delta q^{v+1}\right)_{i+\frac{1}{2},k} - \left(A^v \Delta q^{v+1}\right)_{i-\frac{1}{2},k}, \tag{3.5.17}$$

$$\left(C^v \Delta q^{v+1}\right)_\xi = \left(C^v \Delta q^{v+1}\right)_{i,k+\frac{1}{2}} - \left(C^v \Delta q^{v+1}\right)_{i,k-\frac{1}{2}}. \tag{3.5.18}$$

The terms $\left(A^v \Delta q^{v+1}\right)_{i\pm\frac{1}{2},k}$ and $\left(C^v \Delta q^{v+1}\right)_{i\pm\frac{1}{2},k}$ are defined by splitting the Jacobian A,

$$\left(A^v \Delta q^{v+1}\right)_{i\pm\frac{1}{2},k} = \left(T\Lambda^+ T^{-1}\right)_{i\pm\frac{1}{2},k} \Delta q^+_{i\pm\frac{1}{2},k} + \left(T\Lambda^- T^{-1}\right)_{i\pm\frac{1}{2},k} \Delta q^-_{i\pm\frac{1}{2},k}, \tag{3.5.19}$$

$$\left(C^v \Delta q^{v+1}\right)_{i\pm\frac{1}{2},k} = \left(N\Lambda^+ N^{-1}\right)_{i\pm\frac{1}{2},k} \Delta q^+_{i\pm\frac{1}{2},k} + \left(N\Lambda^- N^{-1}\right)_{i\pm\frac{1}{2},k} \Delta q^-_{i\pm\frac{1}{2},k}, \tag{3.5.20}$$

The matrices T and N represent the left eigenvectors matrices of the Jacobian matrix A and C respectively. The right eigenvector matrices are obtained by taking the inverse of the left eigenvector matrix. The positive and negative eigenvalues are denoted by Λ^+ and Λ^- respectively.

$$\Lambda^+ = \begin{bmatrix} \max(0,\lambda_0) & 0 & 0 & 0 \\ 0 & \max(0,\lambda_0) & 0 & 0 \\ 0 & 0 & \max(0,\lambda_1) & 0 \\ 0 & 0 & 0 & \max(0,\lambda_2) \end{bmatrix}, \tag{3.5.21}$$

$$\Lambda^{-} = \begin{bmatrix} \min(0,\lambda_0) & 0 & 0 & 0 \\ 0 & \min(0,\lambda_0) & 0 & 0 \\ 0 & 0 & \min(0,\lambda_1) & 0 \\ 0 & 0 & 0 & \min(0,\lambda_2) \end{bmatrix}, \tag{3.5.22}$$

The term $\Delta q^{\pm}_{i+\frac{1}{2}}$ is calculated at the cell faces using the equation below:

$$\Delta q^{\pm}_{i+\frac{1}{2}} = b\Delta q_i + \frac{1}{2}(1-b)(3\Delta q_i - \Delta q_{i-1}) \tag{3.5.23}$$

3.5.3 Stiffness Problem

Unlike inviscid or viscous fluxes, the chemical source term W is likely to have components and its Jacobian greater than unity; the reason is that their magnitudes are determined by the rate coefficient rather than flow related variables. By using the dimensionless quantity known as Damköhler number D_a, which is defined as

$$D_a = \frac{\text{Available flow residence time}}{\text{Time required for equilibrium}} = \frac{\tau_f}{\tau_r}, \tag{3.5.24}$$

it is possible to assess the speed of the chemical reaction. In effect, the Damköhler number represents the relative magnitude of the components in the source term to those of the convective terms. Therefore, according to Equation 3.5.24, a large Damköhler number represents a fast chemical reaction (fast approaching equilibrium). The eigenvalues λ of source Jacobian can be used to estimate the size of the time step Δt. For an explicit scheme the condition

$$(\lambda\Delta t)^2 \ll \Delta t \tag{3.5.25}$$

must be satisfied. Therefore, the value of Δt is inversely proportional to λ^2.

If the flow is nearing equilibrium, the value of λ is usually real and negative. In an explicit time marching scheme, to satisfy the Equation 3.5.25, the integrating time step or the value of Courant number (`CFL`) must be kept relatively small. The eigenvalue that causes this problem is known as the parasitic eigenvalue, and the problem is referred to as the *stiffness* problem.

3.6 Axisymmetric Treatment

Both test cases considered in this thesis are axisymmetric. There are several ways to exploit this property of the flow. The first is to use so-called axisymmetric formulation in which the equations are solved on a 2D grid. This leads to a reduction of the computational cost as compared to the full 3D calculation. The axisymmetric effects are accounted for by the additional terms which are inversely proportional to the radial coordinate (further details of this method can be found in Section B.1).

The simulations in this thesis were carried using the second approach, which consists of essentially two steps. Firstly, a two-dimensional structured mesh around the 2D geometry is created in mesh generation software. Secondly, this 2D grid is rotated around the symmetry axis (around x-direction) resulting in a sector of the full 3D domain. Finally, the three-dimensional calculation is performed on this domain and mesh with periodic boundary conditions in the azimuthal (angular) direction. No changes to the governing equation is then required. The computational cost of this method is fairly similar to solving the 2D equations with the axisymmetric source term because the 3D solution is computed for only 3-4 cells in the angular direction, which is roughly equivalent in the computational cost to 3-4 two-dimensional updates.

3.7 Summary

In this chapter the numerical techniques, which have been used to investigate hypersonic flow problems, are presented. The high resolution methods introduced are robust and easy to use; the application of very high-order methods in high Mach number flow problems is considered state of the art.

The computational code CNS3D, which houses the aforementioned numerical models, has been validated using many computational studies under perfect gas conditions. However, up to date, the numerical techniques available in the CNS3D code have not been validated against hypersonic chemically reacting non-equilibrium flows.

The implementation of physical and numerical models to accommodate complex flow mechanisms at hypersonic speeds has to be followed up by the process of verification and validation. In the next three chapters, the HB-2 flare and the double-cone have been simulated under perfect and real gas conditions with non-slip and ablating wall conditions.

CHAPTER 4

Assessment of CFD Method in Hypersonic Flows-I: HB2 Flare Configuration

When you have eliminated the impossible,
whatever remains, however improbable,
must be the truth.

Sir Arthur Ignatius Conan Doyle
(Sherlock Holmes, The Sign of the Four (1890))

4.1 Introduction

To enable the CNS3D code to be used to investigate hypersonic flow, additional equations and physical models have been included, as described in Chapter 2. The CNS3D code developed by Drikakis *et at*[6,38] is designed to handle turbulence in a compressible field; nevertheless, it has not previously been tested on such high-speed problems. Yet, each model has limitations of its application. This is also true for numerical schemes that are available within the code. Therefore, it is imperative to *verify* that all the partial differential equations and other models that describe physical processes are solved correctly, and yield consistent solutions with the increment of grid resolution. Experimental data available in the literature can be used to determine the accuracy of the results in relation to the actual physical solution. This process is known as *validation*[25].

In this chapter, the test case blunted-cone-cylinder-flare designated HB-2 (see Figure 4.1) has been utilised for the purposes of validation. Experiments were conducted in various test facilities such as the von Karman Gas Dynamics Facility (VKF) and the Arnold Engineering Development Centre (AEDC); pressure, heat transfer, and other quantities, were measured and tabulated, under varying Mach numbers and angles of attack. More recently, the Japanese Aerospace Exploration Agency (JAXA) employed HB-2 flare in a series of experiments, which measured force and heat-transfer under varying free stream conditions. The results obtained are available in the literature[54,63,87,101]. The tabulated values of heat flux as well as pressure are invaluable within the context of validation. Even though a limited number of computational studies performed using HB-2 are available in literature[14,82], an assessment of different high-order methods versus second-order of accuracy has not yet been fully explored [§].

The purpose of this chapter is to present the computed results utilising 5^{th}- and 9^{th}-order WENO-M schemes as well as the 2^{nd}- and 5^{th}-order MUSCL schemes, under ideal and chemically reacting gas assumption. These methods provide high accuracy in transitional and turbulent flows, real gas effects, and associated instabilities. Comparisons are performed against experimental data for the wall pressure and heat transfer distributions. All investigations are carried out under the assumption of *steady laminar flow*. The ideal gas results are presented in section 4.2; cases designated 001, 002, 003, and 004 have been simulated under varying free stream conditions. Unfortunately, it was not possible to produce both heat and pressure

[§]The work presented in this chapter has resulted in a journal publication by Tissera *et al*[147].

results for all cases due to the unavailability of experimental data. The cases 003 and 004, have also been computed using the commercial software FLUENT and compared with CNS3D. Finally, the case 005 computed under high enthalpy chemically reacting conditions is presented in section 4.3.

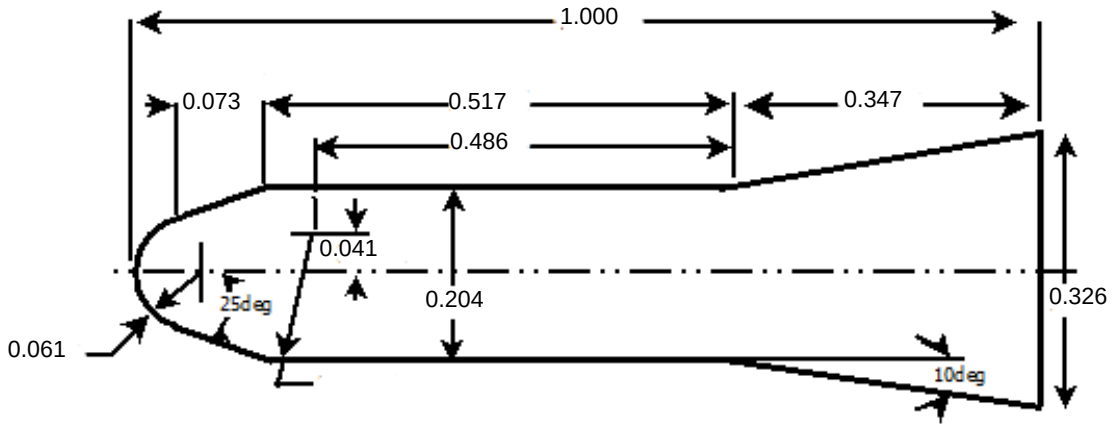

Figure 4.1 — *Schematic of the HB-2 geometry.*

Grid Requirements

Even though the HB-2 configuration does not give rise to overly complicated flow features, to accurately capture the heat transfer and pressure over the surface, it is important to use a sufficiently refined computational mesh. In the present work, several levels of grid refinement have been adopted to assess the improvements made to the numerical accuracy with the increment in grid resolution and order of reconstruction; the total number of grid points within the grid refinement levels ranged from 4704 (98×48) cells to 32768 (256×128) cells, respectively. The grid generated is clustered near the wall. For all grid resolutions, the size of the first grid cell is kept at approximately 10^{-5} (*non-dimensional units*). The accuracy of the heat transfer predicted near the wall is very much dependent on the quality of the grid and the clustering near the wall.

The free stream boundary conditions used for this testcase are supersonic inflow and outflow. At the wall, no-slip isothermal surface is specified. As a result, the normal and transversal

velocity components at the wall are zero. Finally, symmetry condition is employed along the cone axis. The free stream conditions for the cases computed are presented in Table 4.1. The availability of experimental data for the wall pressure and heat flux is shown in Table 4.2. The initial conditions for these cases originate from the experimental data obtained from the VKF and JAXA test facilities. All cases are simulated at zero angle of attack. A typical grid clustered near the wall is shown in Figure 4.2.

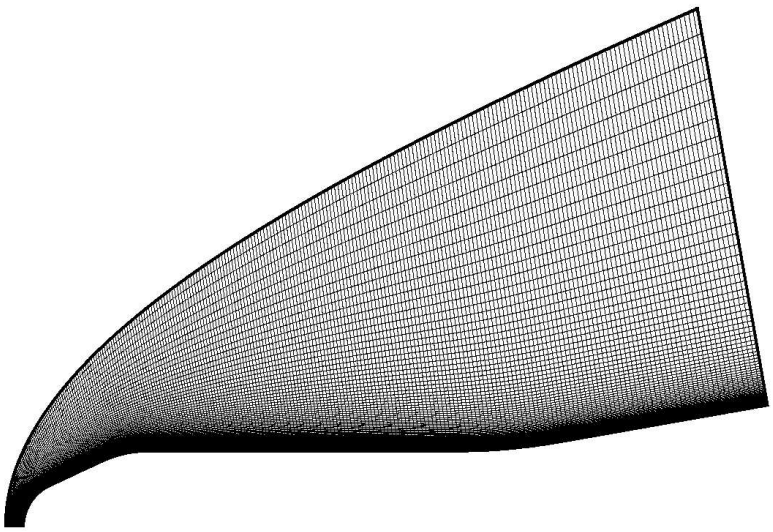

Figure 4.2 — *HB-2 computational grid with clustered cells near the wall.*

Table 4.1 — *Flow conditions for the HB-2 hypersonic configuration.*

Case	001	002	003	004	005
M_∞	17.8	9.59	7.5	5.0	8.5
Re_m	0.02×10^6	2.1×10^6	0.13×10^6	2.32×10^6	0.4×10^6
T_∞(K)	287	52	138.9	138.9	610
T_v (K)	-	-	-	-	610
T_w (K)	287	287	287	287	283
ρ_∞ (Kgm^{-3})	3.95×10^{-4}	5.0×10^{-3}	9.1×10^{-3}	5.1×10^{-3}	2.764×10^{-3}
C_{N_2}	-	-	-	-	0.72
C_{O_2}	-	-	-	-	0.28
C_N	-	-	-	-	-
C_O	-	-	-	-	-
C_{NO}	-	-	-	-	-

Table 4.2 — *Availability of experimental data with reference to wall pressure and heat flux*[63,100,101].

Case	001	002	003	004	005
Pressure	✓	_	✓	✓	_
Heat flux	✓	✓	_	_	✓

4.2 Ideal Gas Computations

Total enthalpy of the ideal gas computations is around 1MJ/Kg and it has been assumed that thermal or chemical non-equilibrium conditions are not present. Figure 4.3(a) to 4.3(d) show the Mach number contours for Cases 001 to 004 (top to bottom and left and to right) and give an insight into the flow field over the test case; it can be observed that a strong shock wave is formed upstream of the body with the second one seen over the cylinder flare junction which is characteristic of HB-2 type flows.

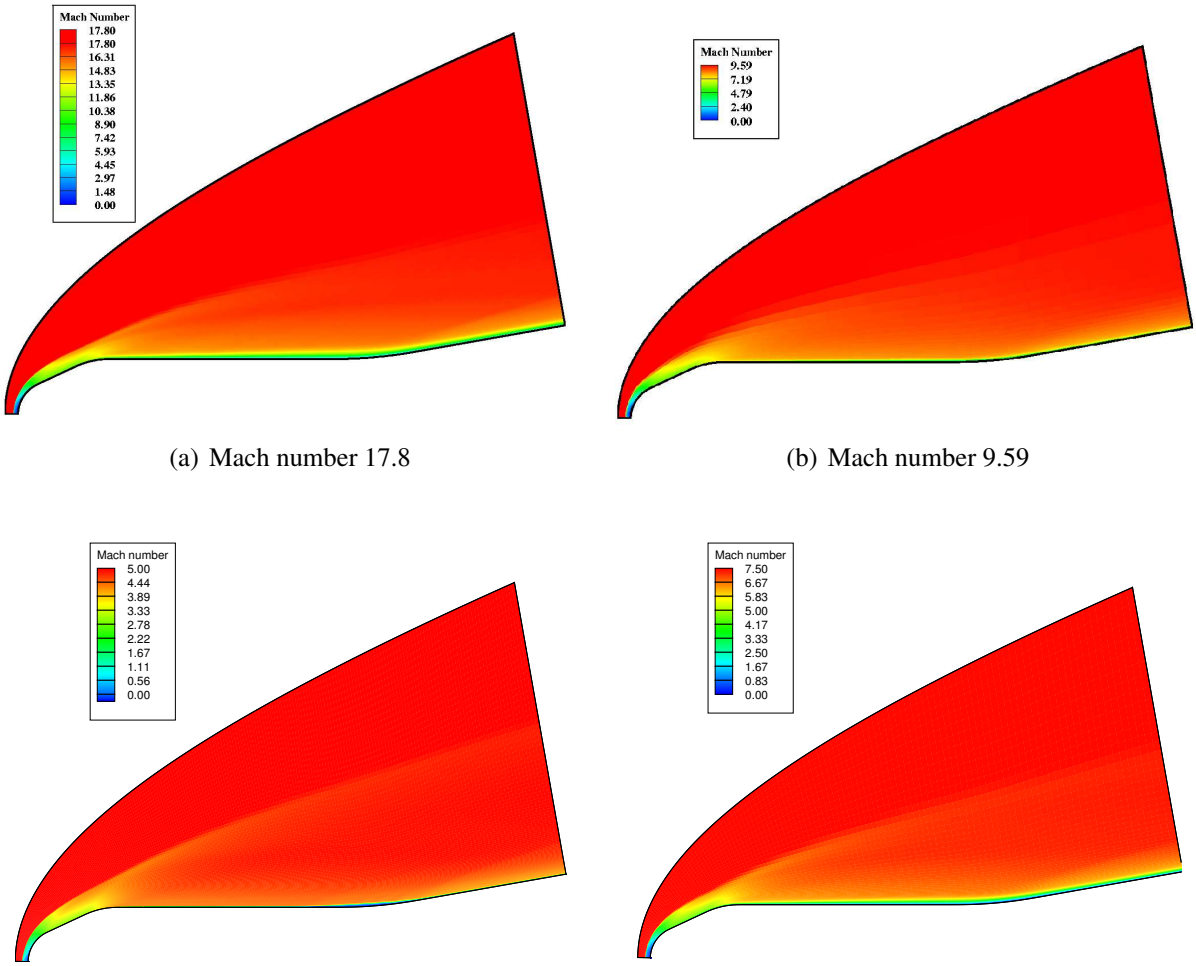

(a) Mach number 17.8

(b) Mach number 9.59

(c) Mach number 7.5

(d) Mach number 5.0

Figure 4.3 — *Mach numbers contours for Case 1 through Case 4.*

Case: 001

A detailed grid convergence study has been carried out for Case 001. The heat transfer to the surface is plotted to examine the improvement in numerical results with the increment in grid density. The results obtained with first order and higher order reconstruction methods over all grid resolutions are also compared (see Figure 4.4 and 4.5). A sequence of grid resolutions has been used, with 256×128, 128×48, and 98× 48 cells, which are referred below as fine, medium, and coarse grids, respectively. Utmost care has been taken to ensure that cells adjacent to the wall have grid lines perpendicular to it.

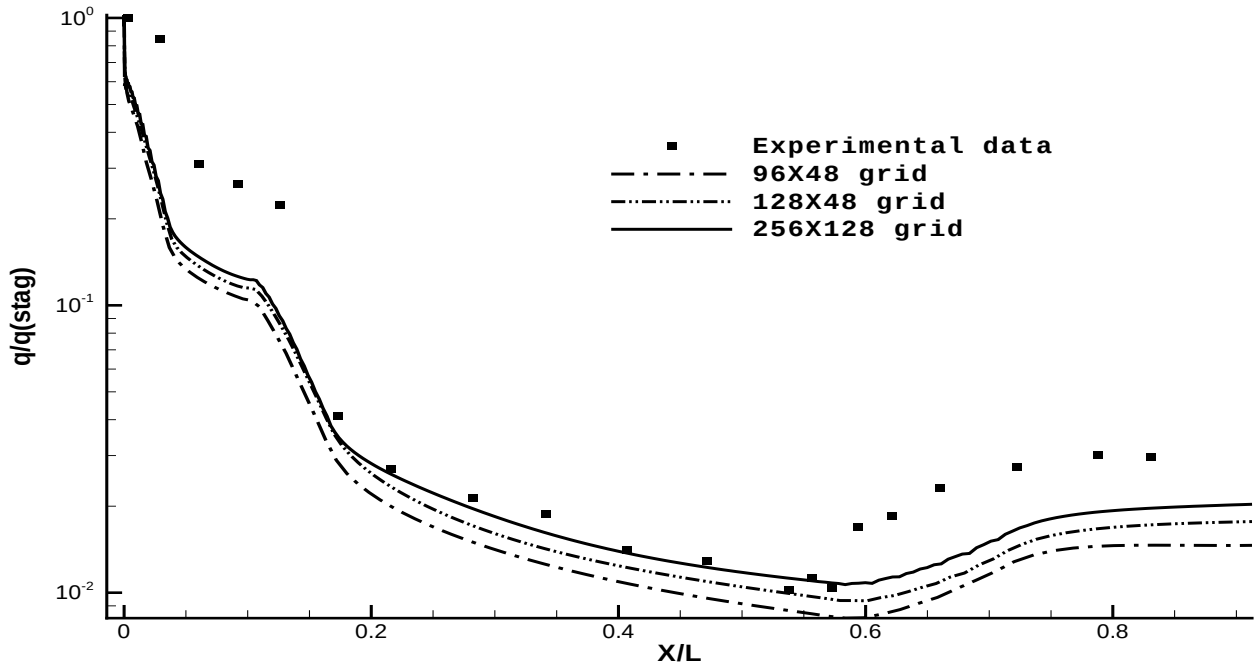

Figure 4.4 — *Heat transfer rate computed on different grids with first order reconstruction accuracy for Case 001: the heat transfer is plotted along the X-axis rather than along the surface of the test case.*

The heat transfer to the nose region at the front and flare region at the back is under predicted by all schemes over all grid resolutions (see Figure 4.4). As expected, the grid resolution influences the computational results for all orders of accuracy. The overall agreement between predicted values by all TVD schemes over the cylindrical sections via the use of fine mesh and the experiment is good (see Figures 4.5(a) through 4.5(c)).

Further investigations are essential to clarify these discrepancies as the front part of the HB-2 flare experiences the highest heat transfer values compared to the rest of the body during a hypersonic flight. As the exact details of the free stream enthalpy conditions are not clear (see experimental work by Gray *et al*[63]), it is difficult to ascertain if the computations under chemically reacting gas condition will yield a better comparison with the experimental data. However, it is worthwhile to investigate the problem, under the assumption of chemically reacting gas, to establish if there is any improvement. The results obtained for the WENO scheme are not shown due to the oscillations present, and the WENO scheme does not appear to perform well at such a high Mach number equal to 17.8. It seems that the design of WENO methods for such demanding applications needs further investigation, which is beyond the scope of this thesis.

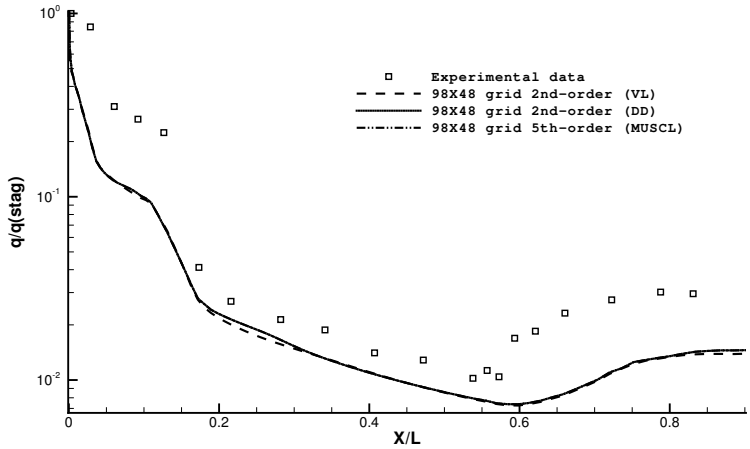

(a) 98×48

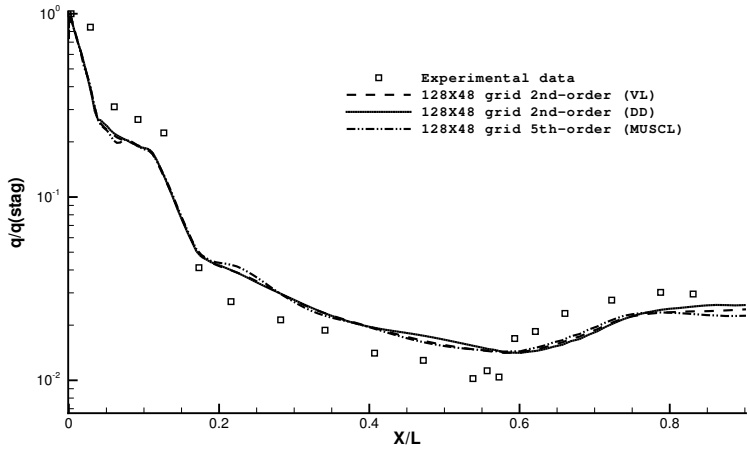

(b) 128×48

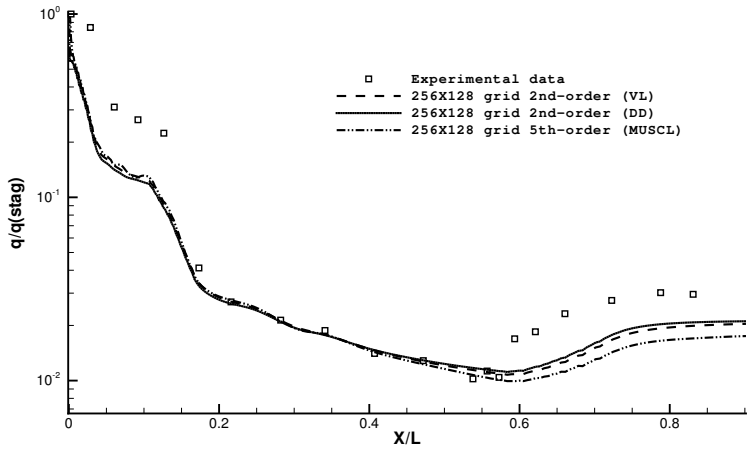

(c) 256×128

Figure 4.5 — *Heat transfer distribution calculated using all grid resolutions for Case 001.*

Figures 4.6(a) to 4.6(c) shows the pressure results obtained for the MUSCL 2^{nd}-(two different limiters) and 5^{th}-order reconstruction schemes over all grid resolutions. The overall agreement between the computational results and the experimental data is good, with minor discrepancies in the front region of the cylindrical section. The 2^{nd}-order (DD limiter) MUSCL gives overall the best results for the heat transfer distribution. The schemes give similar results for the wall pressure. The computations via the use of 5^{th}- and 9^{th} -order WENO scheme were also considered; however, oscillations materialised during the runs which effected the process of convergence, therefore, the results for this scheme are not included.

The stagnation pressures for the second-order(VL), second-order(DD), and fifth-order MUSCL schemes are very similar and equal to 12.1, 12, and 12KPa, respectively, while the stagnation heat fluxes are 4050,4260 and 3750 KW/m^2, respectively. It should be noted that the above values correspond to the values of the first cell adjacent to the wall, where as in the case of finite volume method, the values are stored. Unfortunately, for this case the experimental stagnation values are not available for the purpose of comparison with the computational results.

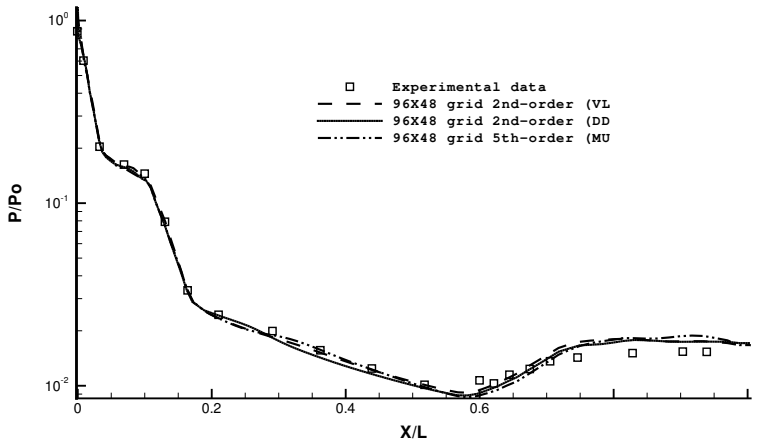

(a) 98×48

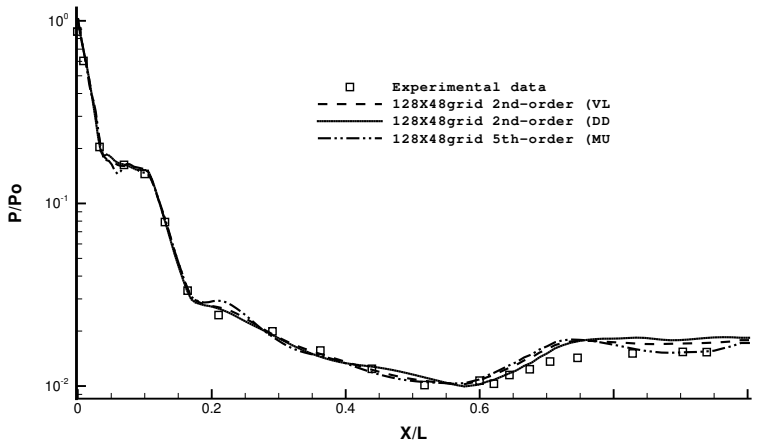

(b) 128×48

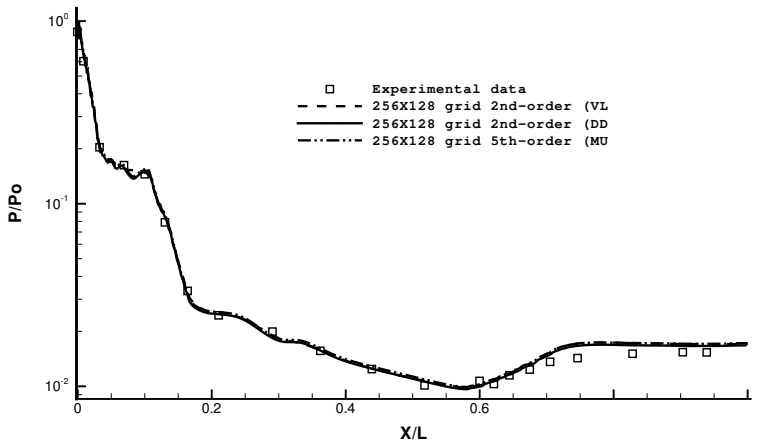

(c) 256×128

Figure 4.6 — *Pressure distribution calculated using all grid resolutions for Case 001.*

Case: 002

The heat transfer results for Case 002 on the 128×48 and 256×96 grids are shown in Figure 4.7 (a) and (b), respectively. The VL and DD limiters gave identical results, thus only the results with the VL limiter are shown. Moreover, the 9^{th}-order WENO was unstable for this case too without being able to satisfactorily converge.

According to Kuchiishi (2006)[101], the experimental heat flux stagnation value is 137.32kW/m^2 (Sec.4 in the experimental report). The predicted value in this study was found to be 127.2 and 118.5kW/m^2. for the second- and fifth-order MUSCL schemes, respectively. Similar to the case 1, the stagnation values are calculated from the first cell next to the wall which compares better in terms of position with the station 3 of the experiment corresponding to heat flux value of 126.77kW/m^2. With regards to the heat flux stagnation value, the second-order MUSCL scheme agrees better the experiment than fifth-order MUSCL scheme. With respect to dimensionless heat flux distribution, the comparison with the experiment is satisfactory and the fifth-order WENO performs overall better than the second-order MUSCL scheme.

In comparison to Case 001, the heat transfer predictions at the nose and in the flare region are significantly better for this case. Numerical experiments were also performed with the 5^{th}-order MUSCL scheme; however, the scheme resulted in spurious oscillations. When the grid resolution was increased, the oscillations were reduced but not completely, thus leading to convergence problems. The 2^{nd}-order MUSCL using the DD limiter gave exactly the same results as the VL limiter. Hence, only the results of the VL limiter are presented in Figure 4.7.

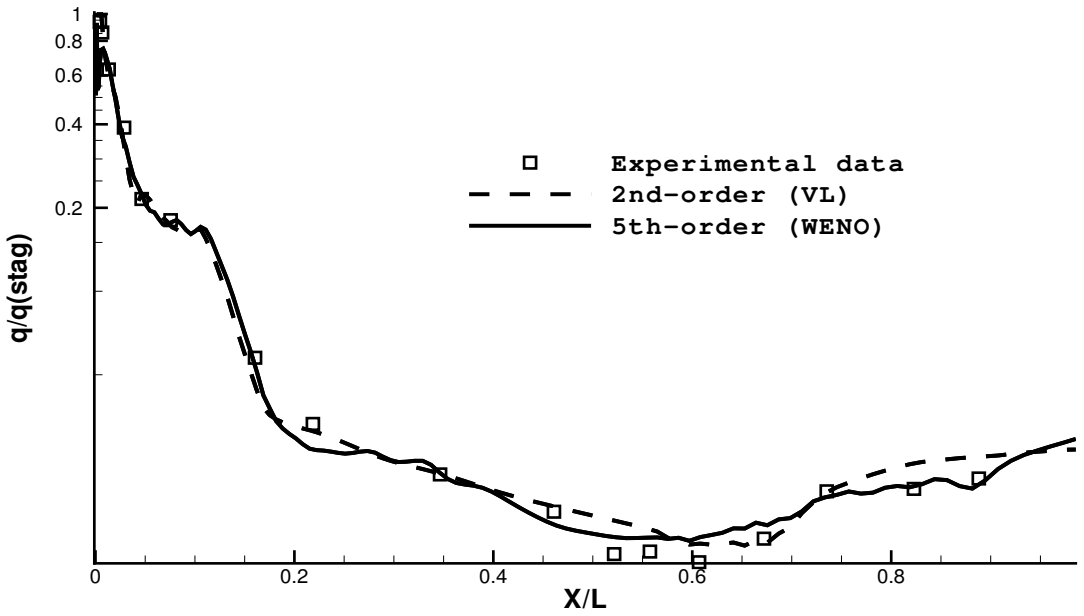

(a) 128×48

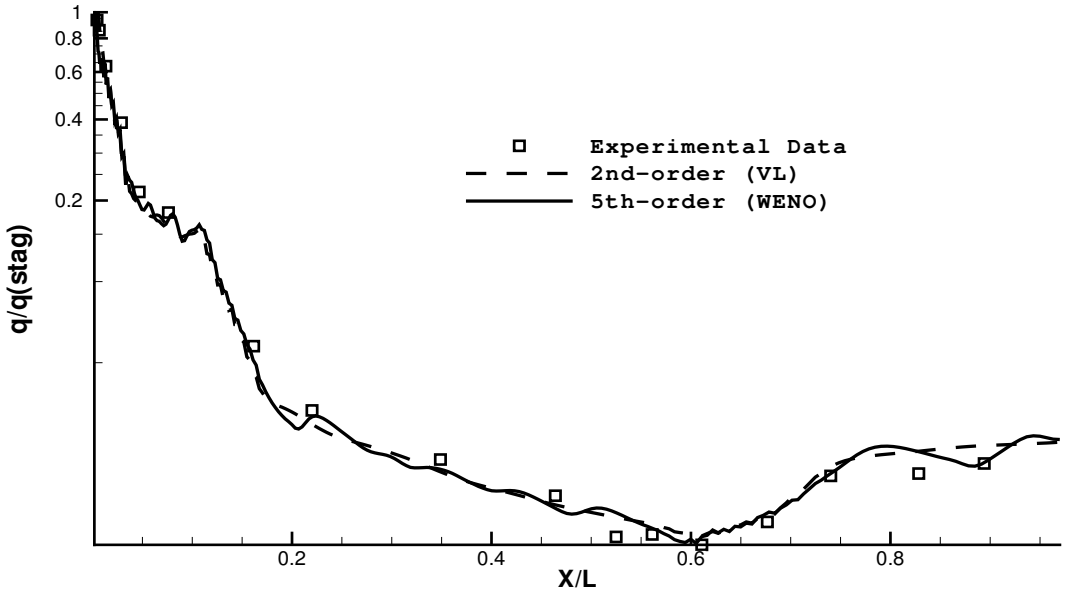

(b) 256×128

Figure 4.7 — *Heat transfer distribution calculated using all grid resolutions for Case 002.*

Case: 003

For Case 003, all methods gave very similar results for the pressure distribution (see Figure 4.8). For this case, even a first-order scheme gives satisfactory results. Therefore, Figure 4.8 presents indicative results from the 1^{st}-order, 2^{nd}-order MUSCL, and 9^{th}order WENO.

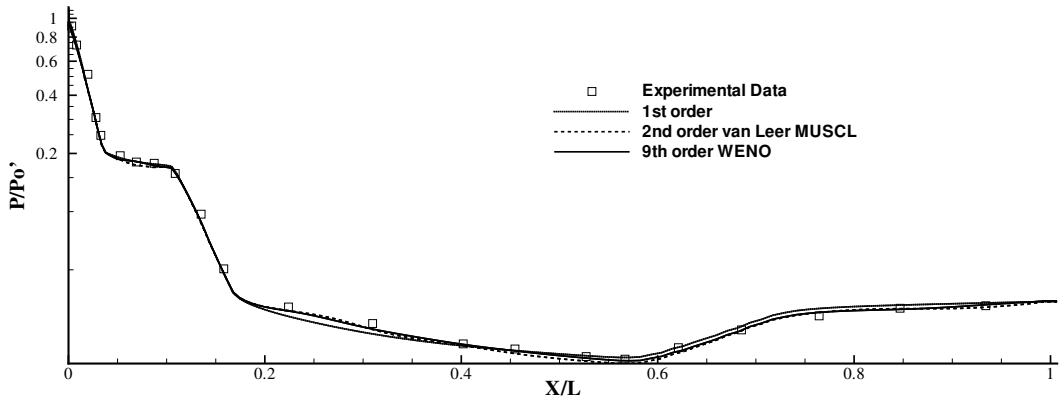

Figure 4.8 — *Pressure distribution on the fine grid for Case 003.*

The 5^{th}-order MUSCL, 2^{nd}-order MUSCL(DD-limiter), and 5^{th}-order WENO scheme also gave similar results, thus they are not included in the graph. The pressure stagnation values for the first- second- and ninth-order schemes were computed as 90, 85, and 95kPa, respectively.

Case: 004

Case 004 is different from the previous cases, because it features separation around the cylinder flare junction (see Figure 4.9). This is indicated in the pressure distribution by a 'double-step' profile (Figures 4.10 and 4.11). Using 1^{st}-order of accuracy the separation cannot be captured. The re-attachment point is well-matched to experiment, although the total separation length is somewhat smaller. The 9th-order WENO captures better the separation point; however, it shifts the re-attachment point downstream. The 2^{nd}-order MUSCL gives better results for the re-attachment point.

As regards the 5^{th}-order MUSCL and 2^{nd}-order MUSCL (DD limiter), these schemes gave almost identical results with the 2^{nd}-order MUSCL (VL limiter); hence, they are not included

in Figures 4.10 and 4.11. It should be noted that past research[6,43,162] has shown that the DD limiter is overall more robust than the VL limiter for a wide range of Mach numbers. For Case 4, the pressure stagnation values for the first- second- and ninth-order schemes are 38, 38, and 38.6 kPa, respectively.

Finally, the CPU requirement for the 9th-order WENO scheme compared to 2^{nd}-order MUSCL increases by a factor of two and three on the coarse and fine grid resolutions, respectively. The 5^{th}-order MUSCL requires only moderate CPU increase compared to 2^{nd}-order schemes.

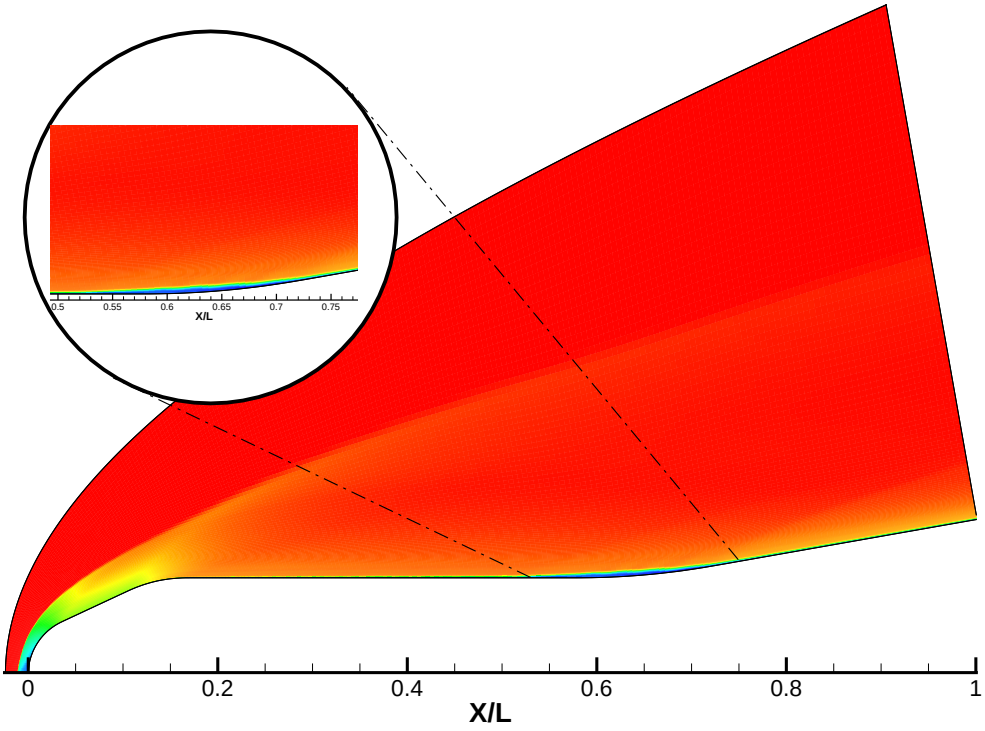

Figure 4.9 — *Mach number contours and enlarged separation region for Case 4.*

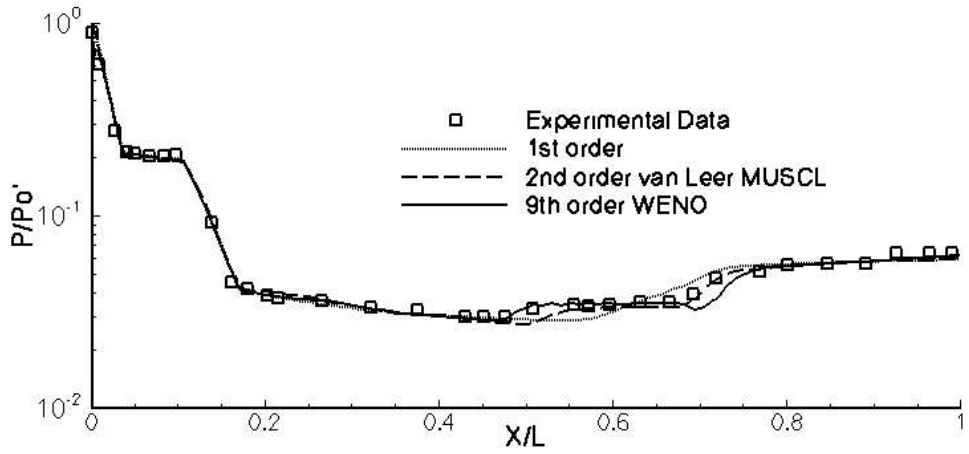

Figure 4.10 — *Pressure distributions for Case 4.*

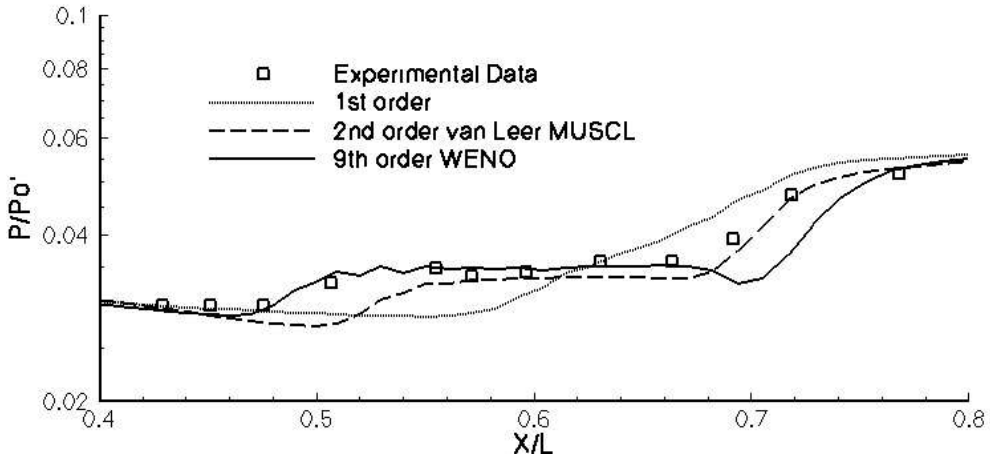

Figure 4.11 — *Enlargement of pressure distribution at cylinder flare transaction for Case 4.*

4.2.1 Comparison of CNS3D and Commercial software FLUENT

A comparison study has also been conducted to analyse the effectiveness of the computational code CNS3D against the commercial software FLUENT. Free stream conditions used for Case 003 and 004 in the previous sections have been used for the study. Furthermore, two grid resolutions, 64×48 and 128×96, were employed for the simulations.

Figures 4.12 and 4.13 show the normalised results against experimental data for the first and second order simulations obtained using CNS3D (Figures 4.12(a) & 4.13(a)) as well as FLUENT (Figures 4.12(b) & 4.13(b)) for case 003. There is little difference between the either code

or the experimental data. The slight discrepancies are essentially resolved in the higher-order simulations (Figure 4.14); however, it is worth noting that FLUENT is marginally less able to handle the coarser mesh at second order. Elsewise the result is fairly consistent, and arguably not far from grid-converged.

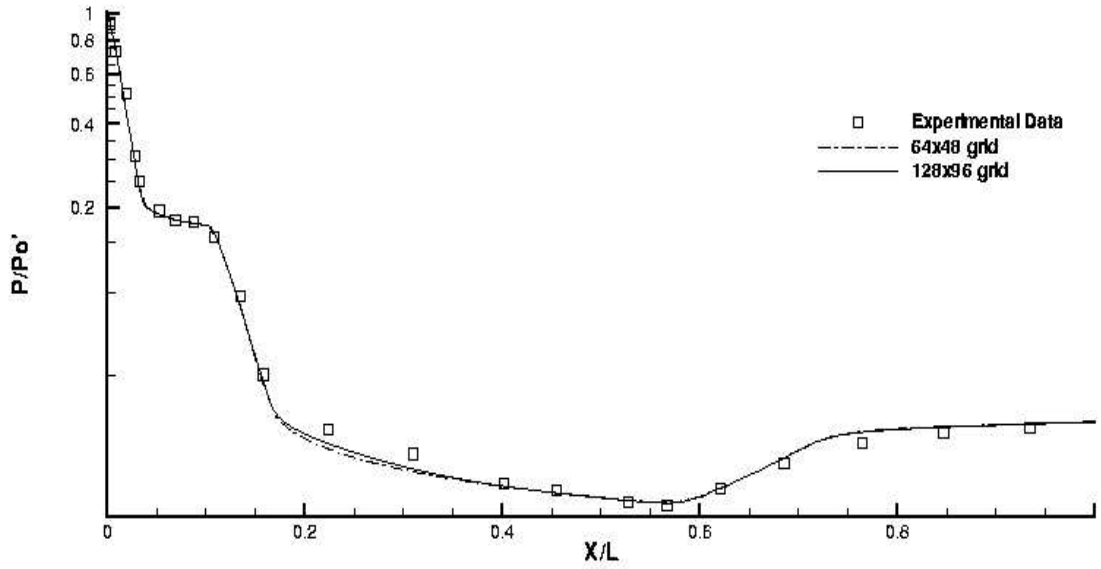

(a) CNS3D:1st-order

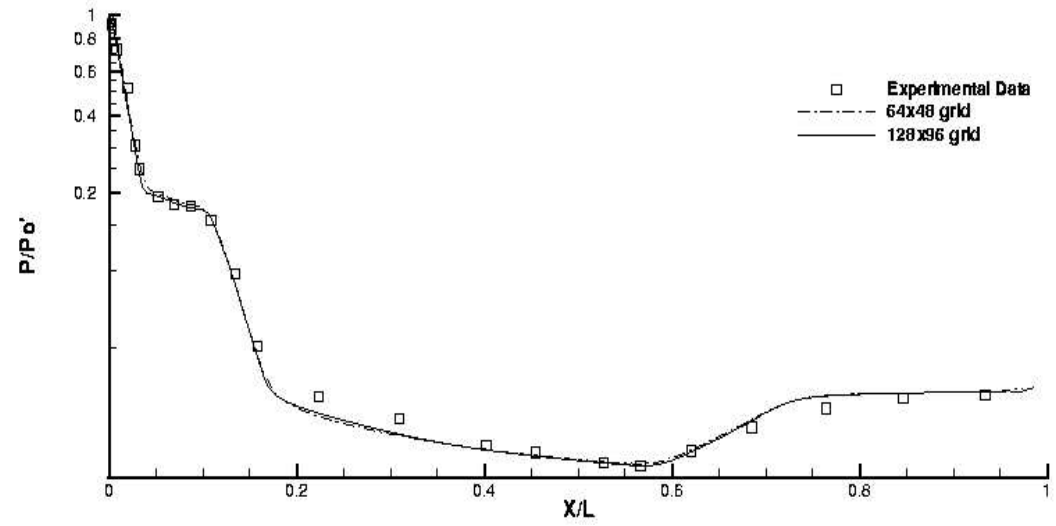

(b) FLUENT:1st-order

Figure 4.12 — *Pressure distribution for HB-2 for the case 003 for CNS3D and FLUENT at both grid resolutions: 1st -order reconstruction accuracy.*

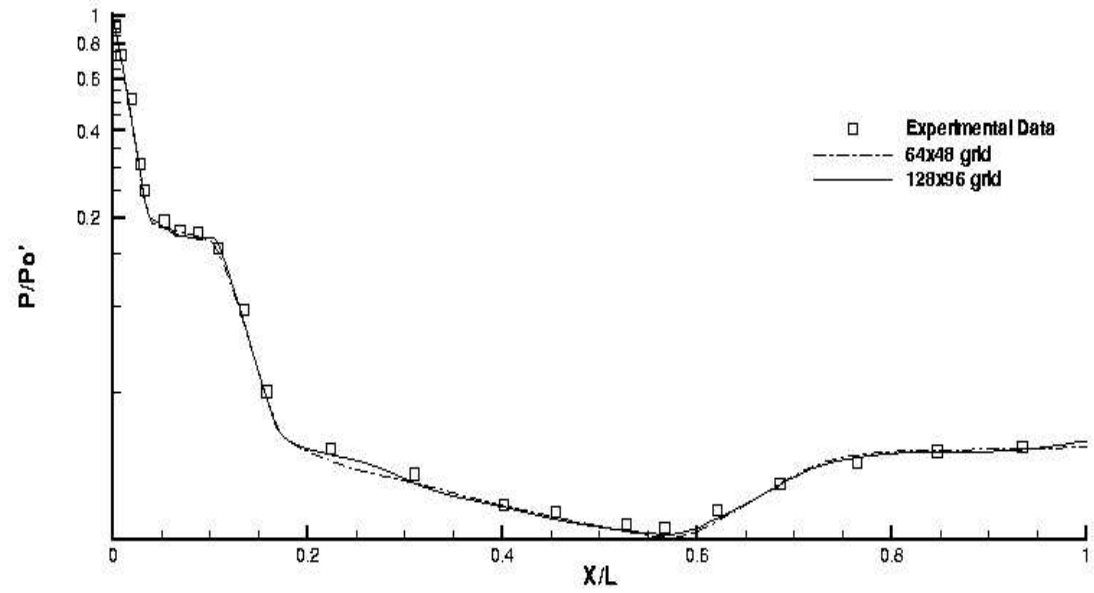

(a) CNS3D:2^{nd}-order

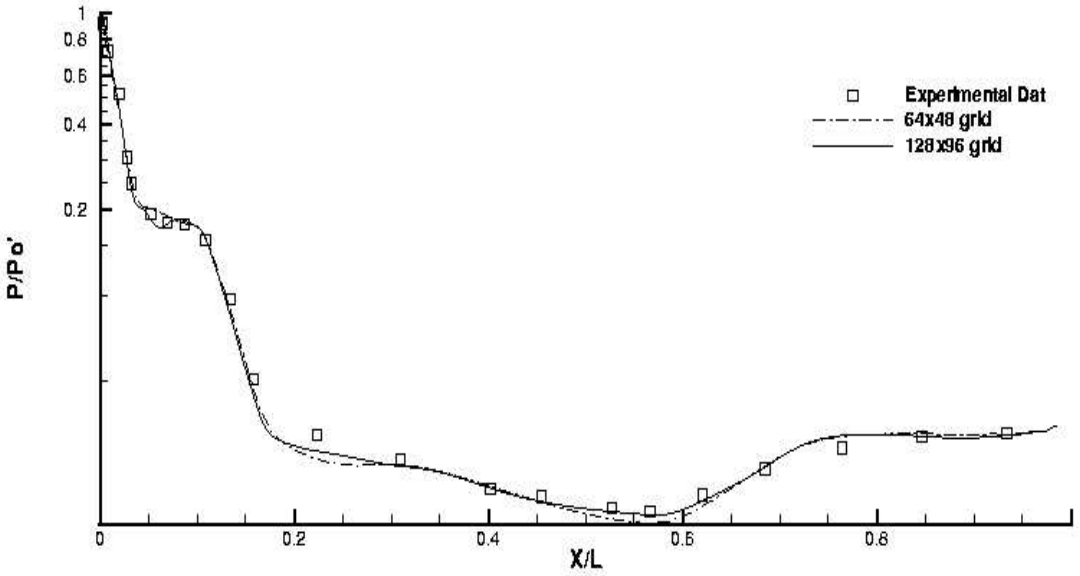

(b) FLUENT:2^{nd}-order

Figure 4.13 — *Pressure distribution for HB-2 for the case 003 for CNS3D and FLUENT at both grid resolutions: 2^{nd} -order reconstruction accuracy.*

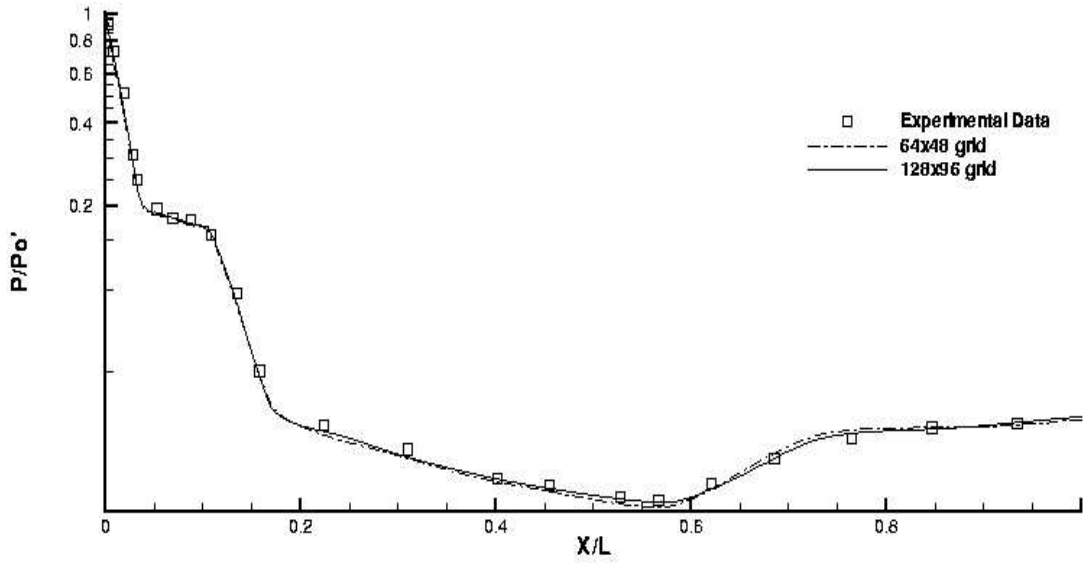

Figure 4.14 — *Pressure distribution for the case 003 using WENO ninth-order in CNS3D.*

When comparing the behaviour of both CNS3D (Figures 4.15(a) & 4.16(a)) and FLUENT (Figures 4.15(b) & 4.16(b)) for the case 004, at first order, both codes fail to capture any of the experimentally observed behaviour around the cylinder-flare transition. Again, there is little difference between the two solvers, and the increased grid resolution does not significantly change the results.

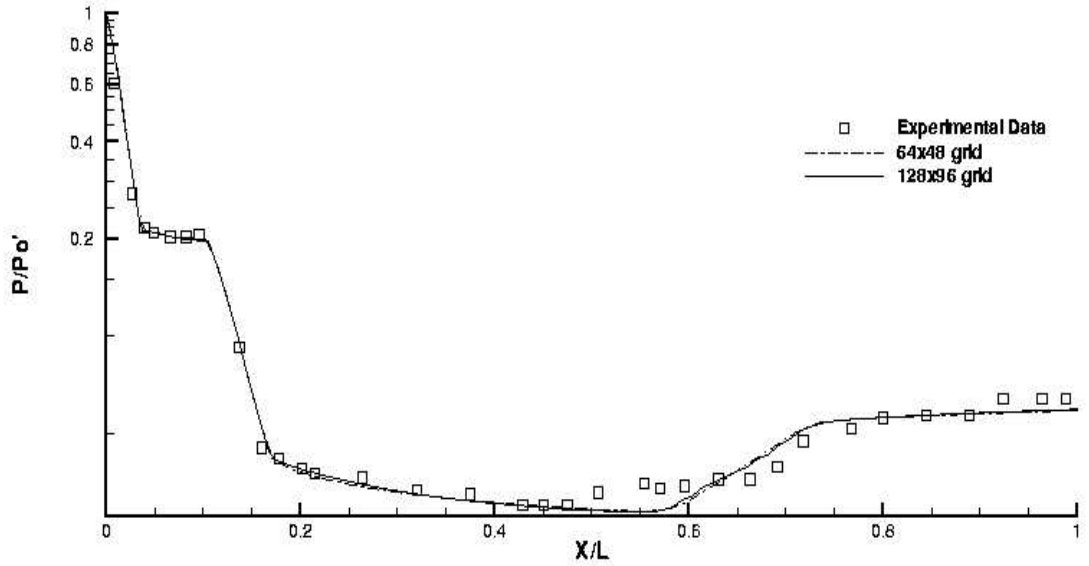

(a) CNS3D :1st-order

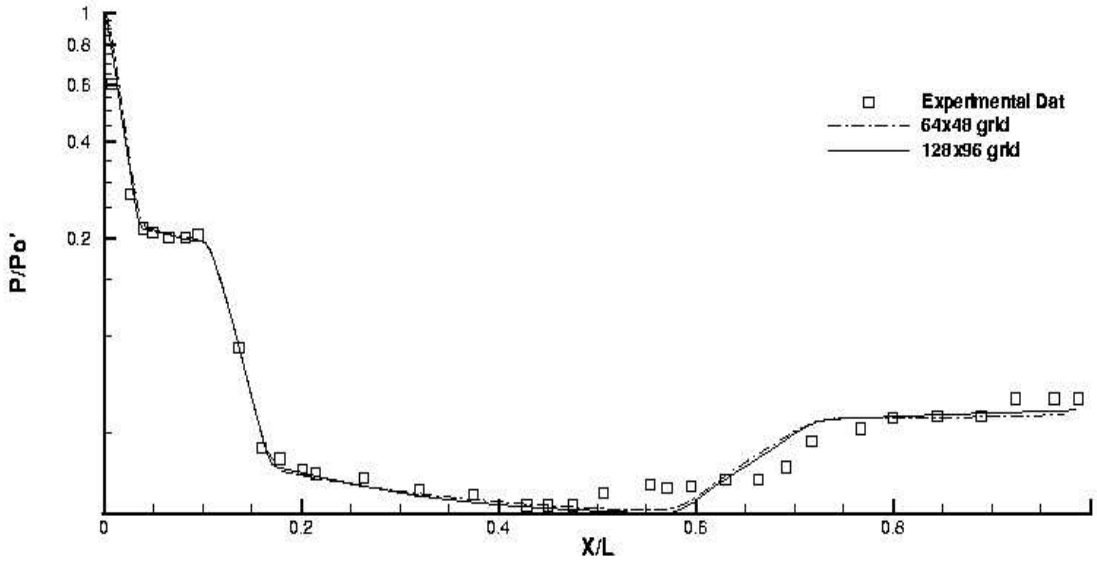

(b) FLUENT:1st-order

Figure 4.15 — *Pressure distribution for case 004 for CNS3D and FLUENT at both grid resolutions: 1st -order reconstruction accuracy.*

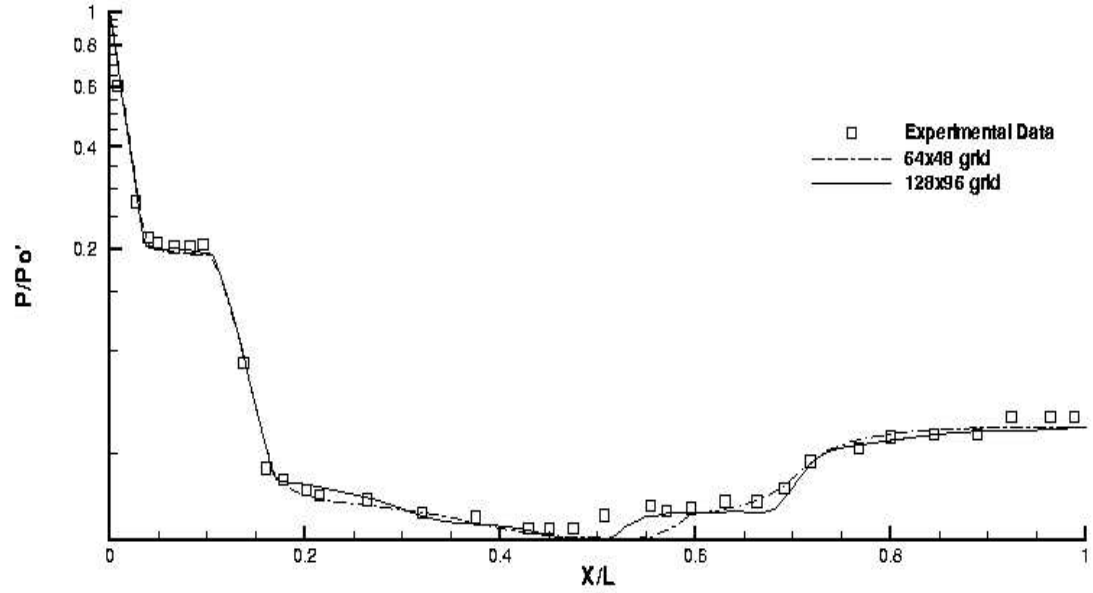

(a) CNS3D :2^{nd}-order

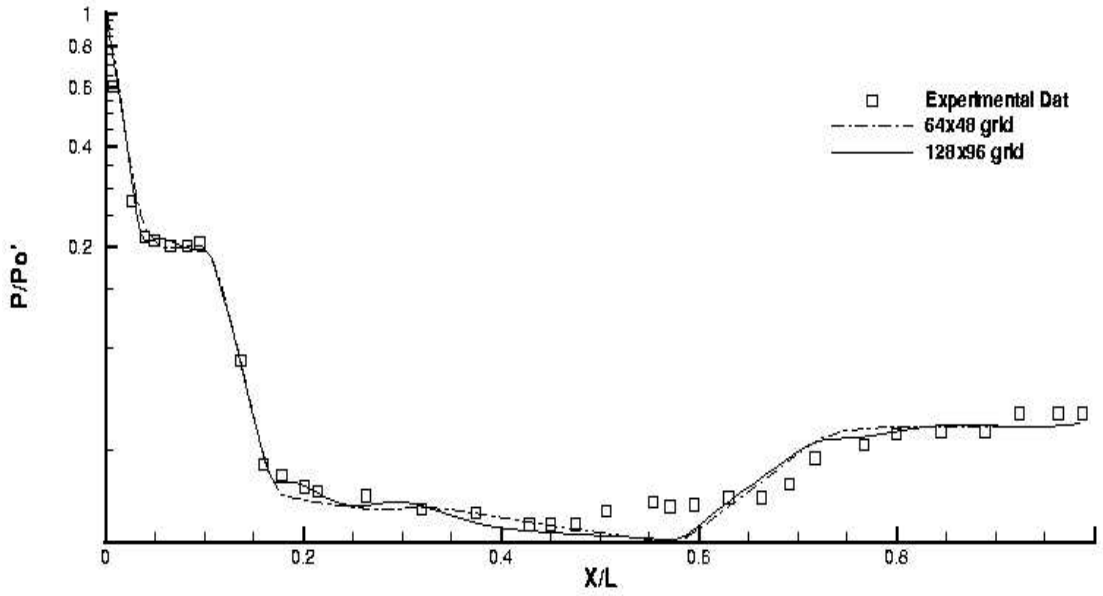

(b) FLUENT:2^{nd}-order

Figure 4.16 — *Pressure distribution for case 004 for CNS3D and FLUENT at both grid resolutions: 2^{nd}-order reconstruction accuracy..*

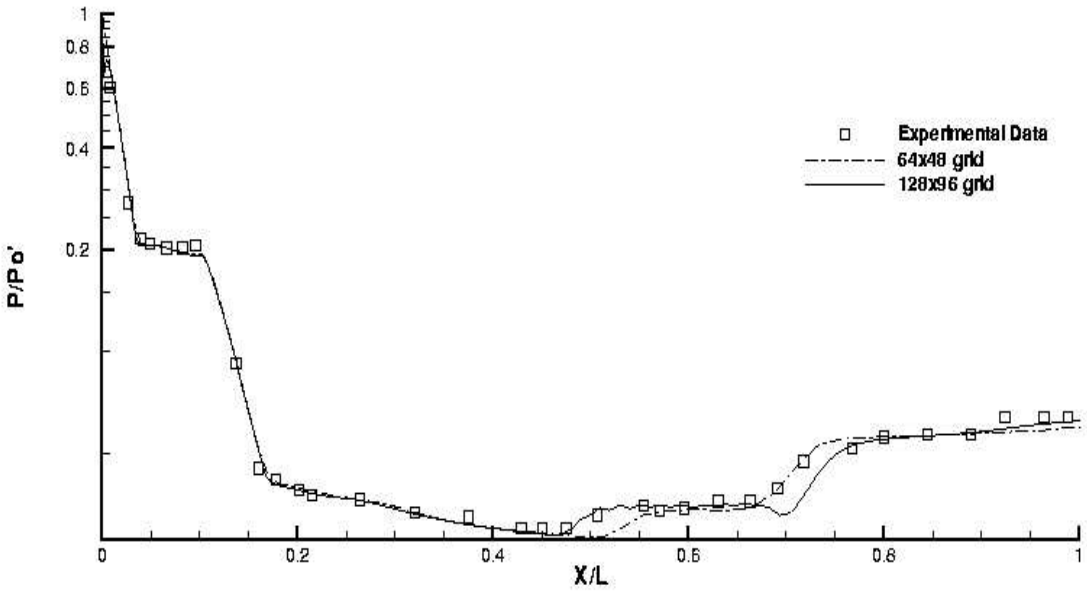

Figure 4.17 — *Pressure distribution for case 004 using WENO ninth-order in CNS3D.*

This is not the case at second-order. Both solvers capture better the observed flow past the shoulder of the cone-cylinder, while FLUENT seems not to be capturing any of the main separations, and clearly indicated that CNS3D has the 'double-step' profile characteristic of a separation bubble. The re-attachment point is well-matched to the experiment, although the total separation length is somewhat smaller. The results obtained for the higher-order schemes have been presented in Figure 4.17.

4.3 Chemically Reacting Gas Computations

In this section, the results obtained for Case 005 conducted at a total enthalpy of 8MJ/kg are presented. The schematic of the test case is presented in Figure 4.1 and the simulated test conditions are listed in Table 4.1. The computations are carried out using two grids (resolutions: 128×48 and 256×96).

The numerical results obtained are presented below. The contours of Mach number, pressure, and two temperatures are plotted in Figure 4.18 $\sim$ Figure 4.21 respectively. As expected, the Mach number recorded at the nose, behind the shock is subsonic; consequently, the maximum pressure is also predicted at the stagnation point. The flow continues to expand while moving

downstream where the calculated pressure values decreases. Here, the shock, stand-off distance as well as the general shape of the shock layer near the nose can be clearly observed.

As the Mach number reduces drastically before the stagnation point, the kinetic energy of the flow reduces while the translational-rotational as well as vibrational temperatures rise (see Figures 4.20 & 4.21). Just behind the shock, upstream of the stagnation point, an adverse gradient of translational temperature can be observed. To further illustrate this behaviour, both temperatures are plotted along the stagnation streamline (see Figure 4.22(a)).

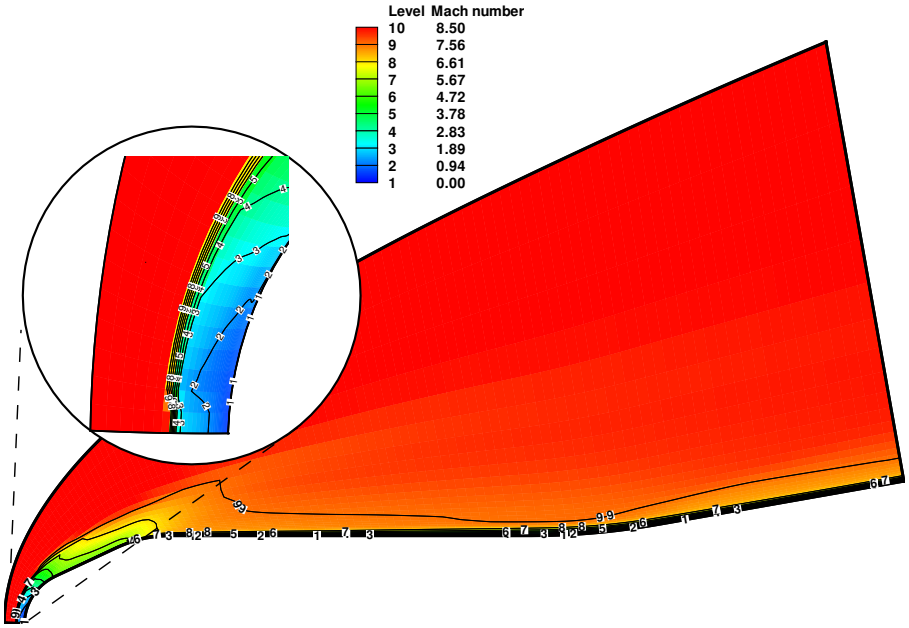

Figure 4.18 — *Flow contours of Mach number highlighting the flow features; the nose region is enlarged and displays the conditions at the stagnation region.*

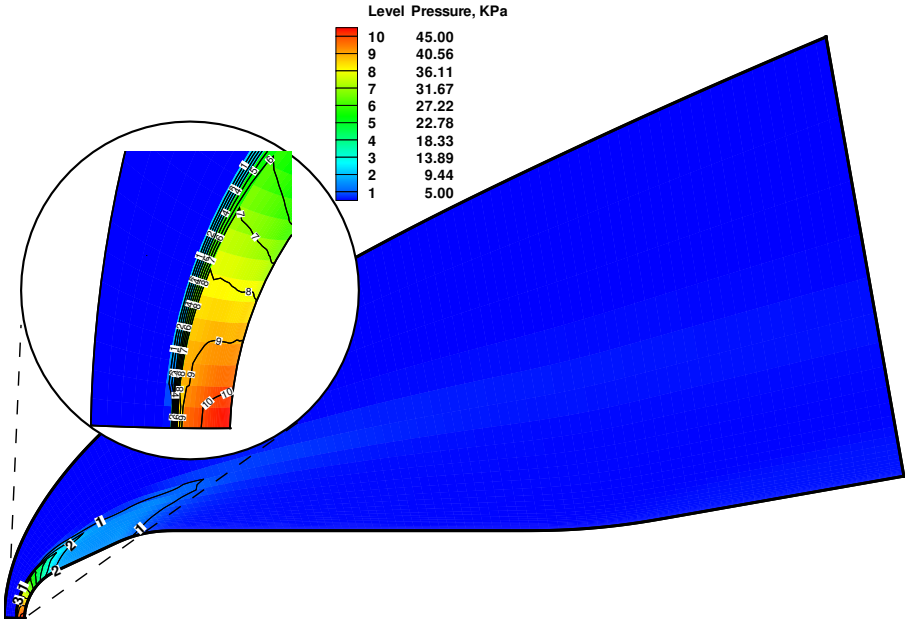

Figure 4.19 — *Flow contours of pressure highlighting the flow features; the nose region is enlarged and displays the conditions at the stagnation region.*

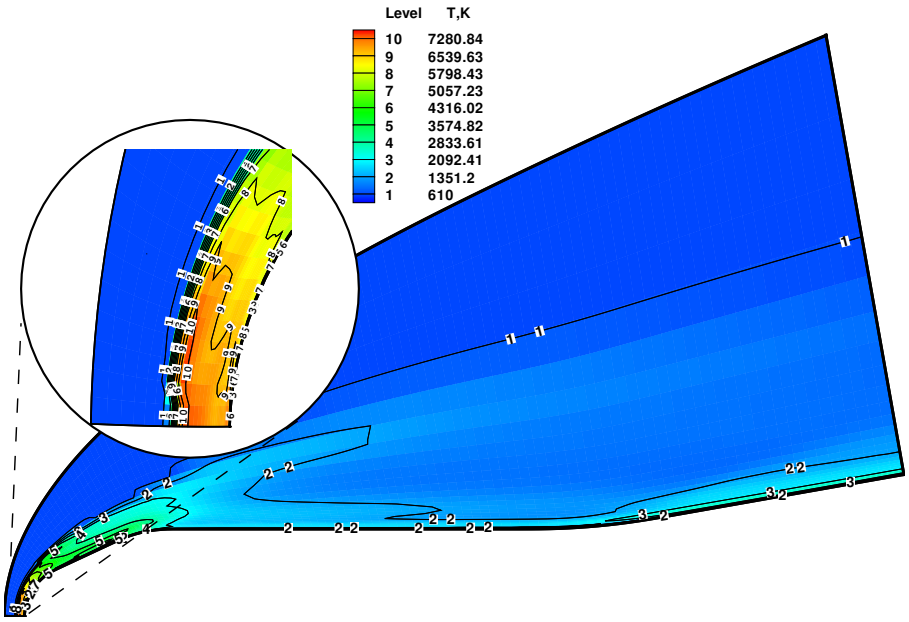

Figure 4.20 — *Flow contours of tranlational-rotational temperature.*

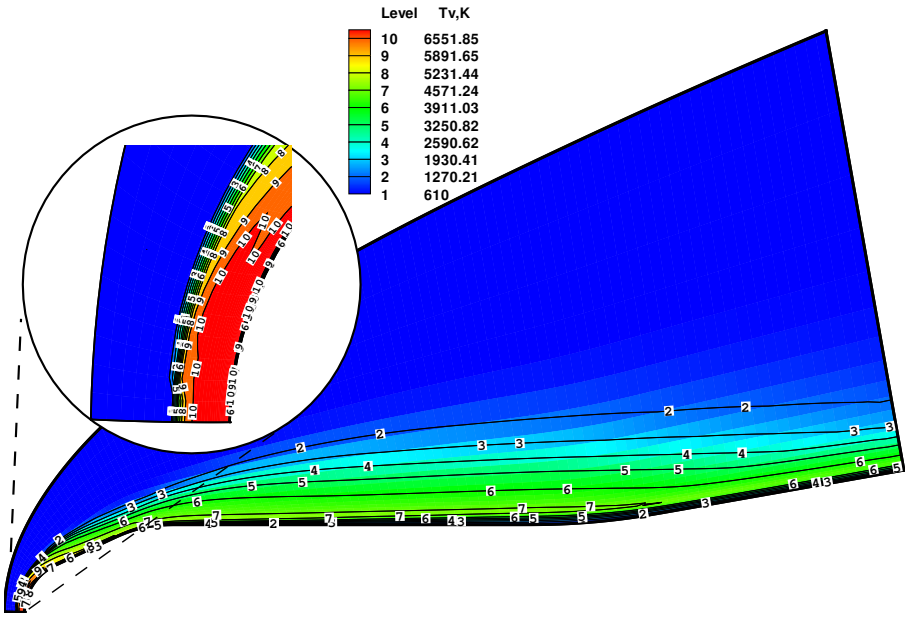

Figure 4.21 — *Flow contours of vibrational temperature.*

As it was explained earlier, the kinetic energy of the flow decreases as the Mach number reduces to a subsonic value upstream of the nose region. The excess energy instantaneously gets diverted to other energy modes; translational-rotational and vibrational energy modes are populated with the excess energy. Due to this sudden spike in two temperatures the rate of particle collisions as well as internal vibrations of the molecules increases rapidly. As a result, the chemical and thermal non-equilibrium effects are initiated in the stagnation region. This causes the gases in the region to dissociate; these phenomena can be observed in the case 005.

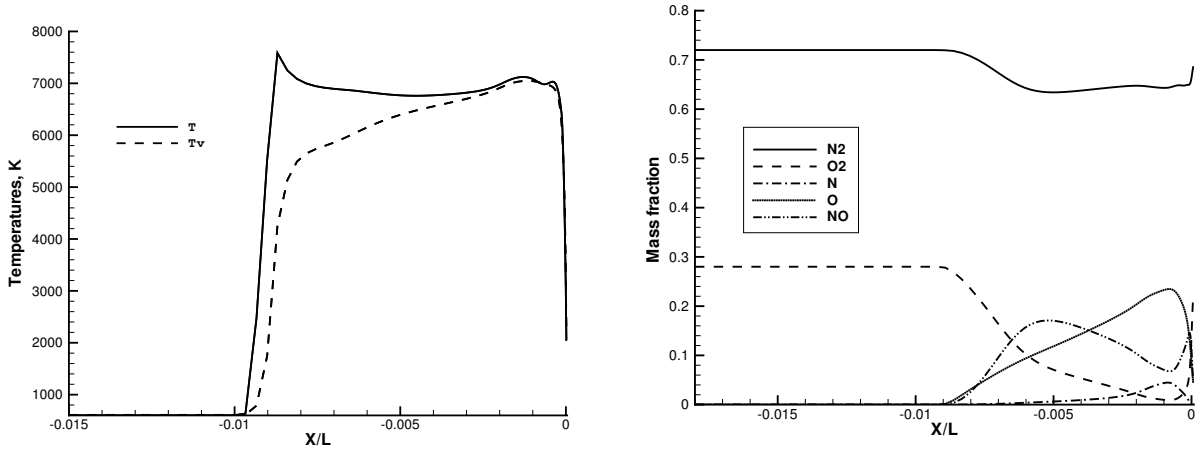

(a) Two-temperatures (b) Mass fraction of species

Figure 4.22 — *Translational-rotational (T) and vibrational (T_V) temperatures as well as mass fraction plotted along the stagnation stream line.*

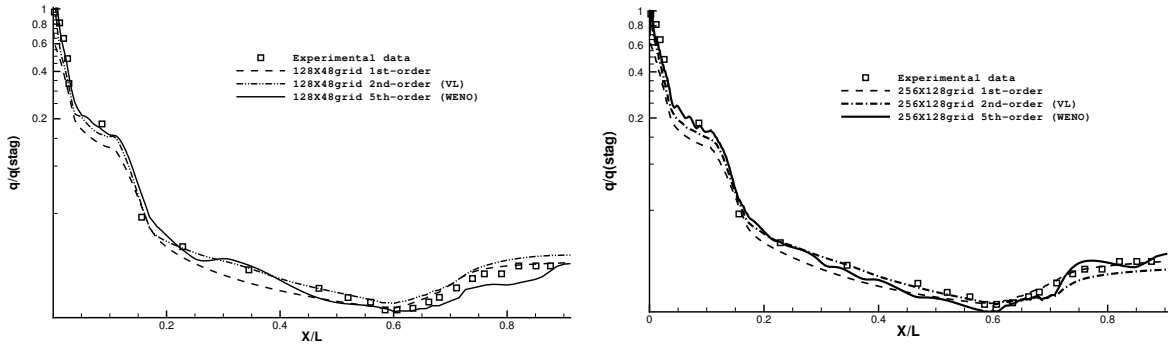

(a) (b)

Figure 4.23 — *The heat transfer to the surface plotted for all grid resolutions.*

The evolution of the mass fractions along the stagnation streamline is presented in Figure 4.22. The Nitrogen and Oxygen molecules are dissociated forming Nitrogen and Oxygen atoms respectively. Oxygen molecules dissociate almost completely forming Oxygen atoms. Furthermore, oxygen and nitrogen atoms combine to form NO molecules. As there is a clear difference between the two temperatures, the two temperature model gives an insight into the behaviour of the energy modes within the flow.

Finally, Figure 4.23 shows the comparison for the calculated heat flux to the wall with experimental data for all three reconstruction techniques. The free stream translational-rotational temperature utilised in the experiment was not available to the investigator. In fact, only Mach

number and Reynolds number have been explicitly stated in the literature for this case and the other free stream conditions had to be estimated. Therefore, the free stream values for both temperatures were taken as 610K; it was assumed that the temperature was sufficient to trigger chemical dissociation and was chosen based on past experiences.

The absolute values of heat flux for the experiment and the computations at the stagnation point are incomparable due to the possible discrepancies in the free stream conditions. However, the desired shape of the heat flux over the surface, where the maximum is visible at the nose, is predicted correctly by the computations (see Figure 4.23).

When comparing the normalised values, that is q/q_0, the obtained numerical results show good agreement with experimental values on the first half of the body. The most accurate results are provided by the 2^{nd} order TVD method with the van Leer slope limiter, which is somewhat more accurate than the WENO methods. In fact, the WENO results contain mild oscillations, indicating that for the geometry it may not be the most suitable scheme. Both high-order schemes are still much better than the 1st order Godunov method. Further investigation of this test case has been carried out using an ablation wall boundary condition; the results are presented in Chapter 6.

4.4 Efficiency and Robustness

As it was discussed previously, it is a primary requirement of CFD codes to be efficient and robust in order to complement or to act as an alternative to the physical experiments[118]. Presently, the numerical simulations depend heavily on the computer hardware employed, and the effective algorithms that describe the physical problem investigated. The ideal way of establishing the performance of a numerical method is to evaluate the time to achieve a converged solution; many different factors such as efficiency of the algorithm, the use of a particular hardware platform at a percentage of its peak speed, etc have to be taken into account. Due to the shear number of variables that may potentially have an effect on the computations, it is a difficult task to perform comparisons using this method. An alternative, more universal benchmark used by researchers is the raw computational speed, typically expressed in FLoating-point OPerations per Second (FLOPS)[118].

In this thesis, to make comparative conclusions about the relative efficiency of the various numerical methods, runs were conducted on a single processor using the finer HB-2 grid to ascertain the cost per iteration. Even though, the flows are treated as steady, it is quite possible that the instabilities are present within the solution; the observation that, during the course of the simulations steady results emerge followed by a long period of slight and ever-reducing oscillation, is the reason for this supposition. Moreover, it is somewhat difficult to establish the efficiency and robustness for both 5^{th}- and 9^{th}- order WENO schemes, due to the *local order reduction* technique employed (see Section 3.3.3) in CNS3D code.

Therefore, this study is intended as a guide to show an overall relative effect on performance when increasing the order of reconstruction accuracy. The values presented are for both unmodified (perfect gas) and modified versions of CNS3D code, as well as commercial code FLUENT (see Table 4.3).

Table 4.3 — *Approximate evaluation of computational cost with respect to CNS3D first-order.*

Order of reconstruction	1^{st} -order	2^{nd} -order	2^{nd} -order (FLUENT)	5^{th} -order	9^{th} -order
CNS3D	1.00	1.088	1.109	1.38	1.893
Modified-CNS3D	1.00	1.092	-	1.46	2.18

Unsurprisingly, the results show that, for both versions of CNS3D, the ninth-order scheme requires more CPU time per iteration. However, the performance of 5^{th}- order WENO scheme is more interesting, as it is halfway between, values of 2^{nd}-order VL and 9^{th}-order WENO schemes. Also, the robustness observed throughout the simulations over a range of Mach numbers suggest that WENO scheme is far more reliable with 5^{th}- order reconstruction accuracy.

The commercial flow solver FLUENT is more robust compared to CNS3D as it has algorithms forcing a stable solution; employing these methods to force stability is questionable. In the case of CNS3D, when producing a result deemed unphysical, the code would simply terminated the calculation process, forcing the the user to investigate and rectify the problem. Therefore, extracting conclusions from these results must be done with caution.

When comparing the computational time, between modified and unmodified versions of CNS3D, it is apparent that the computational times have increased due to the burden of having to perform additional calculations. It is clear that the computational costs, associated with increasing the

grid resolutions when simulating real gas effects, are comparatively much higher than in ideal gas computations. Therefore, as a compromise between accuracy, efficiency, and robustness, it is clear that the high-order methods are more suited to be applied to real gas problems. In summary the high-order methods, specially 5^{th} -order WENO, is exceedingly good value in terms of their overall efficacy on coarse grids and capable of gaining better accuracy with half the number of grid points in each direction consistent with observations in other flow applications of this code.

4.5 Summary

Numerical experiments from the implementation of 2nd-, 5th- and 9th-order reconstruction schemes for hypersonic flows around the HB-2 hypersonic configuration were presented for free stream Mach numbers ranging from 5 to 17.8, under perfect and real gas assumptions.

With regards to perfect gas flows, the results show that WENO schemes can be unstable for Mach numbers above 10; however, they seem to be more accurate than 2nd-order methods for Mach numbers less than 10. For the HB-2 geometry the 5th- and 2nd-order MUSCL schemes give similar results and, additionally, the 2nd-order MUSCL is more stable. Very similar results were obtained using the MUSCL scheme with two different limiters, with the DD limiter being numerically more robust across a range of Mach numbers.

The real gas run conducted with Mach number 8.5 shows similar behaviour: the fifth-order and second-order schemes behave in a similar fashion but show improvement over the first-order reconstruction. Due to the unavailability of exact free stream data, the heat flux values obtained cannot be directly compared to the experimental data observed. Despite of that, the overall agreement between the experimental data and the predicted values seems to indicate that the results obtained are reasonable.

CHAPTER 5

Assessment of CFD Method in Hypersonic Flows-II: Double-cone Configuration

Light thinks it travels faster than anything but it is wrong.
No matter how fast light travels,
it finds the darkness has always got there first,
and is waiting for it.

Terry Pratchett (English Writer,1948)

5.1 Introduction

NATO Research and Technology Organisation (RTO), working group 10[31,93,94], initiated a co-ordinated effort to increase the understanding of real gas phenomena which involved many different institutions and researches. A number of test cases were identified as potential candidates for code validation, where each case was specifically designed to draw out and examine phenomena that are dominant in hypersonic flows. An attempt has also been made to construct a database containing experimental measurements for well-defined model configurations, which is an invaluable resource in the validation phase of CFD simulations. Among these, the double-cone flare is an ideal test case for code validation due to the presence of quite complicated flow features, such as interaction between a shock wave and a separated region[48,93]. In this chapter, the double-cone flare (shown in Figure 5.1) is utilised to assess the effectiveness of higher order methods in the computational code CNS3D under the assumption of perfect and real gas [§].

The research facilities at Caltech, Calspan(CUBRC), and Princeton were used to perform a large portion of experimental studies with regards to this test case. The researchers, Holden and Wadhams, who conducted most of the experimental work on double-cone utilised sharp and blunt models with the first cone at a half angle of 25^0 and the second cone with a half angle of $55^0$and 60^0 respectively. The Reynolds numbers were chosen in such a way to ensure that flow over the double-cone remained laminar. To maintain high accuracy at high gradient regions of attachment and shock/shock interactions, the measurements were taken using miniature high-frequency, thin-film, and pressure instrumentation which ensure high spatial and temporal resolution. The high speed Schlieren photography employed with the aforementioned measurement techniques confirmed that large or small scale flow instabilities were not present over the double-cone configuration[79,81].

The flow generated over the blunt tipped configuration is similar to the sharp tipped version but with a larger separation zone. The computation of $25^0 - 60^0$ configuration was deemed more difficult due to a larger separation zone generated and the calculations indicated the presence of unsteady regions[24]. In this thesis all the numerical investigations employing the double-cone are performed using the sharp tipped $25^0 - 55^0$ configuration.

[§]The work presented in this chapter has resulted in a journal publication by Tissera *et al*[149].

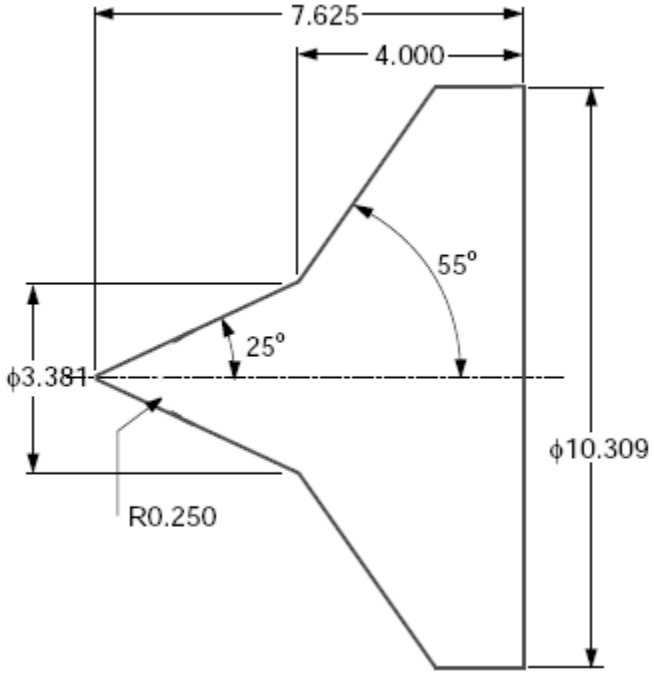

Figure 5.1 — *Double-cone geometry.*

Numerical investigations were carried out by Candler[25], Nompelis[119], Druguet[48], Gnoffo[57], and others under perfect and chemically reacting gas assumption using Navier Stokes governing equations. Inger and Moss[83] performed comparison studies between Direct Simulation Monte Carlo (DSMC) and Navier stokes approach. Druguet *et al*[48] used a second-order accurate modified Steger-Warming method to simulate the double-cone flow, under laminar flow conditions. A number of second-order reconstruction schemes were tested to determine what effect the choice of slope limiter had on the quality of the solution. A grid refinement study was also carried out to investigate grid convergence characteristics of each scheme used. It was concluded that the length of the separation zone is indicative of the amount of dissipation present within the scheme. Therefore, by comparing the separation length obtained through simulation to experimental data, it is possible to assess the accuracy of the numerical scheme. Additionally, the van Leer limiter was noted to be the best compromise between accuracy and robustness of all the limiters considered[48]. Furthermore, Mosedale[115] and Tissera *et al*[147] studied the effects of double-cone flow under perfect gas regime using higher-order methods. Some of the ideal gas results presented in thesis has been obtained jointly with Andrew Mosedale[115,147].

Although, the results gathered from high enthalpy test facilities are fairly important, it is quite a

laborious task to simulate hypersonic flight conditions completely. Due to the complexity of the problem, CFD methods have become an extremely effective alternative to experimental methods. Even though both techniques are far from perfect, both experimental and computational methods can lead to correlative validation. The development of various physical and numerical models, and the improvements in computational hardware have allowed the advancement of CFD as a powerful strategic tool. As a result, the design and development time of aerospace vehicles will reduce significantly.

There are many physical models that accommodate phenomena from a perfect gas model to a multi-species, high temperature, chemically reacting perfect gas model, including chemical and vibrational non-equilibrium relaxation. The properties of flow regime under rarefied conditions with such phenomena as radiation, ionization, and magneto-hydrodynamics have also been investigated[10,138]. In addition, the vibrational relaxation is also considered via the use of vibrational temperature. The vibrational temperature can be calculated using two-, three- or multi- temperature models[19,57,128]. The experimental work carried out by Holden and Wadhams[79,157], and the computational work performed by Candler and Nompelis[25,123] in parallel have shown that more work is needed to correctly establish the real gas effects over the double-cone.

The test runs designated 2893, 2894, 40[119], 42, and 43[79,157] have been employed for the purposes of validation. Among these, runs 2893,2894 are simulated under perfect gas assumption. The low enthalpy run `40`, has been carried out using the real gas assumption, yet fall short of sufficing the conditions necessary for full blown chemical dissociations or related phenomena as the energy within the free stream is not sufficient. This behaviour provides the opportunity to explicitly validate inviscid and viscous elements of the code without much interference from the effects of the source terms. Runs 42 and 43 have high enthalpy conditions (approximately 10MJ/Kg) and are simulated using the real gas assumption; chemical and vibrational phenomena are expected due to the large amount of energy present within the flow. Therefore, the effects of the source term become substantial[119]. The exact employed free stream conditions are presented later on.

The sections 5.2 and 5.3 present the numerical results obtained for the double-cone flow simulated under the ideal and chemically reacting gas assumption respectively; the pressure and heat transfer distributions from the numerical simulations are compared with the experimental data. To adhere to the main theme of this work, the results obtained utilising very high-order

mapped Weighted Essentially Non-Oscillatory (WENO-M) schemes are compared with typical higher order TVD reconstruction. Remarks on overall performance of the numerical methods are presented in section 5.4.

5.1.1 Grid Requirements

Careful attention must be given to the grid generation aspect of the problem. Gaitonde *et al.* [52] and Druguet *et al.*[47,48] have emphasised the importance of the quality and the resolution of the grid, that could yield converged solution. A smoother and resolved grid, especially at the tip and junction of the two cones, is necessary to adequately capture the boundary layer and the separation region. To sufficiently capture the boundary layer that initiates from the tip of the first cone, a well resolved grid is essential. Furthermore, the grid lines that fall over the cone junction, especially closer to the wall, must be smooth as possible to prevent any artificial perturbations[48]. The finer mesh generated with enlarge views of the tip and the cone junction is shown in Figure 5.2. Even though it is ideal that the mesh near the wall is orthogonal, grid resolution studies carried out by various researches suggest that the effect of this aspect is negligible[52].

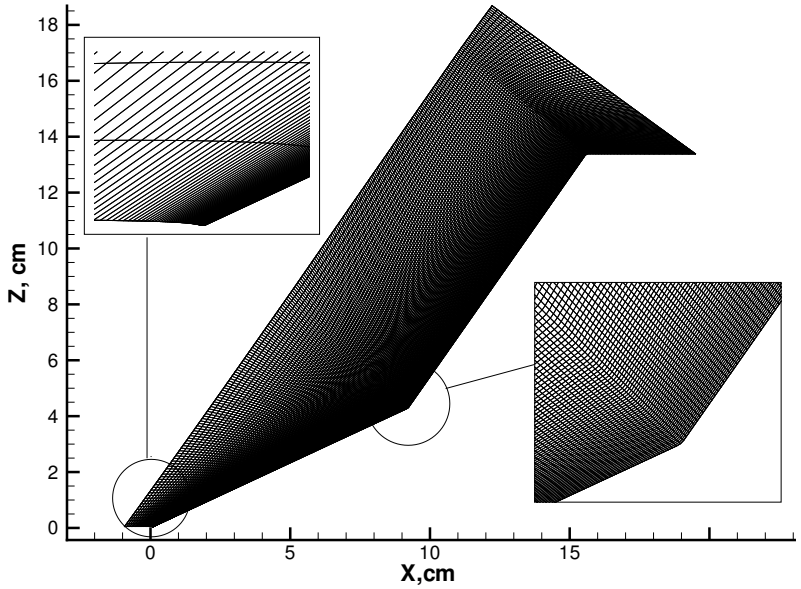

Figure 5.2 — *Computational mesh generated for the simulation of double-cone.*

The supersonic inflow, supersonic outflow, symmetry on the cone axis, and non-slip wall have

been used as boundary conditions. Note, that the supersonic inflow boundary should be sufficiently away from the cone surface to prevent any shock interaction with the boundary.

The size of the smallest grid cell near the wall is approximately 10^{-5}(*non-dimensional units*). Over the course of designing the grid, for both resolutions utilised, above design conditions were observed. Druguet*et al* suggests that, to successfully simulate the flow over the double-cone, it is imperative that implicit time marching scheme is employed; the reason being, when using the explicit time marching scheme, the CFL number used have to small to achieve any form of convergence. However, in this thesis, explicit time marching scheme has been applied, coupled with domain decomposition and the Message Passing Interface (MPI) parallelisation technique.

Comparatively, the explicit solvers are easily parallelised based on domain decomposition. Data exchange between the blocks and implementation of boundary conditions per each block is accomplished through a layer of ghost cells. The application of high order schemes leads to an increased depth of the halo required. The most accurate spatial discretisation implemented in CNS3D is the 9^{th}-order WENO method requiring five ghost cells on each side of the computational domain. The data exchanged between processors is stored into ghost cells.

For N^3 points per core, the total number of boundary cells which should be sent and received by each processor utilising a 9th-order scheme is $\sim 30N^2$. Therefore, it is necessary to consider the minimum number of points per core required in order to avoid the boundary exchange becoming the bottleneck. CNS3D exhibits a very good scalability providing efficiencies over 80% for up to 512 processors and approximately 70% for 1024 processors (based on 100% efficiency for 96 processors).

5.2 Ideal Gas Computations

The free stream conditions for the runs 2893 and 2894 for the double-cone were taken from the published work by Colbish *et al*[31] and are presented in Table 5.1. The Mach number used is approximately 12.7 in both cases. In the published literature[31], experimental values pressure coefficient (C_p) and heat transfer (St) are measured along the wall. By plotting either variable it is possible to identify the region of separation and re-attachment point where transmitted

shock impinges on the surfaces. The WENO scheme with 9^{th}- order reconstruction accuracy is compared with typical 2^{nd}- order TVD scheme with van Leer limiting.

Table 5.1 — *A matrix showing the two test runs simulated for the double-cone geometry under ideal gas conditions.*

Run	2893		2894	
M_∞	12.73		12.62	
Re_L	3.22×10^6		2.24×10^6	
P_∞ (Pa)	8.07		5.04	
ρ_∞ (kgm^{-3})	5.9×10^{-4}		3.9×10^{-4}	
T_∞ (K)	46.1		42.7	
Mesh	128x48	256x96	128x48	256x96

The flow structure typical of the double-cone geometry can be seen in the visualisation of velocity gradients in Figures 5.3 and 5.4, identifying not only the shock positions, but also some of the details of the separation region and under-expanded jet along the aft-cone. The flow has been simulated in first order reconstruction with stream lines indicating the path of the flow field. Using 9^{th}- order reconstruction, a massive separation bubble appears over the cone junction shown in Figure 5.4.

It was previously mentioned that this flow could be characterised by the size of the separation zone and the values at the peak[48]. When observing the results presented below (see Figure 5.5 - Figure 5.8) it is clear that the outcome is in favour of the higher-order methods. Run 2893 calculations performed with increasing order of accuracy over two grid resolutions are shown in Figures 5.5 to 5.6.

Concerning the experimental data, it would appear that in the lower Reynolds number case,2894 grid convergence has been obtained, and a clear discrepancy between experiment and simulation exists (Figure 5.8). The separation bubble has not been correctly captured even in the case of 9^{th} -order WENO (see Figures 5.8(e) & 5.8(f)); in contrast the results obtained for the case 2893, using identical grid resolutions have captured the separation bubble much more accurately. At this time, reason for this discrepancy is unknown. It can be speculated that the experimental free stream conditions listed may contain inaccuracies and need to be clarified. The preliminary runs on finer grids have indicated that this is indeed the converged solution to the problem set in the simulations.

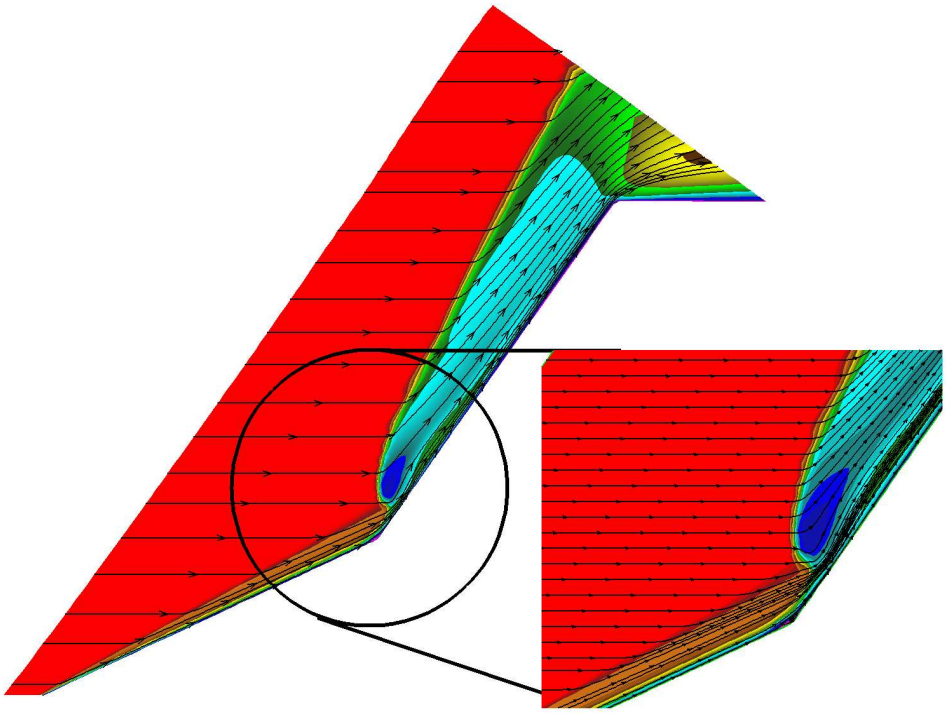

Figure 5.3 — *Streamline visualisation: 1^{st} order reconstruction scheme.*

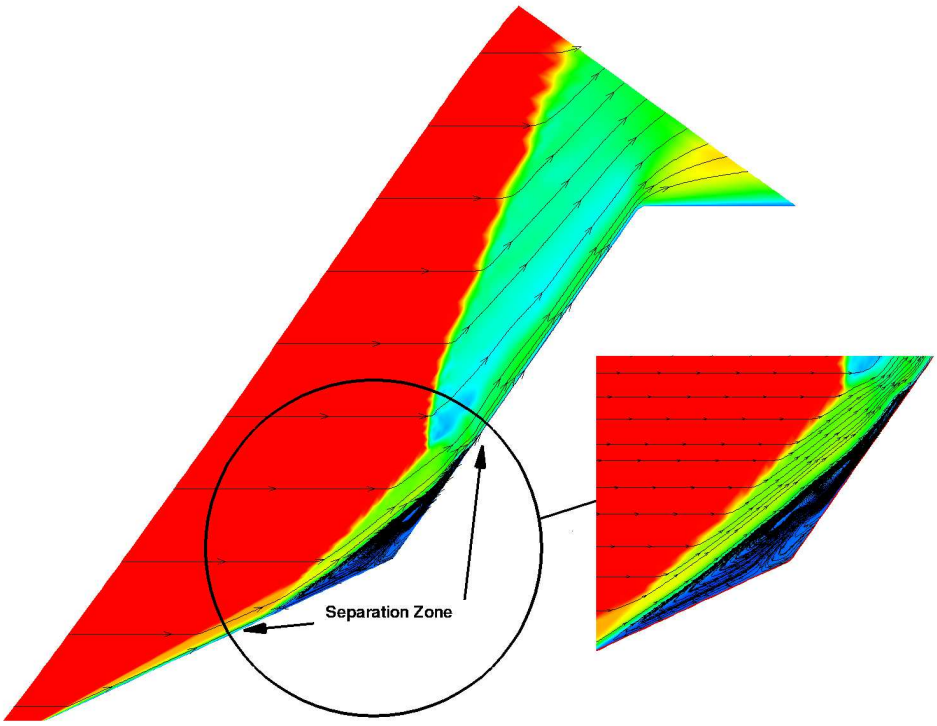

Figure 5.4 — *Massive separation bubble visible in run 2893: 9^{th} order WENO scheme.*

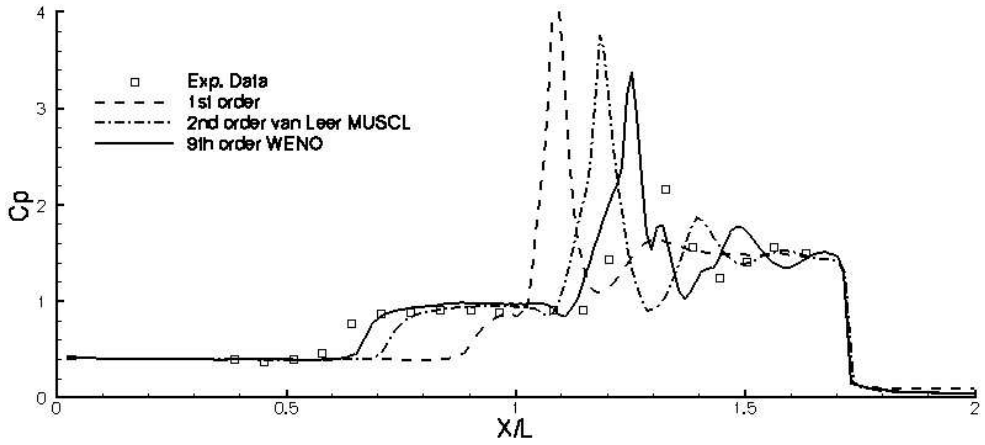

Figure 5.5 — *Run 2893: Pressure Coefficient plotted using 128x48 mesh showing different reconstruction methods.*

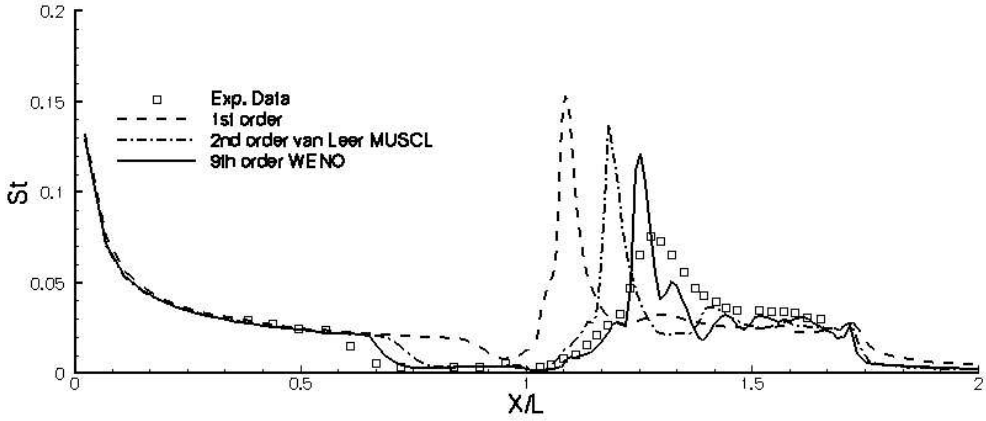

Figure 5.6 — *Run 2893: Stanton number plotted using 128x48 mesh showing different reconstruction methods.*

The C_p and St number results show that the experimental results are best duplicated when the order of accuracy of reconstruction is at maximum. This is much more clearly visible in Figure 5.9, which shows a difference between predicted separation zone lengths between 2^{nd} order and 9^{th} order. At the same time it can be observed that the gain resulting in increasing the grid resolution is comparatively minute. Therefore, it is evident that increasing the order of accuracy offers a much greater improvement than doubling the resolution. It is also undoubtedly much cheaper. although it is worth acknowledging that the measure of surface quantities, in particular the gradients for Stanton number, are dependent on the grid in a finite volume solver. A complete set of results obtained for both runs 2893 and 2894, utilising all reconstruction schemes and all grids is presented in Figure 5.7 and 5.8.

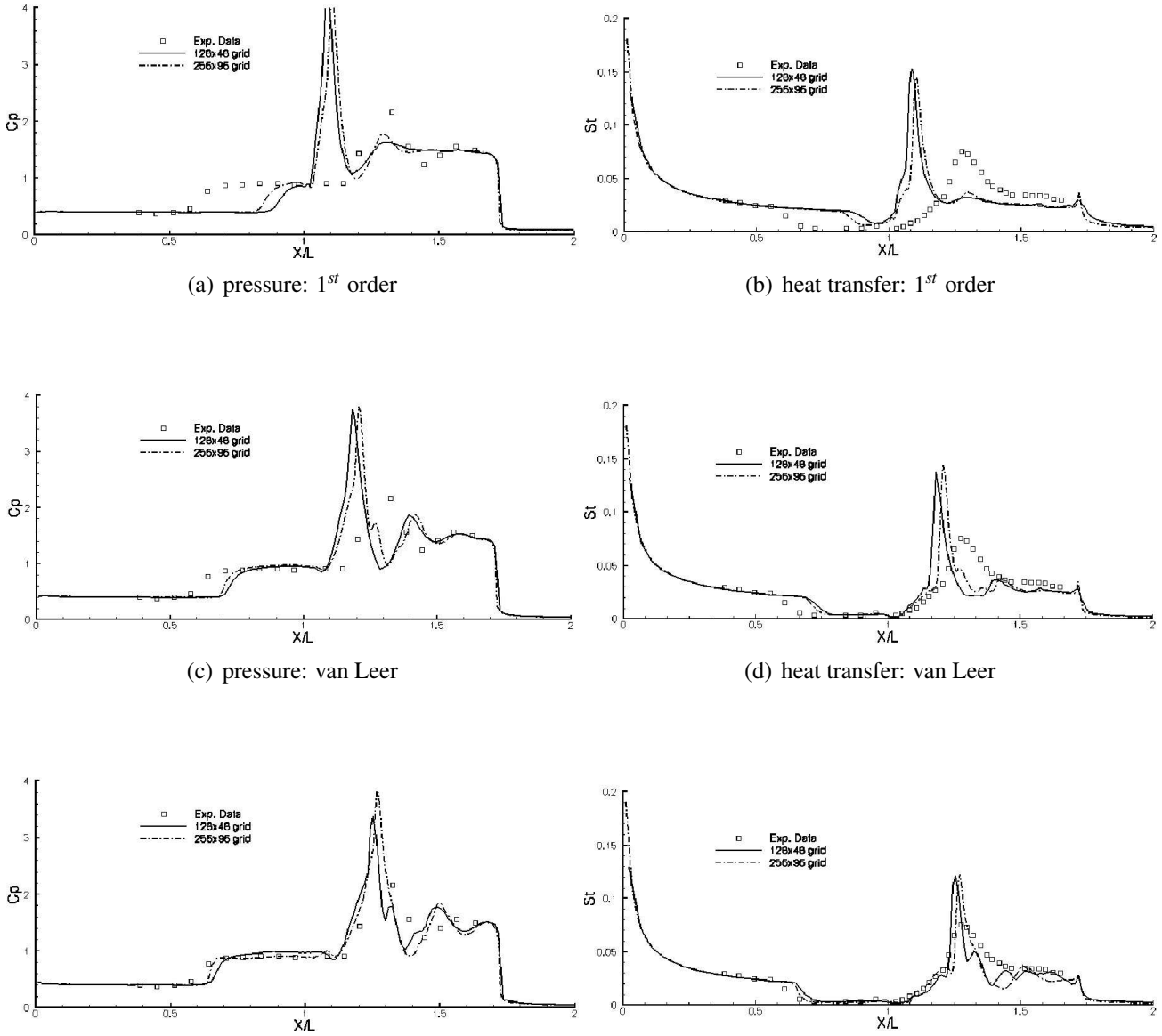

(a) pressure: 1^{st} order

(b) heat transfer: 1^{st} order

(c) pressure: van Leer

(d) heat transfer: van Leer

(e) pressure: WENO 9^{th}

(f) heat transfer: WENO 9^{th}

Figure 5.7 — *Comparison of pressure coefficient and Stanton number for run 2893 for grids 128x48 and 256x96.*

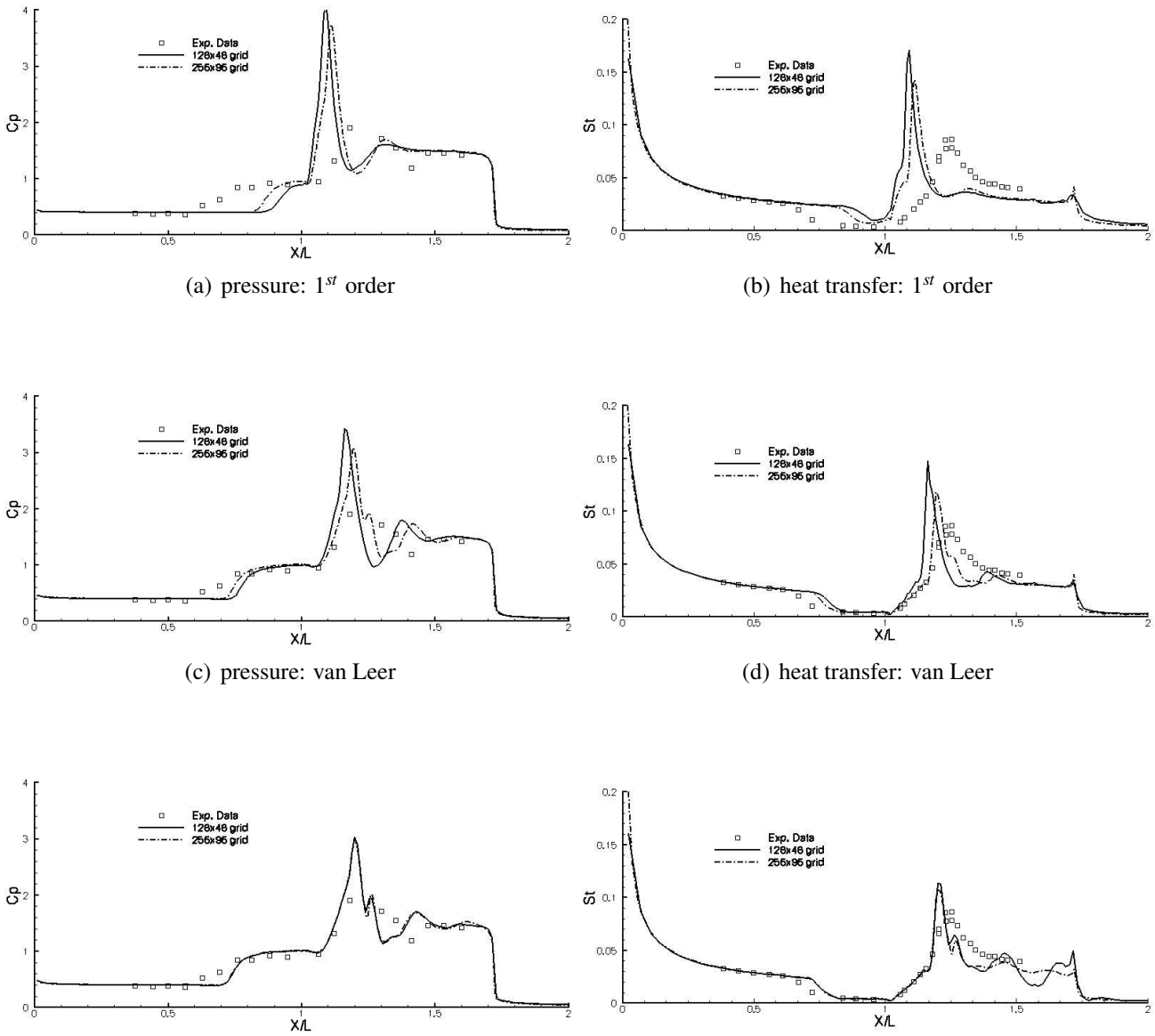

(a) pressure: 1^{st} order

(b) heat transfer: 1^{st} order

(c) pressure: van Leer

(d) heat transfer: van Leer

(e) pressure: WENO 9^{th}

(f) heat transfer: WENO 9^{th}

Figure 5.8 — *Comparison of pressure coefficient and Stanton number for run 2894 for grids 128x48 and 256x96.*

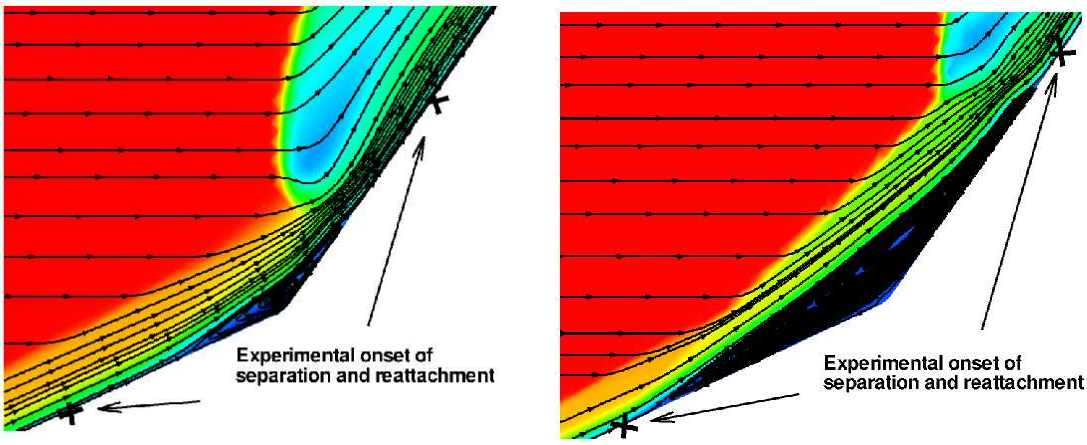

(a) 2^{nd} order van Leer MUSCL

(b) 9^{th} order WENO.

Figure 5.9 — *Comparison of separation zones with run 2894 on coarse grid (128x48) between different reconstruction methods- Axial -velocity plotted with instantaneous streamline.*

5.2.1 Comparison of CNS3D and Commercial software FLUENT

The double-cone runs 2893 and 2894 performed using FLUENT, 1^{st}- order spacial reconstruction, are also presented (see Figures 5.10(a) ∼5.10(d)). FLUENT failed to converge at second order, and while it may be possible to manipulate the available parameters to remedy this, at the present moment FLUENT fails to produce usable results for the double-cone flow.

The first-order results obtained exhibit a remarkable similarity between the two codes, though neither could be said to be a good match to the experimental data. It was observed earlier and elsewhere that increasing the order of accuracy above first order offers a much greater improvement than doubling the resolution of the grid, and is undoubtedly cheaper. With CNS3D, this improvement extends above second-order methods.

It seems that one or more of the assumptions made in modelling this flow are insufficient. The matter has been raised in various works within the literature, and it is difficult to hypothesise as to which assumptions are relevant - be it chemical equilibria or slip effects, unsteady flow or varying wall temperature and heating effects. Some of these would prove easier to assess than others, and there is also a potentially significant related issue of grid design. However, the high-order methods present a useful basis for further investigation.

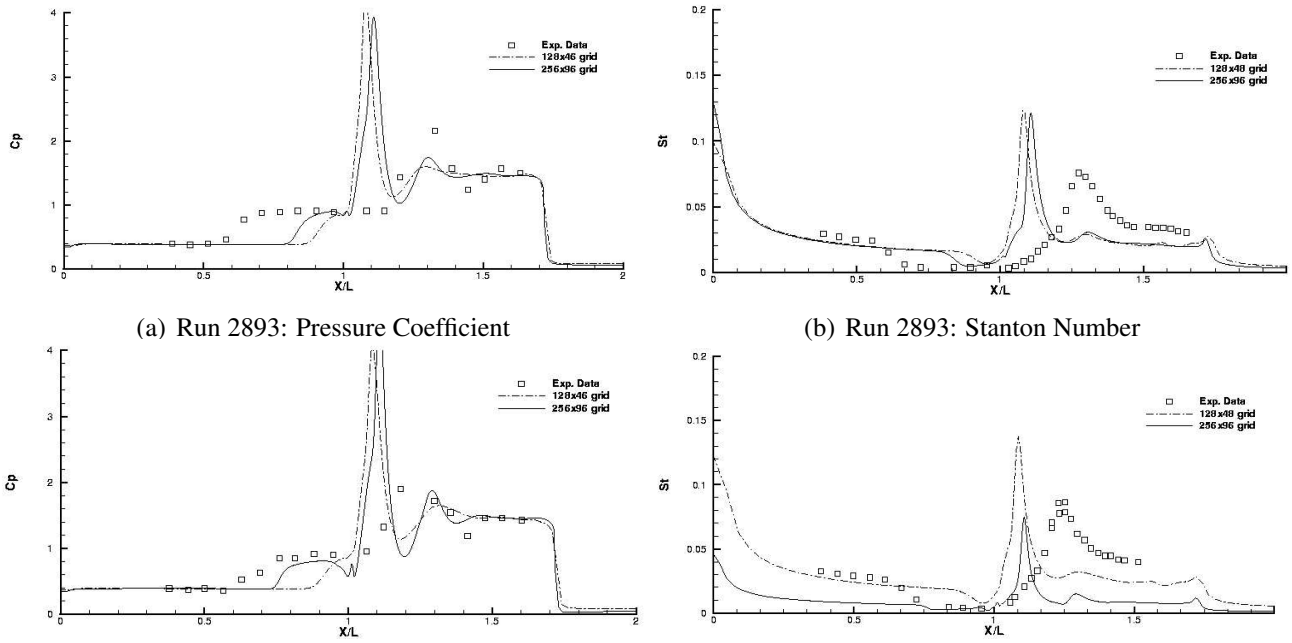

(a) Run 2893: Pressure Coefficient

(b) Run 2893: Stanton Number

(c) Run 2894: Pressure Coefficient

(d) Run 2894: Stanton Number

Figure 5.10 — *Pressure coefficient and Stanton number for first-order FLUENT runs.*

In the next section it has been attempted to address some of the concerns as the investigation deviates from perfect gas assumption to real or chemically reacting gas assumption. Flow physics become more complicated and Navier stokes equations are supplemented by further terms and governing equations. For further details of governing equations used see chapter 2.

5.3 Real Gas Computations

In this section, the validation of the computational code CNS3D continues; runs designated 40, 42, and 43 have been simulated. This is to ascertain the performance of CNS3D (focusing mainly on reconstruction methods), in simulating complex chemically reacting flows. The enthalpy condition of run `40` is about 5MJ/kg, where runs 42 and 43 is at a total enthalpy of 10MJ/kg. It is assumed that no chemical reacting effects are present within the flow for the low enthalpy simulation.

For real gas computations, it was not possible to obtain results using WENO scheme with 9^{th}-order reconstruction accuracy; severe oscillations materialised due to the presence of strong shocks and it was observed to be extremely unstable. However, it was possible to simulate

chemically reacting flows using WENO scheme with 5^{th}- order reconstruction accuracy. The heat transfer and pressure results calculated utilising WENO scheme have been compared with 2^{nd}- order TVD scheme with van Leer limiting.

The free stream conditions for the aforementioned runs are listed in Table 5.2. Furthermore, the results presented in this chapter for runs 40, 42, and 43 have been published in Knight *et al* [94](AVT 136 Subtopic No. 2 for RTO). The motivation behind the publication was to compare the capabilities of modern CFD codes (such as the LAURA code used by NASA[26,27]) and to assess the CFD for specific physical problems (shock interactions[79] and control surfaces in non-equilibrium laminar flows[109]). Several participants presented the computed results for Runs 40, 42, and 43, utilising a thermo-chemical model (as appropriate), numerical algorithms, and grid refinement strategy of their own choosing. The results were also presented in the publication by Tissera *et al*[147,149].

Table 5.2 — *Free stream conditions for the double-cone runs.*

Case	Run 40	Run 42	Run 43
M_∞	11.56	11.52	8.87
$Re_m(10^3/m)$	656.16	333.4	306.6
T_∞(K)	172.22	268.7	576.0
T_v (K)	2735	3160.0	576.0
T_w (K)	295.5	273	273.0
ρ_∞ (gm^{-3})	2.52	1.468	2.134
C_{N_2}	1.00	1.000	0.73704
C_{O_2}	-	-	0.17160
C_N	-	-	0.000
C_O	-	-	0.02659
C_{NO}	-	-	0.06477

Run 40

The separation zone formed over the region between first and second cones (see Figure 5.11) is the primary area of interest as the activity over the separation zone is tightly coupled with global flow characteristics. The low enthalpy simulation shows no significant chemically reacting effects as expected and produces a large separation bubble. The agreement between the experiment and the predicted surface pressure using the 2^{nd}-order scheme over the finer mesh

is good. In comparison, 5^{th}-order WENO scheme displays instabilities over the same region. These instabilities are visible even over the coarse grid. The heat transfer rate onto the surface, predicted by both schemes, is good.

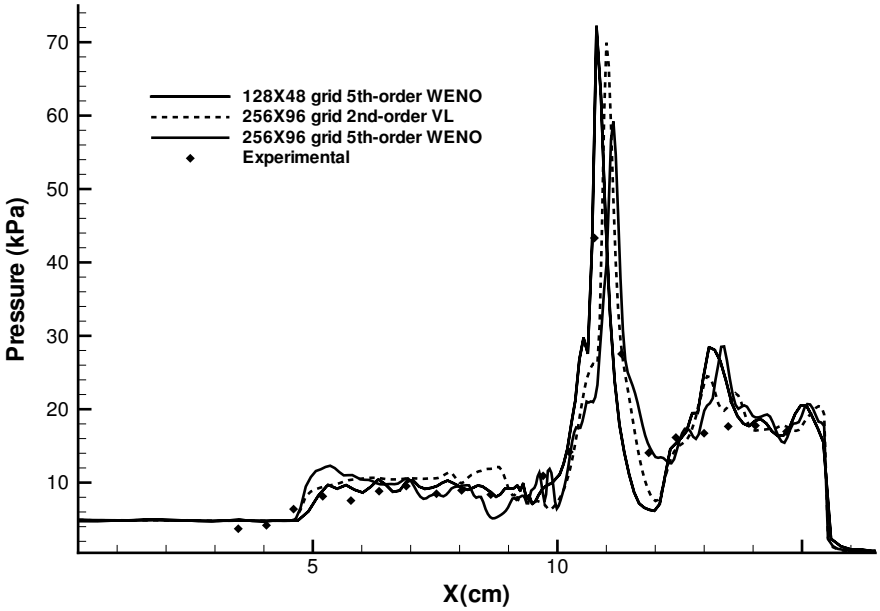

(a) Run 40: Pressure Coefficient

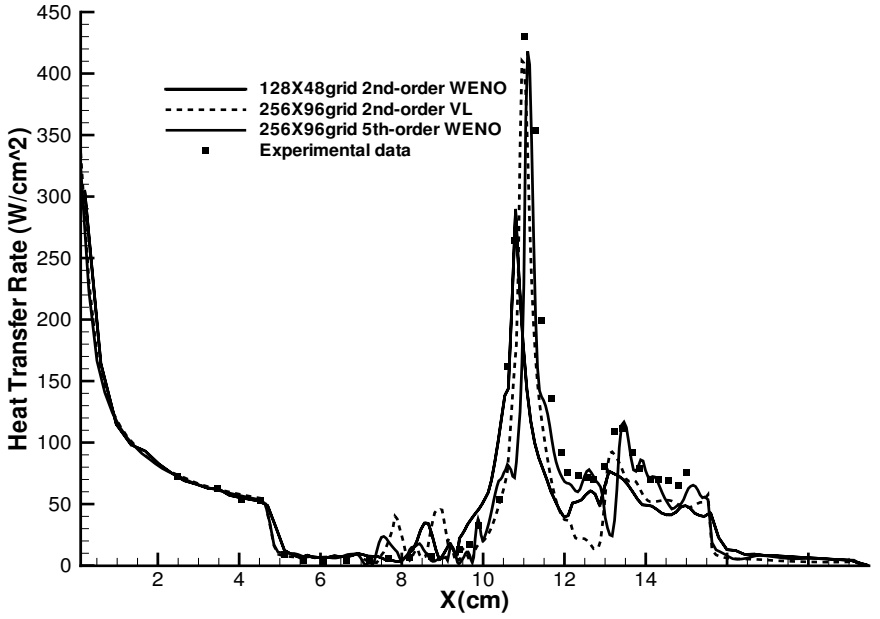

(b) Run 40: Stanton Number

Figure 5.11 — *Run 40: Comparison of Pressure coefficient and Stanton number plotted for both reconstruction schemes and grids.*

It is also evident that the position of the peak heat transfer rate, which is directly coupled with the activity over the separation region, is also dependent on the reconstruction order of accuracy. The peak heat transfer rate predicted via WENO is positioned further away from the tip of the double-cone compared to VL. The 5^{th}-order scheme under-predicts the peak heat transfer over the coarse mesh by 29%, but recovers with the increment of the grid resolution.

The cause for the instabilities present over the separation bubble can be speculated as being linked to the numerical aspect such spatial reconstruction or the Riemann solver. However, there is reason to believe that the root of the instabilities may lie elsewhere. The Run 40 has been simulated by different researchers such as Nompelis (2009)[120] using various computational codes and techniques; the instabilities witnessed in this instance has been observed in most other cases. Rather curiously these instabilities are not observed in the experiment. The researchers Holden and Wadhams[80] at CUBRC has performed the Run 40 experiment number of times taking into account the feedback from the CFD attempts. However, the cause these instabilities and the discrepancy between the experiment and the computational results are not understood and still under investigation.

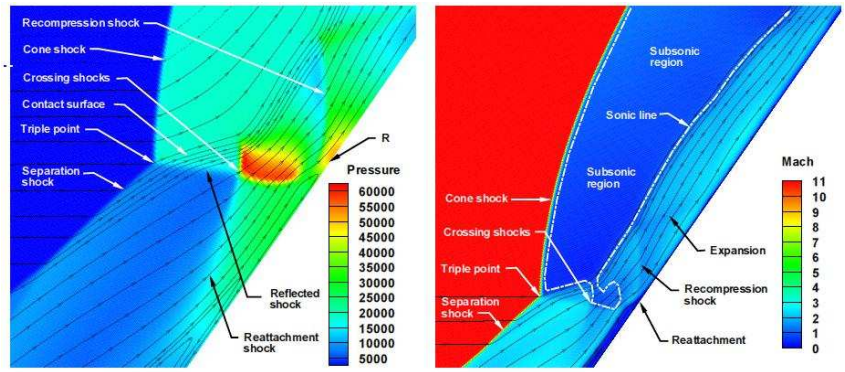

Figure 5.12 — *The structure of the flow field for run 42.*[after 94]

Run 42

The separations region formed over the cone junction for the run 42 is presented in Figure 5.13. The various regions and phenomena defined in Figure 5.12 can be clearly identified in Figures 5.14 - 5.17, where contours of Mach number, pressure, and two temperatures are presented. The shock-shock interaction in the near vicinity of the cone junction gives rise to an adverse rise in temperature (see Figure 5.16). This corresponds to the peak heat transfer to the wall observed in Figure 5.18.

The overall agreement between surface pressure prediction by both schemes and the experiment, over the fine mesh is satisfactory (see Figure 5.19). The surface pressure and the length of the separation zone are captured exactly by the WENO scheme, where 2^{nd}-order TVD reconstruction displays a slight shortfall. Over the coarse mesh WENO duplicates the length of the separation almost exactly, but shows slight oscillations over the separation region (see Figure 5.18). Surprisingly, these oscillations subside with the increment of the grid resolution. The pressure over the separation zone, obtained via the 2^{nd}-order scheme for coarse grid, is over predicted by 5%; and the WENO under-predicts by 7%. As the order is increased, the position of the heat transfer peak moves towards the position of the peak observed by the experiment. Both schemes fail to capture the precise thickness of the heat transfer peak, but WENO succeeds in predicting the location accurately.

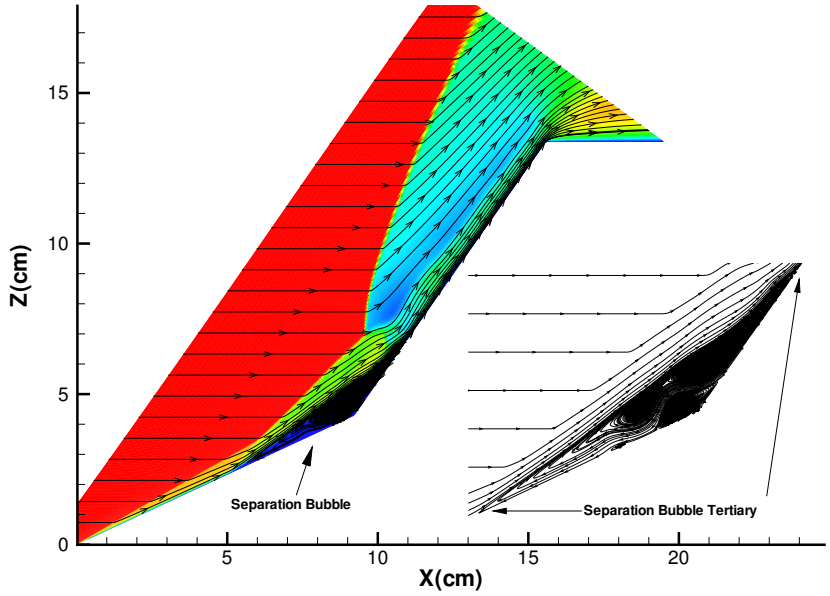

Figure 5.13 — *Run42: Velocity stream lines and close-up of separation bubble produced.*

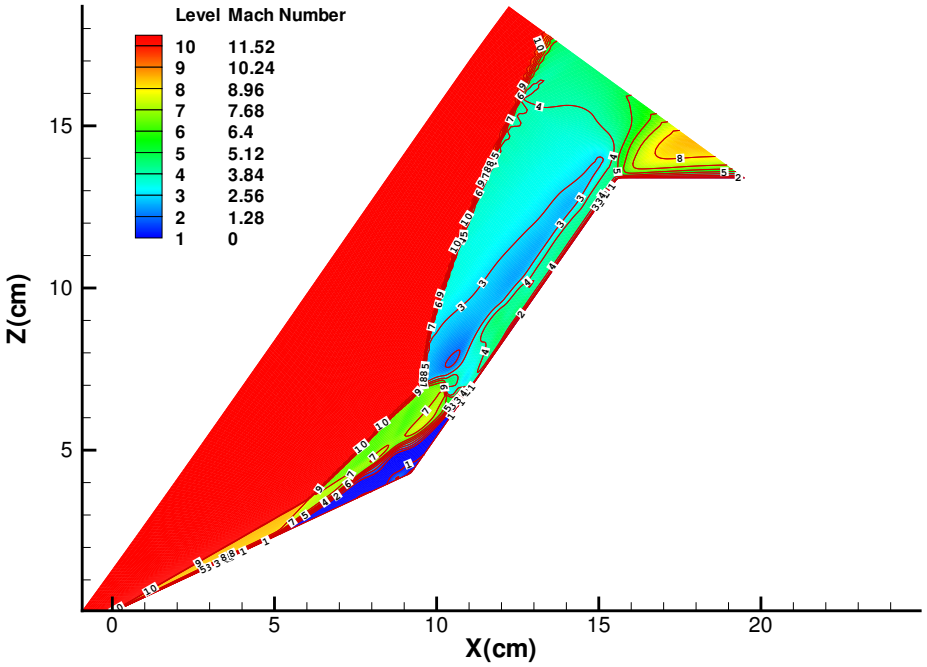

Figure 5.14 — *Run42: Mach number contours.*

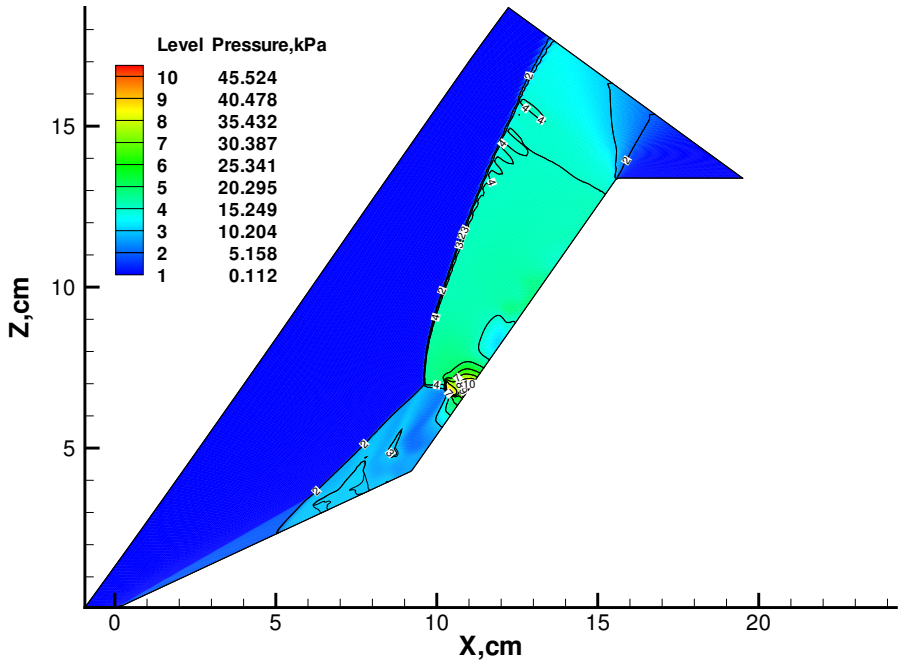

Figure 5.15 — Run42: Pressure contours.

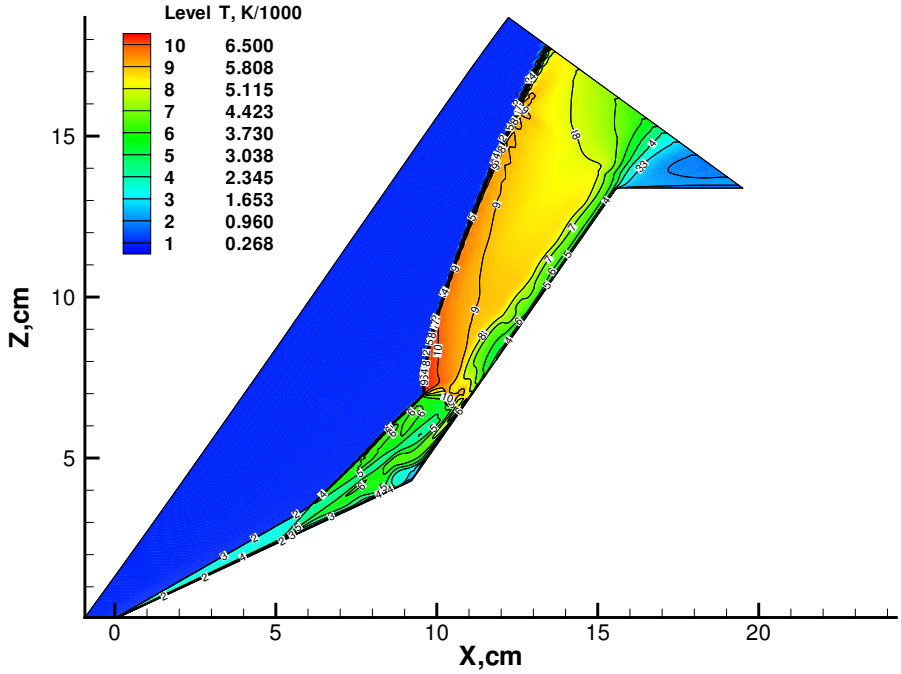

Figure 5.16 — *Run42: Translational-rotational temperature contours.*

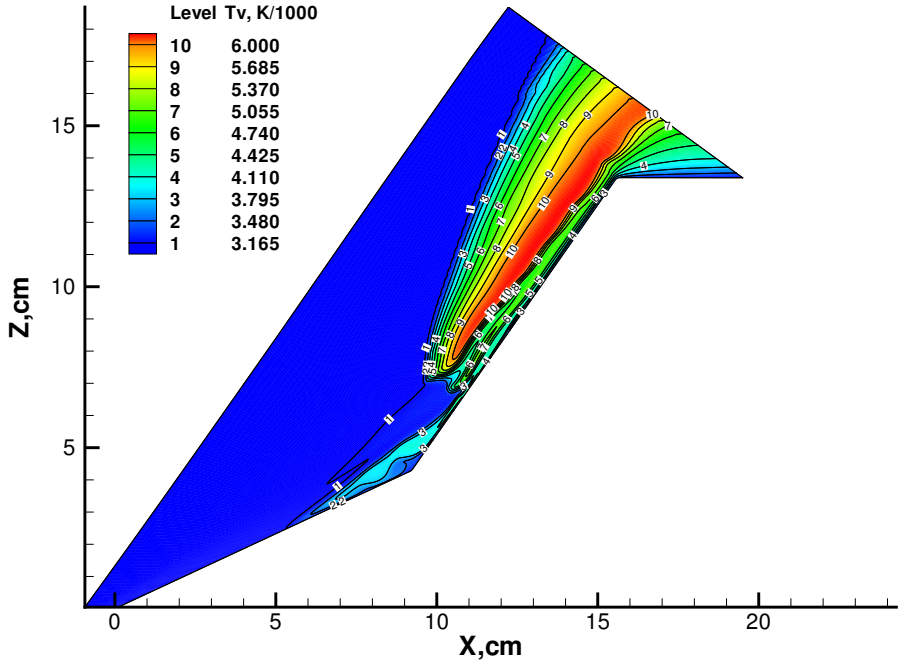

Figure 5.17 — *Run42: Vibrational temperature contours.*

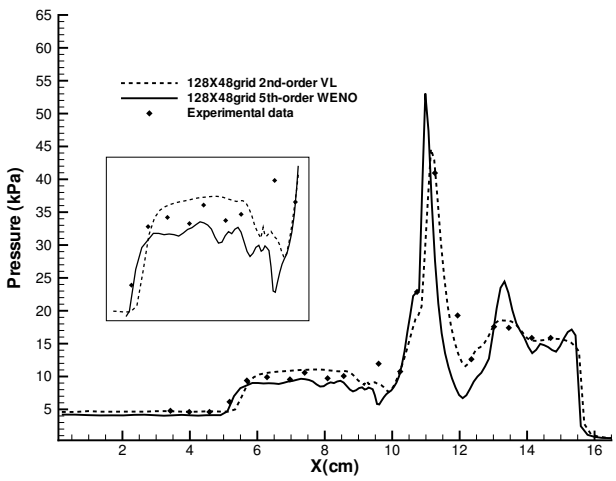

(a) Run 42: Pressure

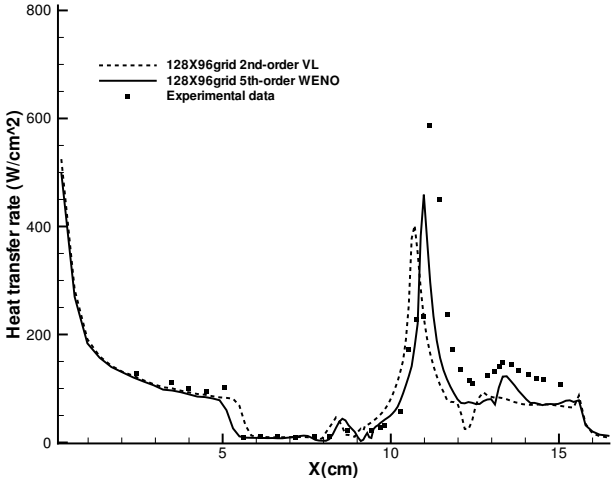

(b) Run 42: Heat transfer rate

Figure 5.18 — *Comparison of pressure coefficient and Stanton number plotted for both reconstruction schemes using 128 $\times$ 48 grid. Peak experimental values; pressure:41kPa, heat transfer: 580W/cm^2*

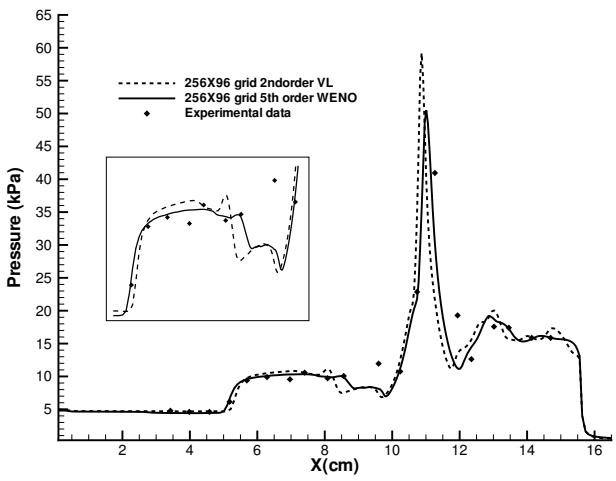

(a) Run 42: Pressure

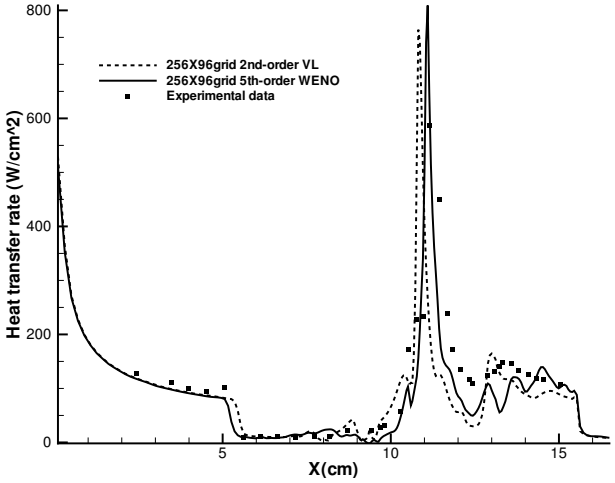

(b) Run 42: Heat transfer rate

Figure 5.19 — *Comparison of pressure coefficient and Stanton number plotted for both reconstruction schemes using 256 $\times$ 98 grid. Peak experimental values; pressure:41kPa, heat transfer: 580W/cm^2*

The variation of peak values observed for both grid densities reaffirm the observation made earlier that the heat transfer to the wall is directly influenced by the quality and resolution of the grid. However, the separation bubble predicted by both reconstruction schemes for pressure and heat transfer provides sufficient evidence that the physical models implemented pertaining to the non-equilibrium behaviour over the double-cone is adequate. Yet, reason for the overshoot

of the peak heat transfer value observed in Figure 5.19(b) has to be further investigated [†].

Run 43

Contours of Mach number, pressure, and two temperatures are presented in Figures 5.20 to 5.23. Furthermore, the pressure and heat transfer rate to the surface are shown in Figures 5.24 & 5.25 respectively. Only the finer mesh has been used to simulate the conditions of this run. The 2^{nd}-order scheme under predicts the length of separation zone and over predicts the surface pressure over the same region by 5%. In comparison, WENO scheme predicts the length of recirculation region fairly accurately, but over-predicts the surface pressure by 3%.

The overall prediction of heat transfer by both schemes is not satisfactory. The heat transfer over the first cone is under-predicted by 4% and over-estimated by about 8% over the separation region by both schemes. The peak value is also under-predicted by a massive 30% - 35% by both schemes. The position of peak heat transfer, calculated by both schemes lies almost on top of each other, and upstream of the position observed by the experiment. This is surprising as, compared to previous runs, the difference among predicted separation zone lengths between WENO and VL schemes is much greater in run 43.

[†] a comparison of the results obtained via various computational codes including CNS3D for the Run 42 is available in Knight (2010)[94].

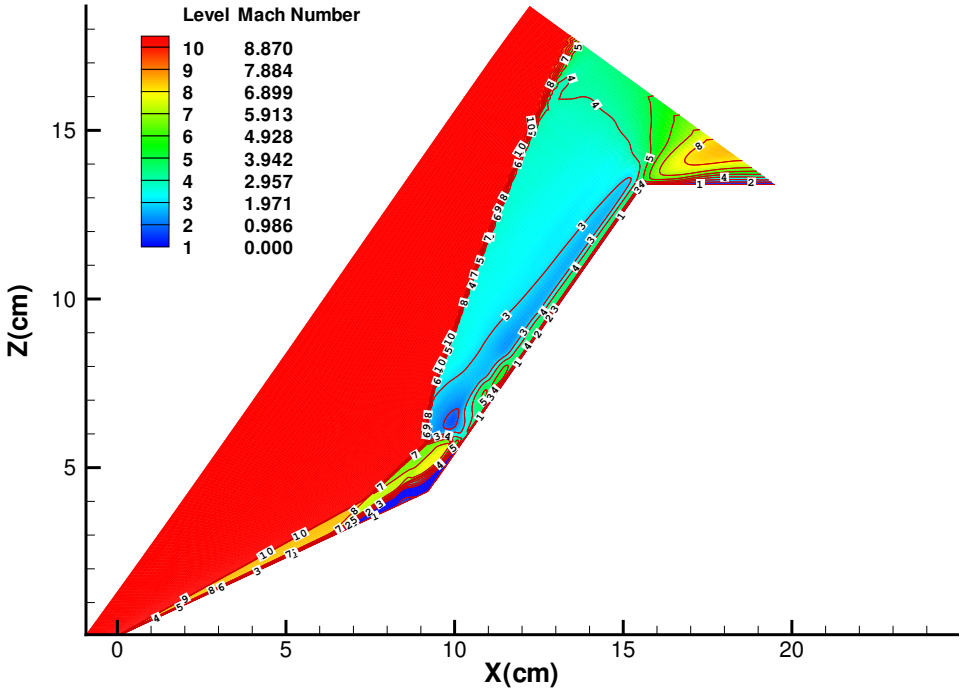

Figure 5.20 — *Run43: Mach number distribution.*

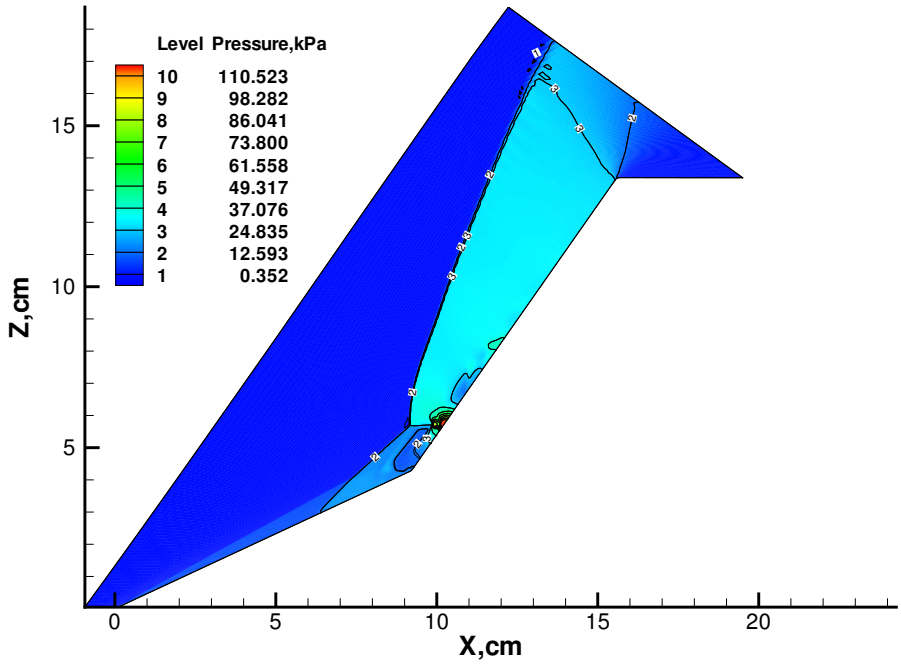

Figure 5.21 — *Run43: Pressure contours.*

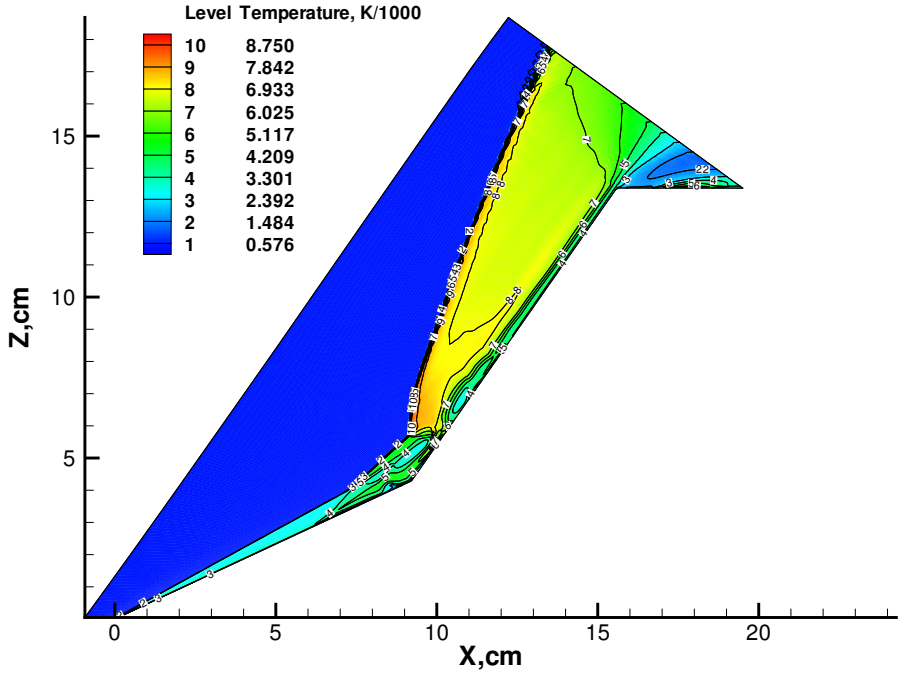

Figure 5.22 — *Run43: Translational-rotational temperature contours.*

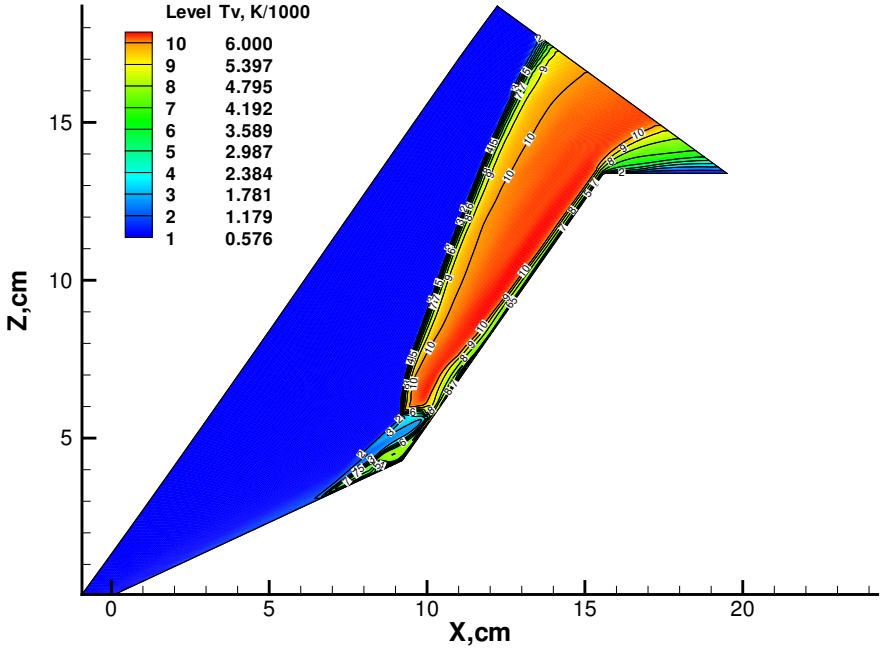

Figure 5.23 — *Run43: Vibrational temperature contours.*

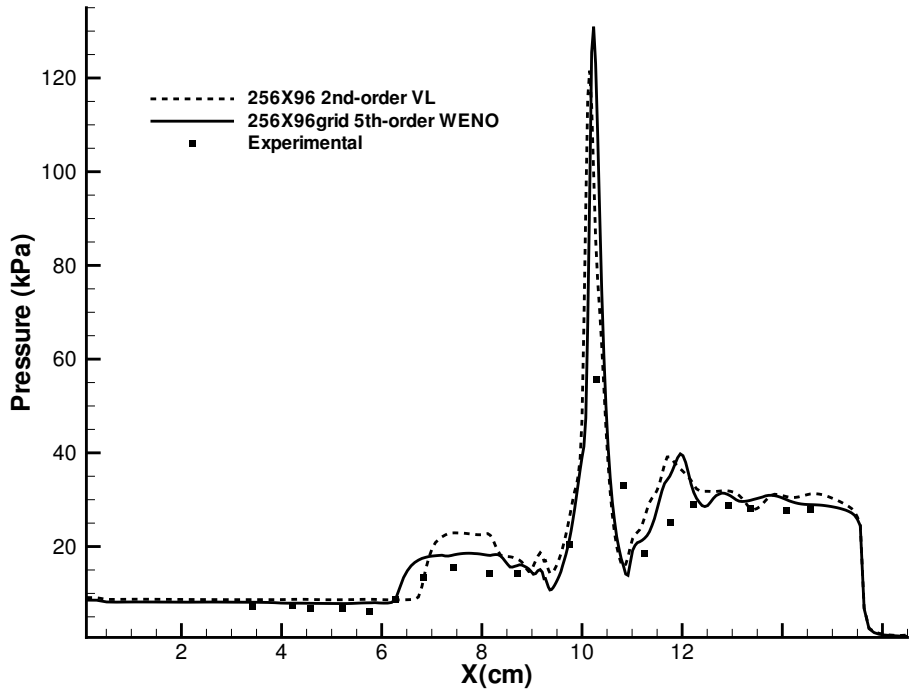

Figure 5.24 — *Comparison of Pressure coefficient plotted for both reconstruction schemes and grids.*

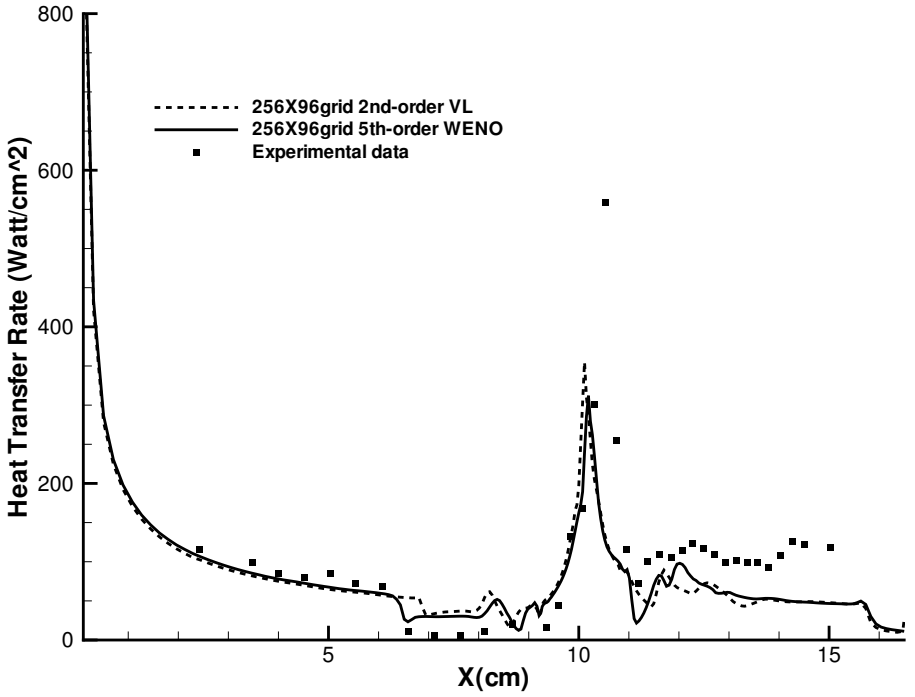

Figure 5.25 — *Comparison of Stanton number plotted for both reconstruction schemes and grids.*

The obtained results for both reconstruction schemes show that further improvement is nec-

essary in the case simulating air dissociation and non-equilibrium effects. When considering the peak pressure and heat transfer values, the mathematical models that describe the physics seem not be inadequate; further investigation is necessary to rectify this issue. The separation region predicted by the 5^{th} -order WENO scheme and the experiment is a closely matched; thus, justifies the use of very higher order methods in terms of yielding improved results over typical 2^{nd}- order reconstruction.

To complement these results contours of mass fractions of species are also presented in Figure 5.26; the dissociation of molecules, N_2 and O_2, and the formation of atomic N, and O is visible. In addition, the formation of NO molecules and the recombination of atoms are also evident.

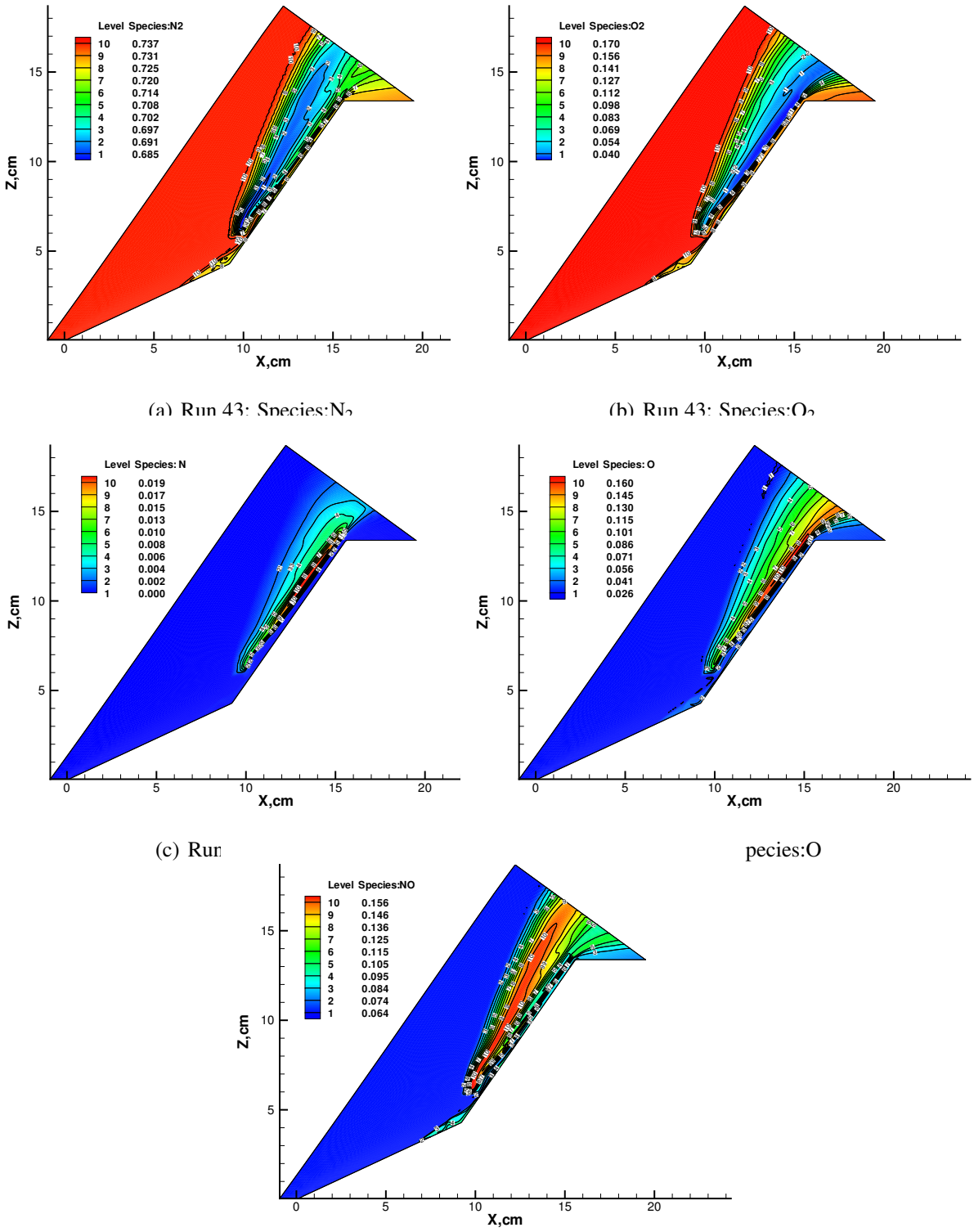

(a) Run 43: Species:N_2

(b) Run 43: Species:O_2

(c) Run

pecies:O

(e) Run 43: Species:NO

Figure 5.26 — *Run 43:Mass fraction of species evolution for all species.*

Experimental Uncertainty

The peak values of pressure have been over predicted for both Runs 40, 42, and 43. However, direct comparison of experimental data with the computational values, specially over the regions of rapid change must be interpreted with caution.

Two possible reasons could be identified as the cause of this discrepancy, between the computational values and the experimental data[94]. Firstly, the location of the experimental transducer that recorded the peak experimental pressure, does not always corresponds to the true location of experimental peak pressure. Therefore, the computationally predicted peak pressure value, which is greater than the experimentally measured peak pressure, may very well not be inaccurate. Furthermore, the transducer employed has a finite size and integrates the pressure over a small surface area. Therefore, the lateral scale of the transducer may be equivalent to several times the grid spacing along the surface depending on the grid resolution employed; it is necessary then to filter out the computed pressure distribution. As a result, direct comparison between the computed and experimental peak pressures with a strict view point is unreasonable, specially over the regions of rapid change.

5.4 Summary

Numerical simulations were carried out to ascertain the effect of increasing the order of accuracy in the reconstruction phase of the numerical scheme in real gas conditions. The double-cone flare which gives rise to complex flow features was used as the test case for validation. An established second order scheme VL and 5^{th}-order scheme WENO were used for the purpose of comparison.

A close attention was given to the region of separation as it is an excellent indicator of the effectiveness and dissipative nature of the numerical scheme. The obtained results by both schemes for the low enthalpy and high enthalpy flow with Nitrogen gas agree fairly well with the experimental data. As expected, the less dissipative nature of WENO forces the length of the separation region to be greater than the length predicted by the VL scheme.

Overall, the WENO scheme simulates the length of the separation zone accurately enough.

Even though this is a positive trend to justify the use of higher order schemes on very high enthalpy chemically reacting scheme, further investigation is needed to verify this finding. As established in the past and in this instance, the double cone test case is extremely useful for code validation purposes but fairly difficult to simulate. The approach of increasing the order of accuracy shows clear improvement in the results over the 2^{nd}-order scheme. In addition, the performance of the higher order scheme in lower resolutions is similar in nature.

CHAPTER 6

Assessment of CFD Method in Hypersonic Flows-III: Ablation Effects

Without pain, without sacrifice, we would have nothing.
Like the first monkey shot into space.

Chuck Palahniuk; author of 'Fight club' (American Novelist,1962)

6.1 Introduction

During hypersonic re-entry, the outer surface of aerospace vehicles undergoes extreme conditions mostly due to the intense heat generated, typically behind the shock wave. It is imperative that the excess heat is kept at bay, to protect vital equipment and possibly human lives. The heat shield, commonly referred to as Thermal Protection System (TPS), is designed to protect the structural components of the space vehicle from these extreme conditions. The surface structure consists of materials capable of withstanding high temperatures and an insulation layer to hinder the conduction of heat to the structure. Depending on the region, the magnitude of heat experienced by the vehicle varies and the Thermal Protection Material (TPM) used in the design must accommodate this fact[2,30,138]. Areas, such as the nose tip and the leading edge of the wings could be seen as the regions with the highest heat loads. It is thus essential to predict the thermal response of TPS material in order to achieve a more successful design for space-entry vehicles[13,131]. Failure of heat shield or error in heat transfer predictions will undoubtedly lead to the most disastrous outcome.

In this chapter, the effects of surface ablation on the flow field around HB-2 flare and the double-cone flare geometry, are investigated. All test cases were investigated under perfect and real gas assumption in previous chapters 4, and 5, with non-ablating boundary conditions. Furthermore, the double-cone flare was investigated under ablating conditions by Tissera *et al* [148]. However, to the best of this author's knowledge, no computational study that investigates the HB-2 flare under ablating wall boundary conditions exists.

The double-cone geometry gives rise to complex flow features, including strong viscous-inviscid and shock-shock interactions, leading to boundary layer separation. Druguet *et al.*[48] observed that making alterations to parameters, such as the forward chemical reaction rate or angle of attack, would alter the size of the recirculation zone. HB-2 flare does not give rise to overly complicated flow features, similar to double-cone, yet can be employed as a useful test case for code validation[§].

The current investigation employs the compressible Navier-Stokes solver (CNS3D) developed over a number of years by Drikakis[6,162]. The pressure and heat transfer distributions for each case with and without ablation are compared, with first and second order reconstruction. Very

[§]The work presented in this chapter has resulted in a publication by Tissera *et al*[148].

high-order WENO or MUSCL schemes have not been used in this study as they were found to be too unstable near the immediate vicinity of the wall. Further investigation is needed to rectify this issue, which is beyond the scope of this thesis. The next and following sections present the mechanics of the gas-surface interaction and the ablation flow model respectively. The pressure and heat flux to the wall obtained for each test case are presented in sections 6.3 through 6.4.

6.2 Catalytic and Ablation Effects: How They Differ

When a flow around the aerospace object is at non-equilibrium, the dissociated particles come into contact with the surface; the interaction between the gas and the solid surface is referred to as *heterogeneous* reaction. Typically, two types of wall interaction can be observed; the first type is known as catalytic wall interactions where, the solid surface only aids the chemical reaction (usually recombination in nature); the other is known as ablation, where the gas actively reacts with the wall to create new molecules. These phenomena were briefly introduced in chapter 1.

Catalytic Wall Effects

Here, the phenomena of the catalytic wall effects are discussed; however, the catalytic wall model has not been employed by any simulation presented in this thesis. The reason for the inclusion of this section was to give the reader an initial understanding about this phenomena and a comparative notion with ablating wall effects presented later on.

As it was established, the dissociated atoms interact with the surface when an external body is introduced into the flow. The dissociation processes typically absorb heat to reach the activation energy required to initiate the forward reaction or dissociation [138]. In the immediate vicinity of the surface (vehicle surface is colder than adjacent flow), recombination reaction or backward reaction is initiated resulting in a release of heat. The composition of the gas is altered near the immediate vicinity of the wall.

In order for the recombination reactions to occur, the surface material acts as a catalyst and increases the rate of reaction, without being consumed in the process. A catalyst lowers the

activation energy necessary to start the reaction. Therefore, reactions reach equilibrium faster, yet the equilibrium state and composition of gas remain unchanged. Reaction heat released is considerably high, when compared to reactions initiated with a non-catalytic wall. Thus, a poor catalytic material should be chosen in order to reduce the reaction heat at the surface as much as possible.

If the surface is to be a catalyst, initiating reaction, the surface and the atoms involved should be compatible. Then, by a process of diffusion, adsorption into the surface would occur. This is called surface selectivity. For example, a metal surface would be more likely to absorb oxygen than a metal oxide surface. Two mechanisms to model this process are known as Langmuir-Hinshelwood (L-H) and Eley-Rideal (E-R).

In the Langmuir-Hinshelwood (L-H) mechanism, two separate atoms are that are adsorbed in different sites of the surface react, by collision, on the surface. They then desorb from the wall, again as one molecule, releasing excess energy from the recombination reaction. The thermal load on the wall is increased.

The L-H model can be written as:

$$* + A \rightarrow A*; \;\; * + B \rightarrow B*$$

$$A* + B* \rightarrow AB* + *; \;\; AB* \rightarrow AB + *$$

In the Eley-Rideal (E-R) mechanism, an atom becomes attached to a wall site. Another atom from the gas collides with this attached atom, forming a molecule. These bound atoms act as a body; it is in an excited state and quickly leaves the surface. However, the excess energy of the molecule is eventually transmitted to the wall through quenching in the wall region[32].

While the E-R model can be written as:

$$* + B \rightarrow B*; \;\; A + B* \rightarrow AB*$$

$$AB* \rightarrow AB + *$$

Here, $*$ represents an active site, while A and B represent individual atoms. It could be observed that $*$ does not affect the gas/solid interaction process. With the use of a suitable model, the

inner workings of the above combination mechanism can be analysed and quantified[117].

In each mechanism, no atoms are lost from the surface sites. This is shown in the equation forms of the mechanisms, where atoms from the sites remain separated from the molecules at the end of the process. This is the differing factor between a catalyst where ablation does not occur[2,9].

In reality, when considering the shuttle wall condition, the recombination process is driven by the E-R mechanism at lower temperatures. The L-H mechanism becomes more important as temperature increases, allowing $A*$ and $B*$ to move around more freely and collide with each other. However, more data is needed in order to accurately model the region of transition between the two mechanisms[117,138].

When the catalytic efficiency, γ, is at a value that implies all atoms striking the surface undergo recombination, the wall is considered fully catalytic[58]. The rate of chemical reaction is increased infinitely at a fully catalytic wall (the mass fractions at the wall reach local equilibrium values at local pressure and temperature). On the other hand, if none of the atoms striking the surface recombine, the catalytic efficiency is taken to be zero and the wall is considered as non-catalytic. In this case, the catalytic rate is zero. However, neither of these two extreme conditions of catalytic efficiency are observed commonly in nature. At a partially catalytic wall, the chemical reactions taking place are catalysed at a finite rate. As mentioned earlier, the diffusion feeds particles from the gas into the wall surface. When steady-state boundary conditions are considered, it is found that the flux generated due to chemical reactions at the wall/gas interaction surface must be balanced by the species diffusion flux at the wall. The catalytic efficiency in this case is finite; this is the most commonly encountered occurrence[2,58,76].

Ablation Wall Effects

In comparison, during ablation unstable atoms present within the flow field interact with the surface to form new molecules; therefore, mass loss and shape change take place over the TPS of the hypersonic vehicle.

The physical process of ablation is complex and not fully understood. However, it is vitally important to predict the thermal response of TPS material in order to achieve a more successful design for space-entry vehicles. In recent years, only a small amount of experimental work has

been carried out into ablation related topics. The reason for this is quite simple. The difficulties inherited in the experimental method with regards to hypersonic flows were highlighted in previous chapters. Similar issues crop up in ablation related experiments; with additional difficulties in recreating phenomena such as mass loss during re-entry conditions at ground level, the computational approach has become the preferred avenue of investigation. The experiments conducted focused on aspects pertaining to the development of TPS such as ascertain the magnitude of mass loss, material response, and thermo-physical properties[77,98,102,104,110,134,153,156]. In addition to TPS used in Aerospace vehicles during re-entry, several experiments focused on other extreme heating environment, such as solid rocket motor nozzle[68,92,111], and vertical launch systems (military applications)[99].

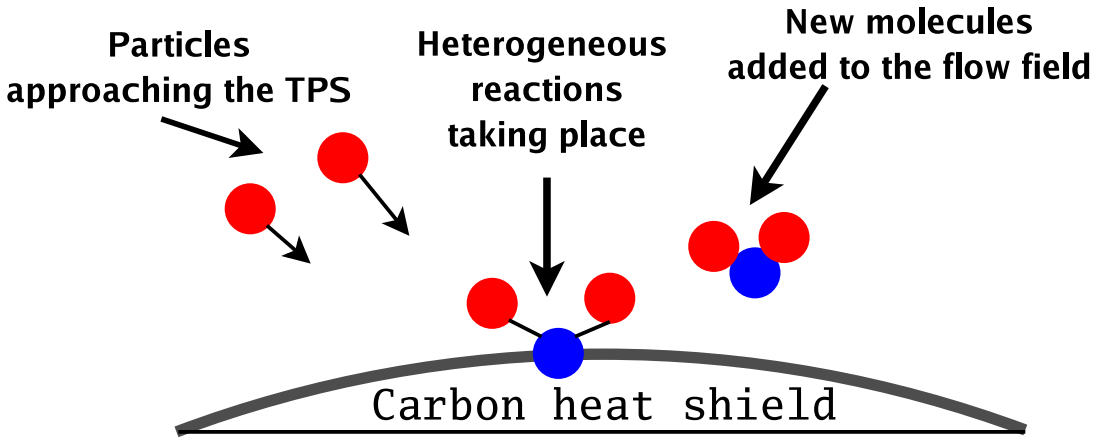

Figure 6.1 — *Removal of material occurs due to the species in air reacting with TPM.*

More recently CFD has also been employed as a tool to model ablation and related phenomena. As mentioned in Chapter 1, CFD techniques provide an outlook into the TPS response by predicting heat flux to the wall and subsequent shape change. However, as it has been the case throughout this thesis and hypersonic flow modelling as a whole, the validity of the results obtained are usually marred with uncertainties.

The majority of the attempts that employed CFD techniques to study ablation have used only simple boundary conditions at the ablating wall[113]. This makes the obtained results unreliable and unable to realistically predict the thermal response. It is crucial that mass and energy balance at the ablating wall must be taken into account with as many components as possible.

However, in reality most studies tend to focus on some aspects while imposing simplified assumptions on others. Due to the tight coupling between the processes, these studies carry the

possibility of producing results that do not represent the ground realities. A detailed study expanding on a number of numerical models regarding TPS has been carried out by Koo *et al.* The review covers many areas of aerospace sciences, where extreme heat conditions prevail and the application of TPS is a must; these include spacecraft and missiles, ablative materials for a missile launching system, solid rocket motor internal insulation, and solid rocket motor nozzle assembly etc[98].

One of the methods that has been used by many researchers utilises B' tables or thermo-chemical tables. These tables are compiled via a solution of equations that describe the thermodynamic state between the TPS and the adjacent gas; the surface energy and mass balance equations are also coupled into the solution process. Further details of the thermo-chemical ablation model are available in[90]. This model has been successfully applied to many charring and non-charring ablating material problems[113].

In this thesis, instead of employing the B' tables, the ablation is imposed as a boundary condition on the surface. The ablation model (surface reaction model) is coupled with the non-equilibrium real gas flow where an iterative procedure is then used to resolve the equations at the interface between the flow and the surface and, directly, calculate the key parameters, such as mass and heat fluxes[28,160,161]. In the next section further details of this method are provided.

6.3 Interaction Between Surface and the Flow Field

When the TPM interacts with chemical species such as atomic oxygen, several physical processes, namely adsorption of the species, migration of the two species involved, recombination and desorption, may take place. When considering non-charring ablators, the most typical TPS materials consist of Carbon and the interaction with atomic species gives rise to ablation. The carbon atoms can combine with a number of different atoms; if species O, N, and H are considered, the reactions that can take place are,

$$2O + C_s \rightleftharpoons O_2 + C_s, \tag{6.3.1}$$

$$O_2 + 2C_s \rightleftharpoons 2CO, \tag{6.3.2}$$

$$O + C_s \rightleftharpoons CO, \tag{6.3.3}$$

$$N + C_s \rightleftharpoons CN, \tag{6.3.4}$$

$$H + C_s \rightleftharpoons CH, \tag{6.3.5}$$

$$H + 2C_s \rightleftharpoons C_2H. \tag{6.3.6}$$

The sublimation can also take place when carbon evaporates into C, C_2, C_3, C_4, and C_5, where the most dominant reaction is defined as

$$3C_s \rightleftharpoons C_3. \tag{6.3.7}$$

However, experiments carried out by Liu[106], have revealed that the recombination reaction given by the Equation 6.3.1 is not dominant and almost no O_2 is produced, under re-entry conditions. The remaining Equations 6.3.2 to 6.3.6 show that the surface of the aerospace vehicle becomes a part of the chemical reaction and ablates into the flow field. To minimise complications, in this study the Park's Model has been employed and only reactions 6.3.2, 6.3.3, and 6.3.4 are considered. Even then, as the CNS3D code considers *56 reactions for 9 chemical species* (that is, Equations 2.5.5 $\sim$ 2.5.21 and Equations 6.4.1 $\sim$ 6.4.3), the calculations become even more computationally expensive.

6.4 Near-Surface Thermochemical Models

In this section, the relevant thermo-chemical models and equations needed to adequately describe ablation phenomena are discussed. Interaction between the gas and the solid surface could occur in the form of Oxidation, Nitridation or as surface catalytic effects.

Mass Blowing Rate

The mass blowing rate of carbon can be calculated as follows;

$$\dot{m}_1 = \rho C_o \bar{v}_o \beta_o \frac{M_c}{M_o}; \left(O + C_{(s)} \rightarrow CO\right), \tag{6.4.1}$$

$$\dot{m}_2 = \rho C_{o_2} \bar{\nu}_{o_2} \beta_{o_2} \frac{M_c}{M_{o_2}}; \left(O_2 + 2C_{(s)} \rightarrow 2CO\right), \tag{6.4.2}$$

$$\dot{m}_3 = \rho C_N \bar{\nu}_N \beta_N \frac{M_c}{M_N}; \left(N + C_{(s)} \rightarrow CN\right), \tag{6.4.3}$$

$$\dot{m}_{tot} = \dot{m}_1 + \dot{m}_2 + \dot{m}_3 \tag{6.4.4}$$

The term $\bar{\nu}_i$ is defined as $\bar{\nu}_i = \sqrt{\frac{kT_w}{2\pi m_i}}$. The efficiency of each reaction is denoted by β. The subscripts w and s represent gas and solid properties at the wall respectively[5].

$$(\rho v_w) = \sum_i \dot{m}_i = \dot{m}_{tot} \tag{6.4.5}$$

Surface Mass Balance

For a given surface temperature, T_w, the molar and mass fractions of each species `s` on the surface are found from the surface mass balance equation, which when projected onto the normal to the surface, read as follows:

$$-\rho D_s \frac{\partial y_s}{\partial n} - \dot{m}_{tot} C_s = -\hat{N}_s \tag{6.4.6}$$

The first two terms on the left hand side of the above equation are the mass transfer via diffusion and convection normal to the surface, respectively. The source term $\hat{N}_s$ represents mass blowing for individual species. Here, an assumption is made that no material is being removed in a condense phase (solid and liquid).

Depending on the inclusion of species when calculating the mass blowing rate in the Equation

6.4.4, the source term $\hat{N}_s$ is calculated as

$$\begin{aligned} \hat{N}_{CO} &= \dot{m}_1 \frac{M_{CO}}{M_C} + \dot{m}_2 \frac{M_{CO}}{M_C}, \quad \hat{N}_{CN} = \dot{m}_3 \frac{M_{CN}}{M_C}, \\ \hat{N}_N &= -\dot{m}_3 \frac{M_N}{M_C}, \quad \hat{N}_O = -\dot{m}_1 \frac{M_O}{M_C}, \quad \hat{N}_O = -\dot{m}_2 \frac{M_{O_2}}{2M_C}, \end{aligned} \tag{6.4.7}$$

If s is equal to CO_2, N_2, NO and C, then $\hat{N}_s$ is zero as these species are not produced or consumed during the surface chemical reactions.

Note that

$$\sum_s \hat{N}_s \equiv \dot{m}_{tot}$$

Surface Energy Balance

The wall temperature of the aerospace vehicle is calculated via the use of energy balance equation:

$$q_{conv} = \overbrace{\sigma \varepsilon T_w^4}^{radiation} + \overbrace{\dot{m}_{tot} h_w}^{ablation}, \tag{6.4.8}$$

where q_{conv} is the total convective heat flux on the surface given by

$$q_{conv} = \overbrace{-k\frac{\partial T}{\partial n} - k_v \frac{\partial T_v}{\partial n}}^{thermal-conduction} - \overbrace{\rho \sum_s h_s D_s \frac{\partial y_s}{\partial n}}^{diffusive\ chemical\ energy}$$

The first term on the right hand side accounts for surface radiation according to the Stefan-Boltzmann law, in which σ is the Stefan-Boltzmann constant and ε is emissivity. For carbon, $\varepsilon \approx 0.85$. The second term is energy supplied to the gas by ablation; h_w is the enthalpy of carbon at the surface temperature. The nine mass balance equations are solved together with the energy balance equation in order to calculate the mass fractions on the surface, as well as the surface temperature.

6.5 Calculation Procedure

The CFD runs were carried out to establish a relatively optimal size of the computational domain and spatial resolution. The computational mesh should be clustered near the ablating surface and around the nose of the body; coarser cells should be allowed downstream of the nose towards the tail of the body.

In order to calculate mass fraction, wall temperature, and mass blowing velocity the mass and energy balance boundary conditions are solved within flow calculation in a subroutine that is used specifically for this purpose. By solving the Equation 6.4.6 explicitly, it is possible to obtain mole fraction at the wall from which mass fraction can be obtained (The calculation process is presented in Figure 6.2).

Using the mass fractions calculated, the mass blowing rate, $\dot{m}$, can be determined for time level $n+1$ using the Equation 6.4.4. It is also possible to use the same procedure to calculate the temperature of the wall, by using the Equation 6.4.8. A detailed version of the calculation procedure is presented in Appendix B.

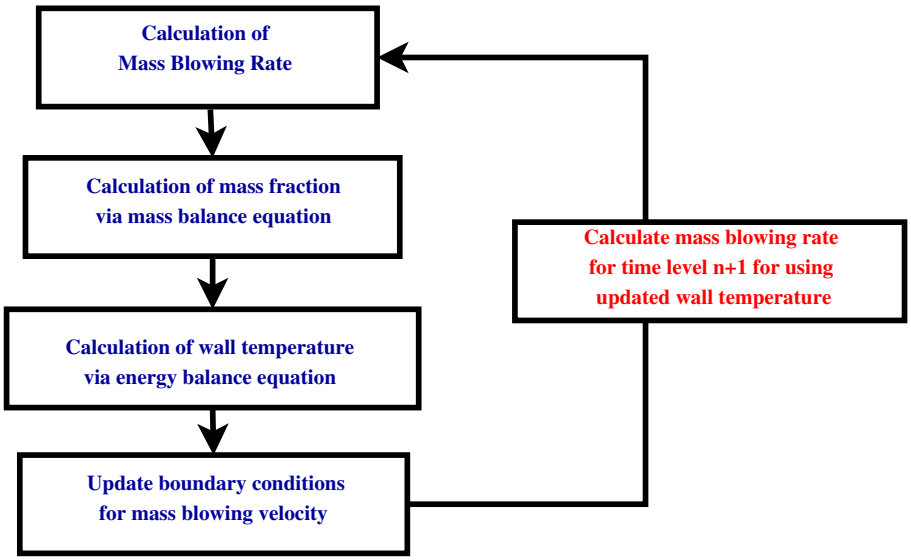

Figure 6.2 — *Calculation process to determine the wall temperature and mass fraction of species at the wall.*

6.6 Ablation Effects on HB-2 Flare

The HB-2 flare has been used for the validation of the ablation model implemented in the numerical code CNS3D. The free stream conditions, and test case used are identical to that of Case 005 presented in Chapter 4. For convenience, the free stream conditions are listed in table 6.1. All runs for this particular test case with ablating conditions were performed utilising a 128×48 grid in conjunction with 1^{st} and 2^{nd}-order numerical reconstruction scheme; the heat transfer, with and without ablation, is compared. Additionally, the mass fraction of species, two temperatures, and the mass blowing rate over the HB-2 surface are also plotted.

Table 6.1 — *Flow conditions for the HB-2 hypersonic configuration.*

Case	005
M_∞	8.5
Re_m	0.4×10^6
T_∞(K)	610
T_v (K)	610
T_w (K)	283
ρ_∞ (Kgm^{-3})	2.764×10^{-3}
C_{N_2}	0.72
C_{O_2}	0.28
C_N	1×10^{-8}
C_O	1×10^{-8}
C_{NO}	1×10^{-8}
C_C	1×10^{-8}
C_{CO}	1×10^{-8}
C_{CO_2}	1×10^{-8}
C_{CN}	1×10^{-8}

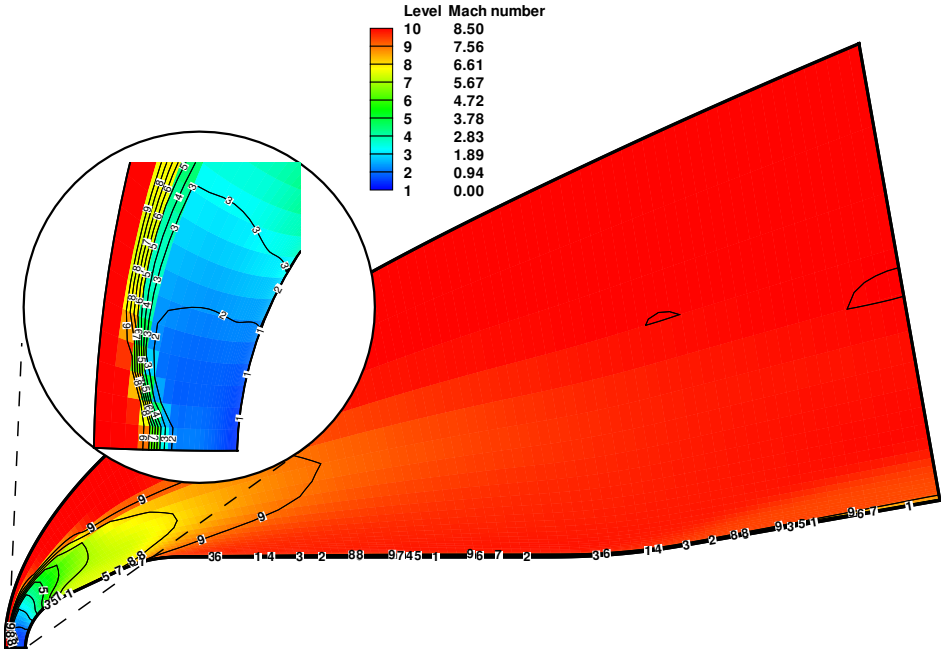

Figure 6.3 — *Contours of Mach number with ablating wall conditions.*

.

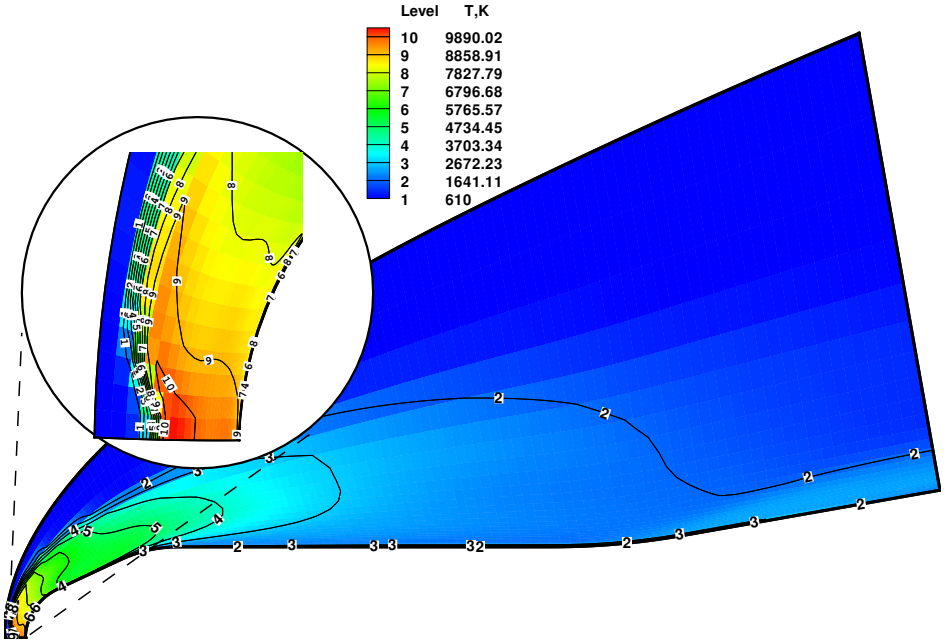

Figure 6.4 — *Contours of temperature with ablating wall conditions.*

The Mach number and temperature contours are presented in Figure 6.3 and 6.4 respectively and feature the flow phenomena within the ablating flow field. The shock layer developed over the test case is much thicker compared to non-ablating flow. This is expected during ablation. The reason for this behaviour is due to the wall boundary conditions imposed. In a typical situation, no slip wall boundary condition is assumed for the NS equations where velocities $u = v = w = 0$ at the wall. In contrast, during ablation the velocity component perpendicular to the surface, in this case w, is no longer zero; the mass ejection at a velocity of w is the cause of the thicker shock layer.

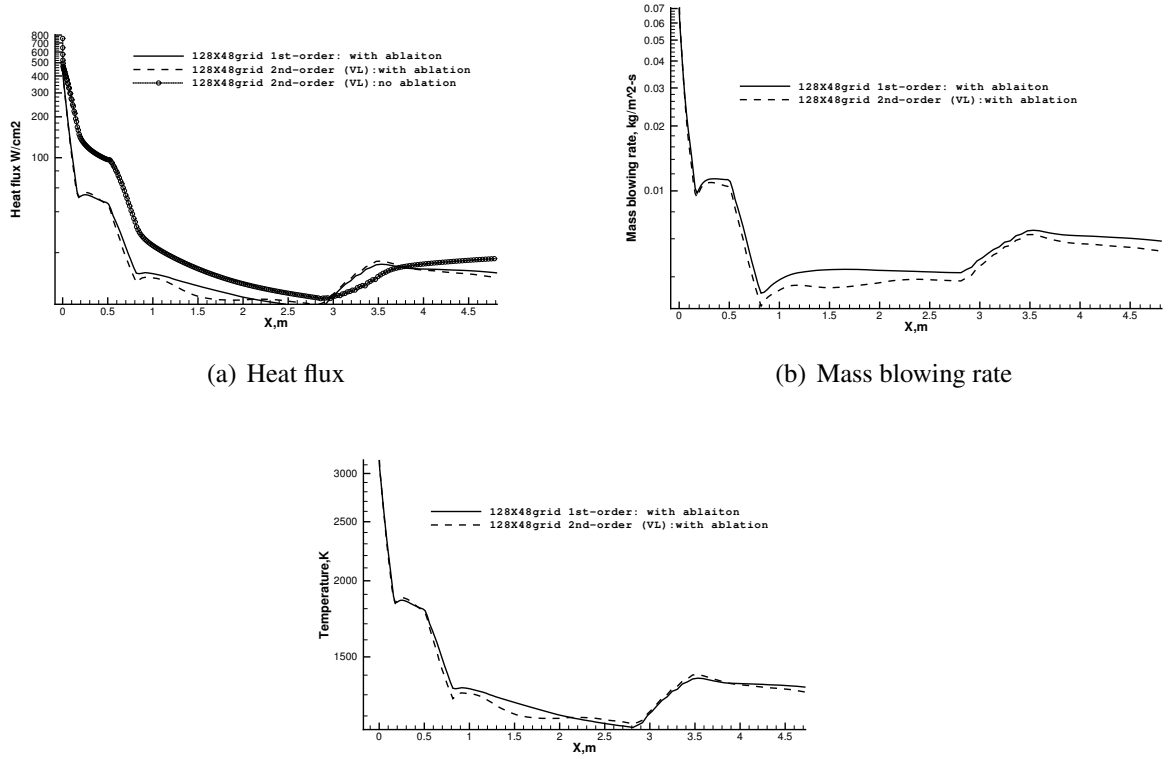

(a) Heat flux

(b) Mass blowing rate

(c) Translational temperature

Figure 6.5 — *Quantities of heat flux, mass blowing rate and translational temperature plotted along the wall with ablating wall conditions.*

The predicted heat transfer and mass blowing rate, using 1^{st}- and 2^{nd} -order(VL) is presented in Figure 6.5 (a). The heat flux value observed in the non-ablating case has been reduced following the activation of the ablating boundary conditions. However, over the flare region, the value of heat flux with ablation appears to be higher than in the case without. The reason for this behaviour is not clear and further investigation is needed. The difference between heat flux results over the body (with ablating effects), obtained for the 1^{st}-order and 2^{nd}-order

reconstruction schemes, appear to be quite similar. However, it must be noted that the heat flux predicted by the 2^{nd}-order reconstruction scheme is 20% higher, compared to the 1^{st}-order results over the stagnation region.

The corresponding mass blowing rate is presented in Figure 6.5 (b). As expected, the highest mass blowing rate is visible at the nose region where the highest heat flux as well as the translational-temperature prevail (see Figure 6.5 (c)). The mass fractions of species in free stream are listed in table 6.1; to prevent division by zero the mass fractions of species other than N_2 and O_2 have been initialised with a value of 10^{-8}. Immediately behind the shock, before the nose region, N_2 and O_2 start to dissociate into atoms forming N and O; followed by the formation of NO. The peak temperature behind the shock is higher than what was observed in non-ablating conditions.

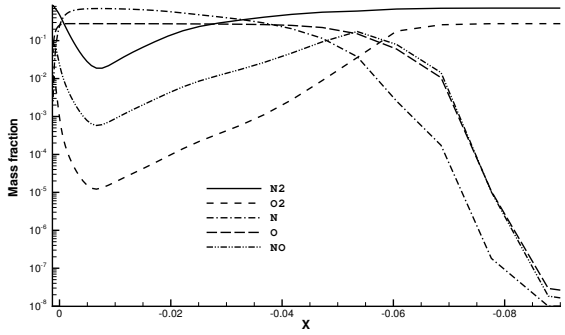

(a) Mass fractions

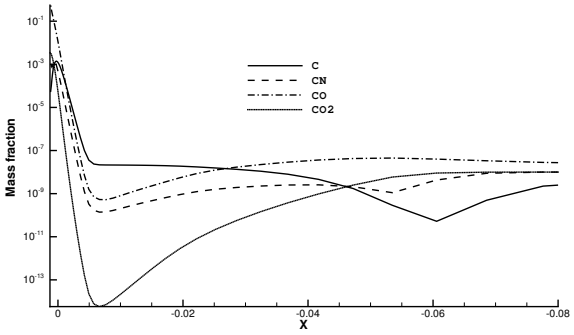

(b) Mass fractions

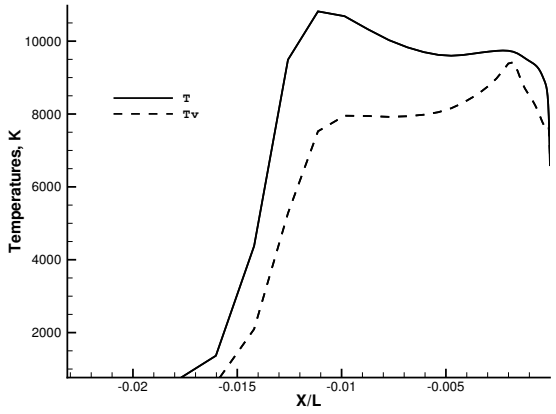

(c) Two temperatures

Figure 6.6 — *Mass fractions and two temperatures plotted along the stagnation streamline.*

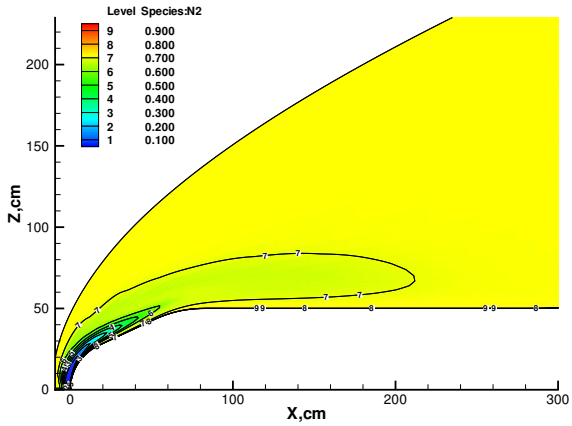

(a) N_2

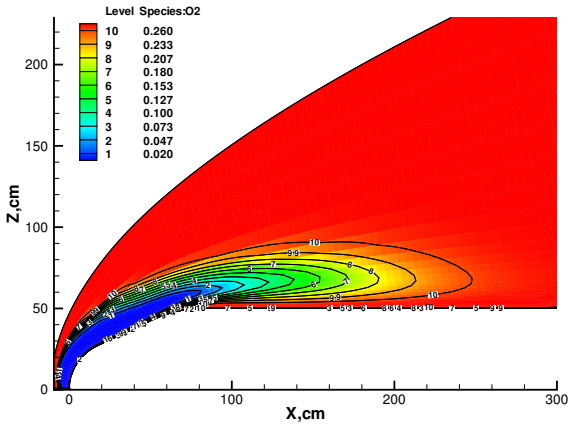

(b) O_2

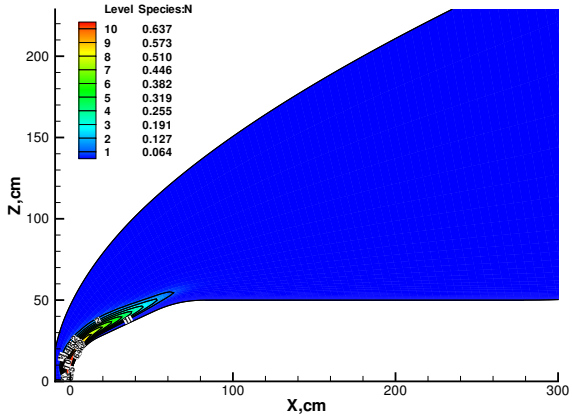

(c) N

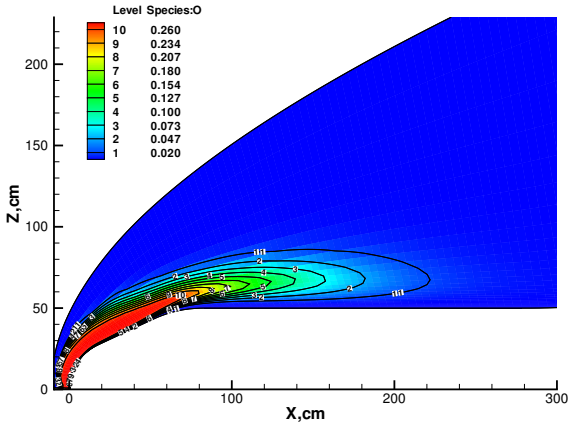

(d) O

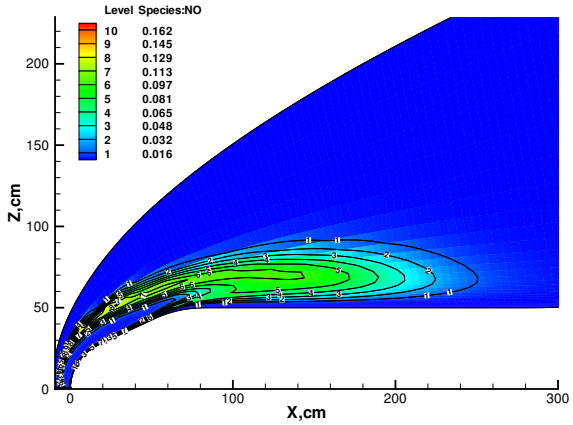

(e) NO

Figure 6.7 — *Species mass fractions of non-Carbon particles.*

Due to the ablating effects, species C, CO, CO_2, and CN are also of significance; that is the

reactions presented in the Equation 2.5.10 through 2.5.21 are presumed to be active. This is true, as the mass fractions of C, CO, CO_2, and CN spike near the surface at the nose region as seen in Figures 6.6 (a) and (b). Among the Carbon related species, the highest mass fraction is observed for the species CO. Rather interestingly, molecules N_2, O_2, and NO, seem to be re-forming near the wall. The peak values for translational and vibrational temperatures at the nose are 10850K and 9400K repectively (see Figure 6.6 (c)). The mass fractions of non-carbon particles present within the flow are presented in Figure 6.7.

6.7 Ablation Effects on Double-cone

The experimental conditions for the run designated 47[78,157] conducted in the LENS-I shock tunnel at Calspan University Buffalo Research Center (CUBRC), have been used for the validation. The experimental data obtained for the Run 47 assuming steady flow with typical no-slip wall conditions. The geometry of the double-cone flare is available in chapter 5(see Figure 5.1). Air has been used as the test gas and the experiments were conducted with total enthalpy of 9MJ/kg. The free-stream parameters are listed in Table 6.2. As mentioned earlier in Chapter 5 it is imperative that careful attention must be given to the grid generation aspect of the problem. Supersonic inflow and outflow (extrapolated conditions), symmetry along the cone axis, and no-slip on wall, have been used as the boundary conditions at initialisation.

Simulations were carried out with and without ablating boundary conditions in order to compare the difference in heat transfer. For the runs without ablation the surface temperature was set to 296.2K, whereas for ablation runs the temperature is during the solution procedure. All runs were performed utilising a 128 $\times$ 48 mesh in conjunction with the 2^{nd}-order numerical reconstruction scheme and the van-Leer limiter. For convenience, the case without ablation is henceforth labelled to as Case A. Similarly, the case with full ablating boundary conditions is referred to as Case B. The results for Case A and Case B are presented below. The separation zone formed over the region between the first and the second cone is the primary area of interest as the flow behaviour in this region is tightly coupled with the global flow characteristics, such as shock position over the double-cone geometry as well as wall heat transfer and pressure distributions. Figure 6.8 show the key flow features for Cases A and B. For Case A, the separation bubble formed over the cone junction extends almost half way over the first cone. The contour

plots in Figure 6.8 were presented in black and white; reason for this was to present a clear picture of the behaviour of flow nearer the wall during ablation.

Table 6.2 — *Flow conditions for the double-cone configuration:(Run 47).*

Case	005
M_∞	8.6
$Re_m(10^3/\text{m}$	393.7
T_∞(K)	628.9
T_v (K)	2128.89
T_w (K)	297.8
ρ_∞ (gm^{-3})	2.62×10^{-3}
C_{N_2}	0.73704
C_{O_2}	0.17160
C_N	1×10^{-8}
C_O	0.02659
C_{NO}	0.06477
C_C	1×10^{-8}
C_{CO}	1×10^{-8}
C_{CO_2}	1×10^{-8}
C_{CN}	1×10^{-8}

Figure 6.9 shows the pressure distribution for the cases with and without ablation. Without ablation the results for the pressure coefficient distribution agree well with the available experimental data except for the peak value, which is over-predicted by about 5%. The location of the peak value of the pressure coefficient distribution agrees well with the experimental data. The peak pressure coefficient in Case B is higher than A and additionally, larger pressure values occur downstream.

The mass and energy transfer due to the ablation of the surface results in a wider shock layer with the second shock formed over the second cone lying further away from the wall compared to Case A. Moreover, the subsonic region behind the shock over the second cone is considerably wider in Case B. The ablation effects also reduce the length of the separation region.

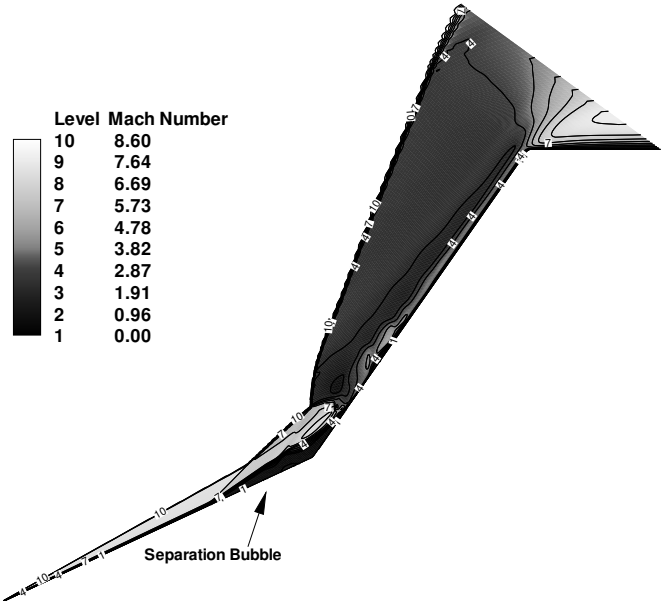

(a) Case A

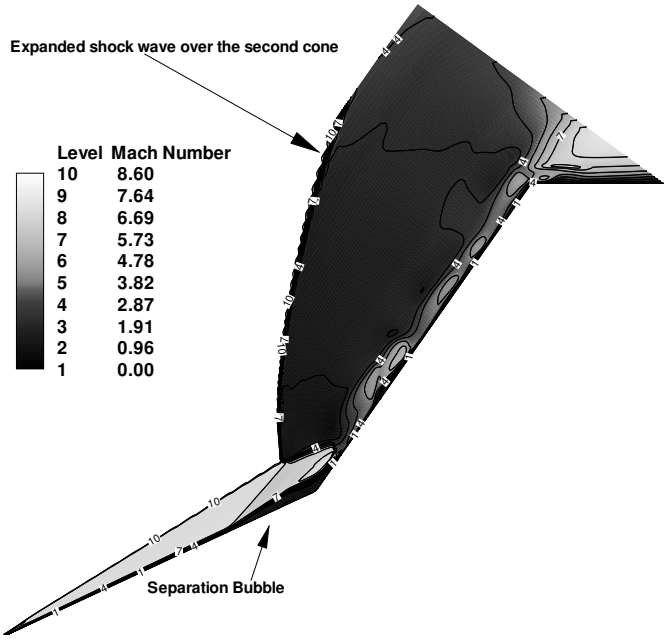

(b) Case B

Figure 6.8 — *Mach number contours plotted ablating and non-ablating cases showing the shock-shock interaction and separation region.*

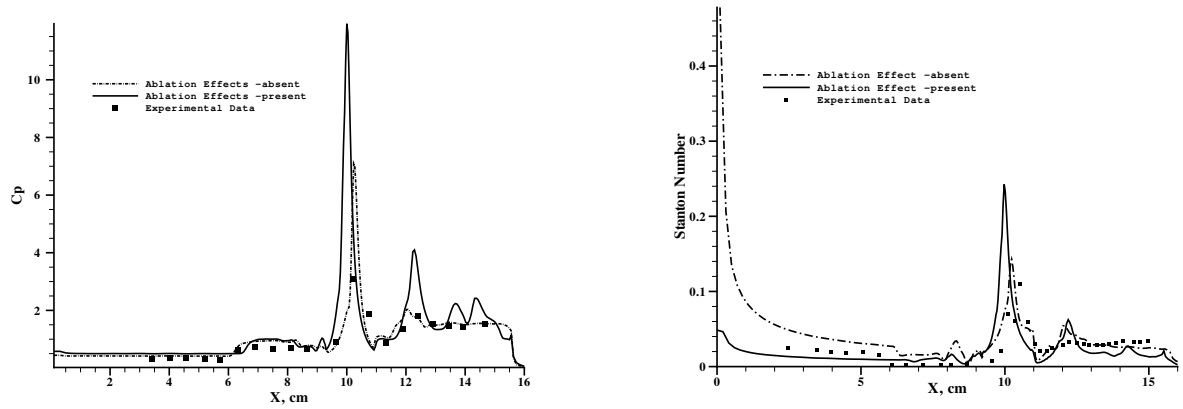

(a) Pressure (b) Heat transfer

Figure 6.9 — *Wall pressure coefficent and heat transfer (Stanton number) for cases with and without ablation.*

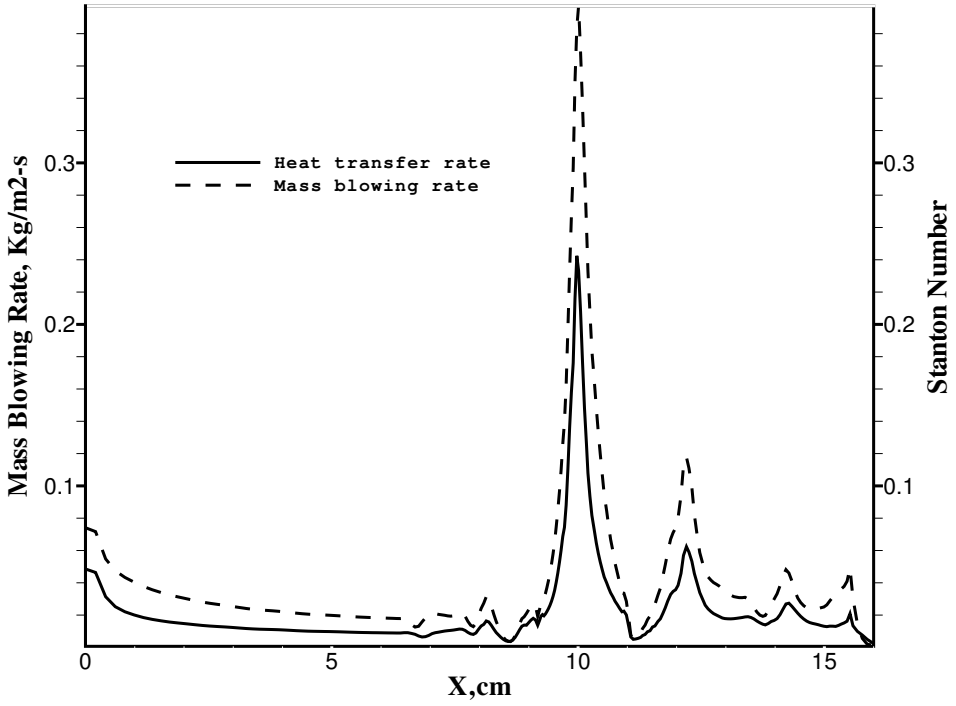

Figure 6.10 — *Comparison of Mass blowing rate and Stanton number distributions.*

Further comparisons are presented in Figure 6.9 for the heat transfer coefficient (Stanton number) over the surface cases A and B. In respect of Case A, some discrepancies between numerical and experimental data occur, but there is an overall reasonable agreement except in the

region over the first cone (upstream). A further grid refinement might improve the results in this region and this is a matter of future investigation.

The heat transfer near the nose is significantly reduced for the case with ablation. The reduced heat transfer in Case B continues over the entire length of the first cone. The numerically predicted peak heat transfer is higher in Case B than A. At present, the cause of this effect is not clear and further investigation is required. Downstream of the region of peak heat transfer, the heat transfer coefficient for Case B is overall smaller than in Case A. Figure 6.10 shows the predicted mass blowing rate over the surface, including the heat transfer distribution for case B. As expected, the mass blowing rate variation follows the wall heat transfer distribution. The maximum mass blowing rate occurs in the position of peak heat transfer.

One of the key aspects of this study is to observe the behaviour of ablating boundary conditions where chemical species engage in heterogeneous type reactions. Figures 6.11 through 6.13 are presented below to highlight the distribution of chemical species with and without the effect of ablation.

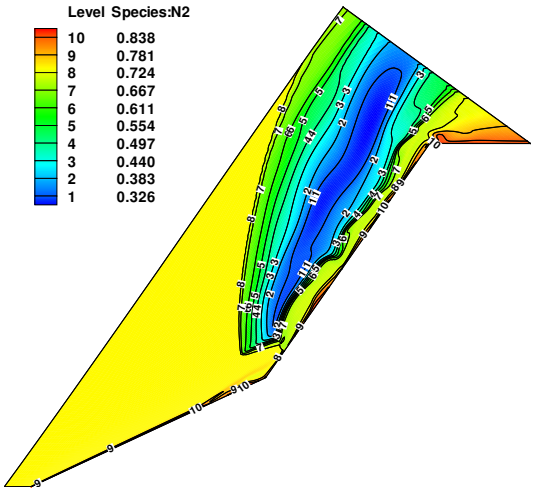

(a) N_2 Species, ablation: present

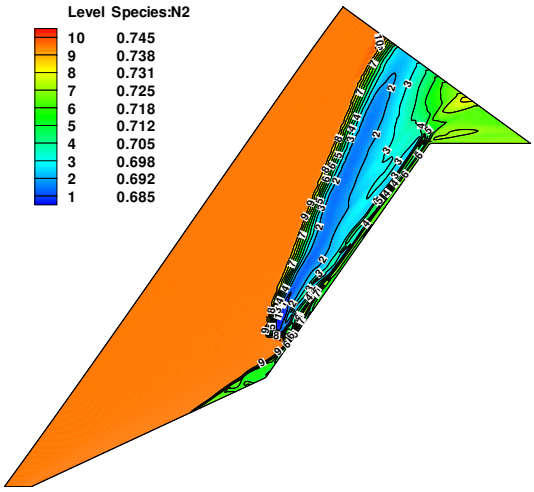

(b) N_2 Species, ablation: absent

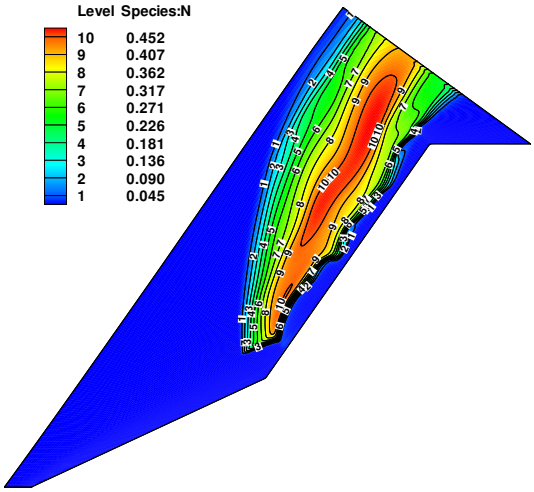

(c) N Species, ablation: present

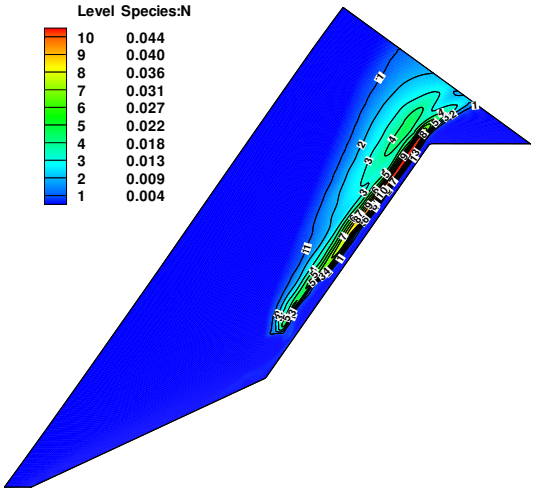

(d) N Species, ablation: absent

Figure 6.11 — *The contours of Nitrogen molecule and atoms distribution with and without ablation.*

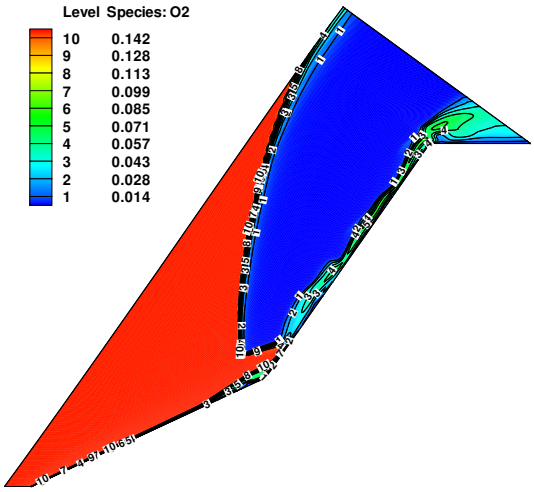

(a) O_2 Species, ablation: present

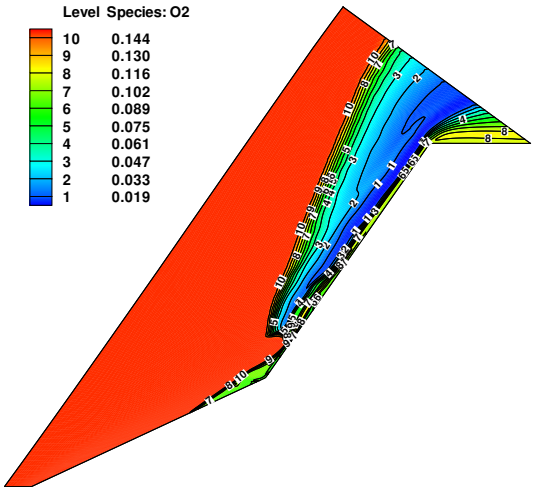

(b) O_2 Species, ablation: absent

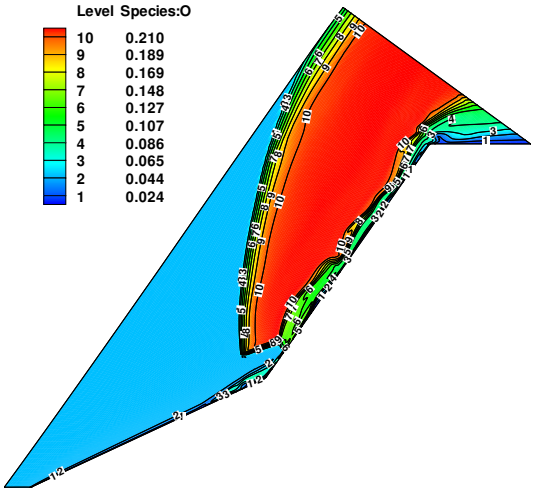

(c) O Species, ablation: present

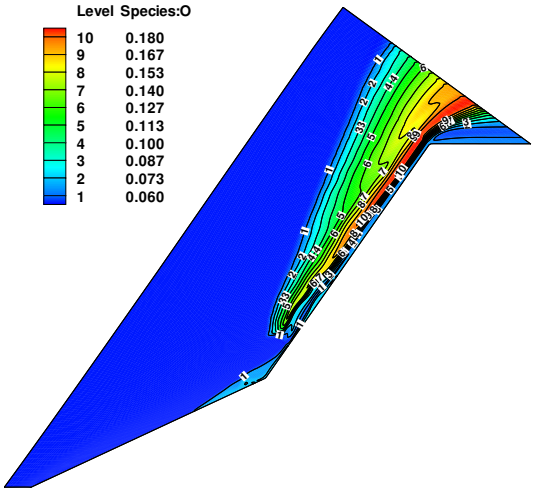

(d) O Species, ablation: absent

Figure 6.12 — *The contours Oxygen molecules and atoms distribution with and without ablation.*

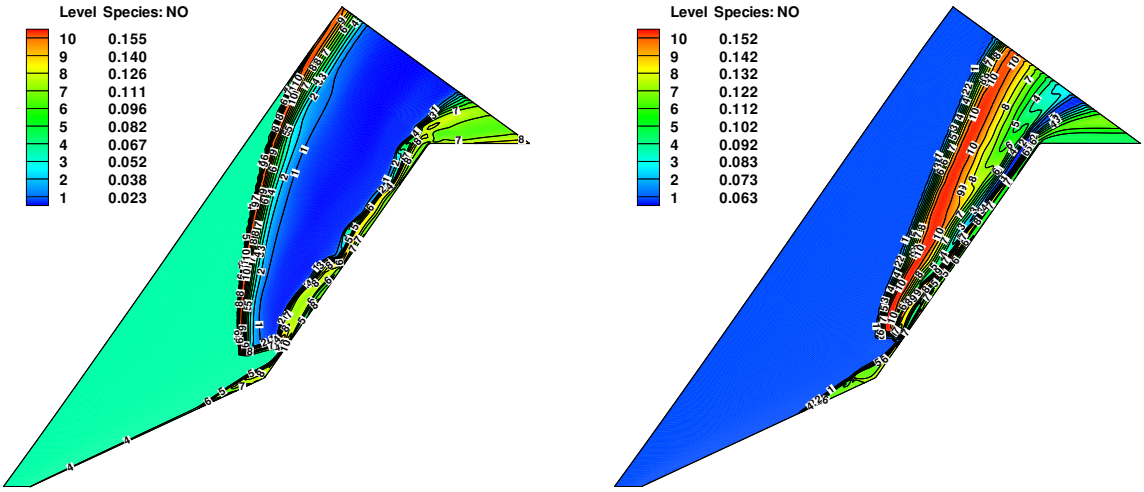

(a) NO Species, ablation: present

(b) NO Species, ablation: absent

Figure 6.13 — *The contours Nitrogen Oxide molecule distribution with and without ablation.*

6.8 Summary

Numerical experiments were carried out to ascertain the effects of the ablating boundary condition under the high enthalpy real gas assumption. In the case of HB-2 flare, it was previously observed that, the heat transfer predicted by the CNS3D numerical code under non-ablating conditions agrees well with the experiment. In this chapter, the absolute values of heat flux for cases with and without ablation were compared; the results show that the activation of the ablating boundary condition minimises the heat flux at the stagnation nose region.

When considering the double-cone flow, the numerical heat flux results for the double-cone obtained without ablation agree well with the experiment. The use of ablating boundary conditions showed that they have significant effects on the heat transfer coefficient, especially over the second cone. The position of peak mass blowing rate corresponds to peak heat transfer. However, the effects of ablation at the point of shock impingent are not entirely clear and further investigation is needed.

CHAPTER 7

Summary , Conclusions, and Future Work

'If'

An Ephor of Sparta to Alexander the Great (356 –323 BC)

7.1 Summary

In recent years there has been a growing interest in CFD methods for aerospace problems. As the numerical techniques become increasingly reliable and robust, the range of applications is ever on the rise. CFD techniques have been successfully employed in hypersonic flow modelling. Due to the complex nature of the flow at high Mach numbers, the verification and validation of physical and numerical models is undoubtedly an area of vital importance in hypersonic flow research.

The computational code CNS3D was utilised for the work carried out and presented in this thesis. The Compressible Navier-Stokes Solver (CNS3D), developed over number of years by Drikakis *et al*, has been utilised to tackle many complex flow problems; it includes a selection of high-order methods of both TVD and WENO type. However, the extension to model non-equilibrium flow at high Mach numbers was not available. The work presented in this thesis was motivated by the code validation effort following the supplement of additional models and governing equations to tackle high speed flow phenomena.

The main aim of this work has been to facilitate the application of higher-order methods in non-equilibrium hypersonic flow, in the way of implementing numerous physical models and additional governing equations. The need for the additional terms arises from the complex phenomena that become dominant due to high energy present within the flow. Various effects, such as diffusion, thermal and chemical non-equilibrium, and the activation of additional energy modes, are not present or dominant in a typical ideal gas flow.

The experiments of hypersonic flow over HB-2 flare and double-cone performed in the test facilities ONERA, JAXA, and LENS-I have been simulated. These test cases were chosen partly because of the availability of experimental data and the potential of being simulated as axi-symmetric problems (requiring only a 2D grid), but mostly because they give rise to complex flow features that are excellent for code validation.

In addition to non-equilibrium flow, ablating boundary conditions have also been implemented in the computational code. The aforementioned test cases, as well as the Phenolic blunted flare have been used for validation of the gas-surface interaction model alongside the high enthalpy flow. Only non-charring ablation was considered. With the inclusion of ablation effects, the

CNS3D code is equipped to handle nine species, with 54 potential chemical reactions. Furthermore, the two temperature model proposed by Park as well as additional governing equation for vibration energy has been implemented in order to account for the vibrational temperature. The governing equations as well as the numerical methods utilised in this work have been discussed in detail in chapters 1 and 2.

The first stage of validation focuses on the flow over the HB-2 flare. So far, only few computational studies have investigated the HB-2 flow. Therefore, the validation study carried out in this thesis, over several Mach numbers with perfect and real gas assumptions, can be regarded as a significant contribution to the overall validating effort of this test case.

Low enthalpy flow (1MJ/kg) with Mach numbers ranging from 17.9 to 5 was simulated with perfect gas assumption; this was to ascertain the overall performance and robustness of the higher-order methods. It was shown that WENO does not perform well in cases above Mach number 10. Furthermore, the performance of the CNS3D code was compared with the commercial software FLUENT. It was discovered that in 1^{st} -order special reconstruction, the performance of both codes are quite similar. However, it is possible to increase the reconstruction accuracy to 9^{th}- order in the CNS3D, where the separation bubble over the cylinder flare junction was accurately predicted; FLUENT did not reproduce the separation bubble in the 2^{nd}-order AUSM method.

The HB-2 flare was also simulated using real gas flow assumption, where the heat flux to the surface was adequately captured by both 2^{nd}-order VL and 5^{th}-order WENO reconstruction methods; WENO with 9^{th}-order reconstruction accuracy was observed to be too unstable and therefore suffered convergence problems.

To further validate the CNS3D code, the double-cone flow was simulated. The test case is regarded as being excellent for code validation. As it was the case in HB-2, the double-cone was simulated using both perfect and real gas assumption with varying Mach numbers; furthermore, the CNS3D code was compared with the commercial code FLUENT by simulating the flow over the double-cone. It was seen that the CNS3D performed well with 2^{nd}- and 9^{th}-order reconstruction methods to capture the separation bubble formed over the cone junction in perfect gas simulation. As observed earlier, the 9^{th}-order reconstruction accuracy was too unstable to attain any useful results in the case of the real gas flow. However, the WENO scheme with 5^{th}-order reconstruction accuracy captured the separation well, compared to the typical 2^{nd}-order VL scheme. However, the peak heat transfer observed at the point where flow

impinges on the surface after the separation, predicted by the experiment was not matched in all cases. It was also observed that the position of the heat transfer appears to move away from the tip of the double-cone with increment of the order of reconstruction. The less dissipative WENO scheme always predicts the largest separation bubble.

Finally, ablating boundary conditions with varying wall temperature were introduced where the flow over the HB-2, and the double-cone was simulated. For the HB-2, as well as the double-cone, the most important aspect of an ablating boundary, the heat transfer reduction, was satisfied. The heat flux predicted at the nose for the HB-2 flare has been reduced. This trend continues over the entire surface save over the cylinder-flare junction region. A similar discrepancy is observed in the double-cone flare, where the peak heat transfer appears to be higher with ablation than without. The cause for this discrepancy is a matter for further investigation. The WENO scheme with 5^{th} and 9^{th}order of accuracy was observed to be unstable and therefore, only 2^{nd}-order VL results were presented.

7.2 Conclusions

One of the main objectives of this work was to establish the improvement of accuracy gained from increasing the order of reconstruction compared to the improvement made via the increment in grid resolution. In the case of the double-cone flow, it is clear that the WENO scheme (with 5^{th} or 9^{th} -order reconstruction accuracy) outperforms the typical 2^{nd}- order VL scheme over all grid resolutions utilised, by predicting the length of the separation bubble more accurately. However, this observation is not so clear cut in the HB-2 flow. WENO scheme was observed to be too unstable when attempted to simulate the very high speed flow of Mach number 17. Yet when the Mach number was reduced, Mach 7.5 and 5, the WENO reconstruction outperformed the 2^{nd}-order VL. Therefore, it can be concluded that, as far as the Mach number is kept sufficiently smaller (comparatively), that is below the Mach 10, increasing the order of reconstruction would be an ideal way of improving the accuracy compared to increments in grid density.

It was observed that the HB-2 runs, performed for Mach numbers 17.8, under predict the heat flux over the nose region significantly. As during decent nose region is expected to see the highest heat flux, it is vital that the heat transfer to the wall is predicted accurately. The main

issue in this case is the lack of experimental conditions presented in the literature. As the experiments were carried out in the 60's and the available information is limited, it is difficult to pinpoint the exact free stream conditions. However, this is an excellent opportunity for what is referred to as blind comparison study. As the free stream values are based on an educated guess, future experimental work can take into account the conditions listed and compare the stagnation heat transfer values predicted by CFD.

In CFD, it is vital to take into account as many physical processes as possible and describe them via physical models. However, as the number of physical processes and reactions included increase, the burden on computational resources increase and the whole process becomes very expensive. The only alternative is to identify which processes are more important than others. It is also crucial to treat, where possible, all phenomena as being interlinked. The ablation wall boundary conditions imposed draw values from the flow field, and subsequently feedback information into the flow. This process, even though more difficult to model, provides undoubtedly a better estimation of heat transfer or other physical quantity which may be desired.

In previous studies it was established that the prediction of the separation bubble over the cone flare junction in the double-cone flow is an indicator of the effectiveness of the numerical methods employed in the CFD code. As it is clear that both WENO and VL schemes predict the separation zone length quite accurately, it can be concluded that the models implemented are reasonably validated. Moreover, the numerical models, such as the reconstruction methods as well as the HLLC Riemann solver utilised in this work, are effective under low and high enthalpy chemically reacting conditions.

The main points of this study's findings are summarised as follows;

- Stagnation point values for flow over HB-2 flare test case with varying Mach number from 5 to 17.8 have been obtained, which would aid future validation efforts[147].
- The behaviour of very higher order WENO methods, at high Mach numbers has been established with regards to the blunted nose HB-2 flare[147]. At Mach numbers above 10 WENO-P does not perform well.
- Increasing the order of reconstruction is a much more cost-effective way of gaining accuracy compared to increments in grid resolution[147]. However the order of reconstruction accuracy cannot be increased indefinitely, even with the use of the WENO scheme. The

experience in this work suggests that the optimal order accuracy for the WENO scheme is 5, whereas beyond that the reconstruction algorithm in the face of strong shocks becomes less reliable as oscillations materialise.

- As it was mentioned in previous studies, it is not entirely necessary to use implicit time integration for double-cone computations, as it is quite possible to achieve a converged solution using domain decomposition with MPI, coupled with explicit time marching.
- Ultimatly, it is a constant trade-off between, accuracy, robustness and efficiency and the study concludes that, for high Mach number chemically reacting flows, high-order schemes, 5th-order WENO scheme in particular is exceedingly good value for money.

7.3 Recommendation For Future Work

The computational code CNS3D is robust and effective in many areas of CFD research. With regards to hypersonic flow modelling, it is recommended that the code is extended to tackle plasma flow physics with inclusion of charged particles within the flow field. Furthermore, the existing ablation model can be extended to include other TPM, such as SiC, and high temperature phenomena, such as radiation. It is also recommended that 'reconstruction' step of the high-resolution methods is carried out via the use of characteristic variables; implementation of these variables within the block-structured version of CNS3D is necessary. It is expected that the implementation of characteristic variables will aid CNS3D to iron out the instabilities observed when utilising the WENO scheme with 9^{th} -order reconstruction accuracy.

In spite of the existence of several studies related to code validation using various test cases, in recent years experimental and computational work carried out in the field of hypersonic flow is comparatively limited. Even institutions, such as NASA, suffer from funding issues for hypersonic related research, such as TPS design and aero-thermodynamics[†]. As there is a distinct lack of understanding related to high-speed non-equilibrium flow modelling, it is vital that more experimental data is made available for the purpose of CFD validation. For instance, in the case of HB-2 there has been no experimental work carried out recently, save the tunnel calibration study conducted at JAXA. Therefore, it is important that more experimental work

[†]Personal communication: Dr Frank Milos, TPS design branch, Ames Research Centre (ARC), NASA frank.s.milos@nasa.gov

is perused, highlighting the exact free stream conditions, which would be invaluable for cross validation using CFD and for code validation purposes.

APPENDIX A

Constants and Coefficients for Various Physical Models

A.1 The values of constants used in various physical models

This section introduces several constants used in various physical models throughout the thesis. First off all the Charachteristic temperatures of species used for the calculation of vibrational energy are:

Table A.1 — Characteristic temperature of species

Species	M_s	θ_{vrs} (K)	θ_s(K)	h_s^0,kcal/g-mole	$\tilde{D}_s$,eV	A_s
N_2	28	3395	5000	-	9.759	220
O_2	32	2239	3350	-	5.115	129
N	14	-	-	112.959	-	-
O	16	-	-	59.544	-	-
NO	30	2817	4040	21.6009	6.469	168

A.2 Coefficients for the Blottner Model

In order to calculate the species viscosity, Blottner Model can be used. The values of A_s,B_s, and C_s are given below.

Table A.2 — Viscosity coefficients for the Blottner Model

Species	A_s	B_s	C_s
N_2	0.0268142	0.3177838	-11.3155513
O_2	0.0449290	-0.0826158	-9.2019475
NO	0.0436378	-0.0335511	-9.5767430
N	0.0115572	0.6031679	-12.4327495
O	0.0203144	0.4294404	-12.6031403

A.3 Forward and Backward Reaction Rates

The forward reaction rate $k_{f,r}$ and backward reaction rate $k_{b,r}$ pertaining to five non-carbon particles are presented below (see Table A.3 and A.4); for convienience it is referred to as **option 1**. The coefficients needed to calculate $k_{f,r}$ and $k_{b,r}$ are tabulated in Table A.5, for five non carbon species; this is referred to as **option 2**.

Option: 1

Table A.3 — Forward reaction rates $k_{f,r}$,cm^3/mole-sec; Gupta *et al* (1990)[66].

Reaction	Partners	$k_{f,r}$,cm^3/mole-sec
1(Eq.2.5.5)	O_2, NO, O, N	$1.92\times 10^{17}T^{-0.5}\exp(-1.131\times 10^5/T)$
2(Eq.2.5.6)	O_2,N_2,NO,O,N	$3.61\times 10^{18}T^{-1.0}\exp(-5.94\times 10^4/T)$
3(Eq.2.5.7)	O_2,N_2,NO,O,N	$3.97\times 10^{20}T^{-1.5}\exp(-7.56\times 10^4/T)$
4(Eq.2.5.8)	-	$6.75\times 10^{13}\exp(-3.75\times 10^4/T)$
5(Eq.2.5.9)	-	$3.18\times 10^{9}T^{1.0}\exp(-1.97\times 10^4/T)$

Table A.4 — Backward reaction rates $k_{b,r}$,cm^3/mole-sec

Reaction	Partners	$k_{b,r}$,cm^3/mole-sec
1(Eq.2.5.5)	O_2, NO, O, N	$1.09\times 10^{16}T^{-0.5}$
2(Eq.2.5.6)	O_2,N_2,NO,O,N	$3.01\times 10^{15}T^{-0.5}$
3(Eq.2.5.7)	O_2,N_2,NO,O,N	$1.01\times 10^{20}T^{-1.5}$
4(Eq.2.5.8)	-	1.5×10^{13}
5(Eq.2.5.9)	-	$9.63\times 10^{11}\ T^{0.5}\exp(-3.6\times 10^3/T)$

Table A.5 — Coefficients needed for calculating $k_{f,r}$;source Candler (1988)[22].

Reaction	Partner	$C_{f,r}(m^3/kgs)$	η_m	θ_{dm}(K)
1(Eq.2.5.5)	N_2	3.7800×10^{18}	-1.600	113200
	O_2	3.7800×10^{18}	-1.600	113200
	N	1.110×10^{18}	-1.600	113200
	O	1.110×10^{18}	-1.600	113200
	NO	3.7800×10^{18}	-1.600	113200
2(Eq.2.5.6)	N_2	2.75×10^{16}	-1.00	59500
	O_2	2.75×10^{16}	-1.00	59500
	N	8.250×10^{16}	-1.00	59500
	O	8.250×10^{16}	-1.00	59500
	NO	2.75×10^{16}	-1.00	59500
3(Eq.2.5.7)	N_2	2.30×10^{14}	-0.500	75500
	O_2	2.30×10^{14}	-0.500	75500
	N	4.60×10^{14}	-0.500	75500
	O	4.60×10^{14}	-0.500	75500
	NO	2.30×10^{14}	-0.500	75500
4(Eq.2.5.8)	-	3.180×10^{10}	0.100	37700
5(Eq.2.5.9)	-	2.160×10^{5}	1.29	19220

In order to calculate the backward reaction rate, equilibrium constant $K_{eq,r}$ can be used. That is

$$k_{b,r} = \frac{k_{b,r}(T)}{K_{eq,r}(T)}, \tag{A.3.1}$$

and using the expresion provided by Park (1985)[127,128] $K_{eq,r}$ can be calculated

$$K_{eq,r} = \exp(A_{1r} + A_{2r}Z + A_{3r}Z^2 + A_{4r}Z^3 + A_{5r}Z^4) \tag{A.3.2}$$

The coefficients A_{1r} to A_{5r} for reactions 1 through 5 are presented below.

Table A.6 — Coeffients needed for calculating $k_{f,r}$

Reaction	A_{1r}	A_{2r}	A_{3r}	A_{4r}	A_{5r}
1	3.898	-12.611	0.683	-0.118	0.006
2	1.335	-4.127	-0.616	0.093	-0.005
3	1.549	-7.784	0.228	-0.043	0.002
4	2.349	-4.828	0.455	-0.075	0.004
5	0.215	-3.652	0.843	-0.136	0.007

Coefficients of Surface Efficiency for Ablation Model

Table A.7 — Efficiency of surface reaction for Park's Ablation model.

Species	β_s
O_2	0.5
N	0.3
O	$0.63 * \exp(-1160/T_w)$

APPENDIX B

Numerical Models and Calculations

B.1 Axi-symmetric Formulation

When considering a domain that is symmetric around a coordinate direction, a two dimensional problem with geometric source term can be used to simulate a three dimensional problem. To this effect, the eq. 2.2.1 is reformed with cylindrical coordinates to allow the grid to be treated as two-dimensional Cartesian with additional source terms. The axi-symmetric source terms appear as S_{inv} and S_{visc} representing inviscid and viscous terms respectively[69].

$$\frac{\partial \boldsymbol{U}}{\partial t} + \frac{\partial \boldsymbol{F}}{\partial x} + \frac{\partial \boldsymbol{H}}{\partial z} + \alpha \boldsymbol{S}_{inv} = \frac{\partial \boldsymbol{F}_v}{\partial x} + \frac{\partial \boldsymbol{H}_v}{\partial z} + \alpha \boldsymbol{S}_{visc} \tag{B.1.1}$$

where $\alpha = 1$ and

$$\boldsymbol{S}_{inv} = \frac{1}{r} \begin{bmatrix} \rho_{N_2} u \\ \rho_{O_2} u \\ \vdots \\ \rho_{CN} u \\ \rho u w \\ \rho w^2 \\ (E+p)w \\ E_v w \end{bmatrix}, \tag{B.1.2}$$

$$\boldsymbol{S}_{visc} = \frac{1}{r}\begin{bmatrix} \rho D_{N_2}\frac{\partial y_{N_2}}{\partial z} \\ \rho D_{O_2}\frac{\partial y_{O_2}}{\partial z} \\ \vdots \\ \rho D_{CN}\frac{\partial y_{CN}}{\partial z} \\ \tau_{xz} - \frac{2}{3}z\frac{\partial}{\partial x}\left(\mu\frac{w}{z}\right) \\ \tau_{zzp} - \tau_{\theta\theta} - \frac{2}{3}\mu\left(\frac{w}{z}\right) - \frac{2}{3}z\frac{\partial}{\partial z}\left(\mu\frac{w}{z}\right) \\ u\tau_{xz} + w\tau_{zzp} - q_z - \frac{2}{3}\mu\left(\frac{w^2}{z}\right) - z\frac{\partial}{\partial z}\left(\frac{2}{3}\mu\frac{w^2}{z}\right) - z\frac{\partial}{\partial x}\left(\frac{2}{3}\mu\frac{uw}{z}\right) \\ k_v\frac{\partial T_v}{\partial z} + \rho\sum_{s=1}^{n} h_{v_s}D_s\frac{\partial y_s}{\partial z} \end{bmatrix}. \tag{B.1.3}$$

Here w is the radial velocity, (which is z velocity in CNS3D [†] code). All other notations are conventional. The viscous stresses are given by

$$\tau_{xxp} = \mu\left(\frac{4}{3}\frac{\partial u}{\partial x} - \frac{2}{3}\frac{\partial w}{\partial z}\right), \quad \tau_{zzp} = \mu\left(\frac{4}{3}\frac{\partial w}{\partial z} - \frac{2}{3}\frac{\partial u}{\partial x}\right),$$
$$\tau_{xz} = \mu\left(\frac{\partial u}{\partial z} + \frac{\partial w}{\partial x}\right), \quad \tau_{\theta\theta} = \mu\left(-\frac{2}{3}\left(\frac{\partial u}{\partial x} + \frac{\partial w}{\partial z}\right) + \frac{4}{3}\frac{w}{z}\right)$$
$$q_x = -k\frac{\partial T}{\partial x}, \quad q_z = -k\frac{\partial T}{\partial z}$$

B.2 HLL Riemann Solver Fomulation

The Riemann solver designed by Harten *et al* is refered to as HLL and has been implemented in the computational code CNS3D. The left and right states of the acoustic wave speeds, that is S_R and S_L are calcaulated.

The HLL solver describes the conservative varible $\boldsymbol{U}$ and the inercell flux $\boldsymbol{E}$ in the following

[†] details about CNS3D code will be exaplined later on.

manner

$$\boldsymbol{U} = \begin{cases} \boldsymbol{U}_L & \text{if} \quad S_L > 0, \\ \boldsymbol{U}_* & \text{if} \quad S_L \leq 0 < S_R, \\ \boldsymbol{U}_R & \text{if} \quad S_R < 0 \end{cases} \tag{B.2.1}$$

and

$$\boldsymbol{E} = \begin{cases} \boldsymbol{E}_L & \text{if} \quad S_L > 0, \\ \boldsymbol{E}_* & \text{if} \quad S_L \leq 0 < S_R, \\ \boldsymbol{E}_R & \text{if} \quad S_R < 0 \end{cases} \tag{B.2.2}$$

where

$$\boldsymbol{U}^* = \frac{S_R U_R - S_L U_L - (E_R - E_L)}{S_R - S_L}, \qquad \boldsymbol{E}^* = \frac{S_R E_R - S_L E_L - S_R S_L (U_R - U_L)}{S_R - S_L}$$

REFERENCES

[1] AMARATUNGA, S., TUTTY, O. & ROBERTS, G. (2000). High-speed flow with discontinuous surface catalysis. *J. Fluid Mech*, **Vol. 420**, pp325–359. 6

[2] ANDERSON, J.D. (2000). *Hypersonic and High Temperature Gas Dynamics*. American Institute of Aeronautics and Astronautics, Reston, VA 20191. 3, 4, 120, 123

[3] ANTONIO, V. & GIUSEPPE, P. (2007). Catalytic effects on non-equilibrium aerothermodynamics of a reentry vehicle. *AIAA Paper 2007-1211*. 5

[4] ARMENISE, I., BARBATO, M., CAPITELLI, M. & KUSTOVA, E. (July- September 2006). State-to-state catalytic models, kinetics, and trasport in hypersonic boundary layers. *Jnl of Thermophysics and Heat Transfer*, **Vol. 20**, pp. 465–476. 6

[5] AYASOUFI, A., RAHMANI, R.K., CHENG, G., KOOMULLIL, R. & NEROORKAR, K. (2006). Numerical simulation of ablation for reentry vehicles. *AIAA Paper 2006-2908*. 127

[6] BAGABIR, A. & DRIKAKIS, D. (2004). Numerical experiments using high-resolution schemes for unsteady, inviscid, compressible flow. *Computer Methods in Applied Mechanics and Engineering*, **Vol. 193**, pp 4675–4705. 9, 45, 56, 64, 76, 120

[7] BALSARA, D. & SHU, C. (2000). Monotonicity preserving weighted essentially non-oscillatory schemes with increasingly high order of accuracy. *Journal of Computational Physics*, **Vol. 160**, pp 405–452. 8, 50

[8] BARBATO, B., BELLUCCI, V. & BRUNO, C. (1998). Effects of catalytic boundary conditions accounting for incomplete chemical energy accomadation. *AIAA Paper 98-2846*. 5

[9] BERTIN, J. (1994). *Hypersonic Aerothermodynamics*. American Institute of Aeronautics and Astronautics. 3, 4, 123

[10] BERTIN, J.J. & CUMMINGS, R. (2006). Critical hypersonic aerothermodynamic phenomena. *Annual Review of Fluid Dynamics*, **Vol. 38**, pp 129–157. 7, 94

[11] BERTIN, J.J. & CUMMINGS, R.M. (2006). Critical hypersonic aerothermodynamic phenomena. *Annual Review of Fluid Mechanics*, **Vol. 38**, pp 129 – 157. 3, 5

[12] BERTOLAZZI, E. (1998). A finite volume scheme for two-dimensional chemically reactive hypersonic flow. *International Journal for Numerical Methods for Heat and Fluid Flow.*, **Vol.8 (8)**, pp. 888–933. 3

[13] BIANCHI, D., NASUTI, F., MARTELLI, E. & ONOFRI, M. (2007). A numerical approach for high-temperatures flows over ablating surfaces. *AIAA Paper 2007-4537*. 120

[14] BIRCH, T., PRINCE, S.A., LUDLOW, D.K. & QIN, N. (2001). The application of a parabolized navier-stokes solver to some hypersonic flow problems. *AIAA/NAL − NASDA − SAS International Space Planes and Hypersonic Systems and Technologies Conference, Kyoto, Japan, AIAA Paper 2001-1753*. 11, 12, 64

[15] BISCEGLIA, S. & RANUZZI, G. (2005). Real gas effects on a planetary re-entry capsule. *AIAA/CIRA 13th International Space Planes and Hypersonic Systems Technologies, AIAA Paper 2005-3385*. 7

[16] BLAZEK, J. (2001). *Computational Fluid Dynamics: Principles and Applications*. Elsevier Science LTD. 7, 25

[17] BLOTTNER, F. (1970.). Prediction of the electron density in the boundary layer on entry vehicles with ablation. In *The Entry Plasma Sheath and its Effects on Space Vehicle Electromagnetic Systems, NASA SP-252*. 6

[18] BORGES, R., CARMONA, M., COSTA, B. & DON, W. (2008). An improved weighted essentially non-oscillatory scheme for hyperbolic conservation laws. *Journal of Computational Physics*, **Vol. 227**, pp. 3191–3211. 8

[19] BOSE, D. & CANDLER, G.V. (1997). Simulation of hypersonic flows using a detailed nitric oxide formation model. *Physics of Fluids*, **Vol. 9(4)**, pp. 1171–1181. 7, 94

[20] BOYD, D., CANDLER, V.G. & LEVIN, A.D. (1995). Dissociation modeling in low density hypersonic flows of air. *Phys. Fluids*, **Vol. 7**, pp 1757. 3, 7

[21] BRUNO, C. & BARBATO, M. (1995). Aerothermochemistry for hypersonic technology - physico-chemical input data. Tech. Rep. LS-1995-04, von Karmen Institute for Fluid Dynamic. 32

[22] CANDLER, G. (1988). *The Computation of Weakly Ionized Hypersonic Flows in Thermo-Chemical Nonequilibrium*. Ph.D. thesis, Stanford University. 30, 154

[23] CANDLER, G. (1995). Aerothermochemistry for hypersonic technology -chemistry for external flows. Tech. Rep. LS-1995-04, von Karmen Institute for Fluid Dynamic. 18, 19, 46, 54

[24] CANDLER, G., NOMPELIS, I. & DRUGUET, M.C. (2001). Navier-stokes predictions of hypersonic double-cone and cylinder-flare flow field. *AIAA Paper 2001-1024*. 10, 92

[25] CANDLER, G.V. & NOMPELIS, I. (2002). Cfd validation for hypersonic flight - real gas flows. *AIAA Paper 2002-0434*. 7, 11, 12, 64, 93, 94

[26] CHAMBERS, L.H. (September 1994). Predicting radiative heat transfer in thermochemical nonequilibrium flow fields: Theory and user's manual for the loran code. Tech. rep., NASA, NASA TM-4564. 104

[27] CHEATWOOD, F.M. & GNOFFO, P.A. (1996). User's manual for the langley aerothermodynamic upwind relaxation algorithm (laura). *NASA Technical Memorandum 4674*. 104

[28] CHEN, Y. & MILOS, F. (2004). Finite-rate ablation boundary conditions for a carbon-phenolic heat-shield. *AIAA Paper 2004-2270*. 6, 29, 125

[29] CHIU, C. & ZHONG, X. (1996). Numerical simulation of transient hypersonic flow using the essentially nonoscillatory schemes. *AIAA Journal*, **Vol. 34 (4)**, pp 655–661. 8, 45

[30] CLEVER, R.M. & DENNY, V.E. (1975). Response of charring ablators to severe aerodynamic and erosion enviorments. *Journal of Spacecrafts and Rockets*, **Vol. 12(9)**, pp 558–564. 120

[31] COBLISH, J.J., SMITH, M.S., HAND, T., CANDLER, G.V. & NOMPELIS, I. (2005). Double-cone experiment and numerical analysis at aedc hypervelocity wind tunnel no. 9. *43rd AIAA Aerospace Sciences Meeting and Exhibit - Meeting Papers, AIAA Paper 2005-0902*. 92, 96

[32] COUSTEIX, J., ARNAL, D., AUPOIX, B., BRAZIER, J.P. & LAFON, A. (1994). Shock layer and boundary layer in hypersonic flows. *Progress in Aerospace Sciences*, **Vol.30**, pp 95. 3, 122

[33] DRIKAKIS, D. (1996). Study of compressible flow bifurcation phenomena in sudden expansions. *Computational Fluid Dynamics*, **(eds. Desideri et al.), John Wiley & Sons Ltd**, pp. 312–318. 41

[34] DRIKAKIS, D. (2003). Advances in turbulent flow computations using high-resolution methods. *Progress in Aerospace Science*, **Vol (39)**, pp 405–424. 42, 43

[35] DRIKAKIS, D. & DURST, F. (1993). Numerical study of transonic turbulent separated flows. *Proceedings of 9th Symposium on Turbulent Shear Flows*, **Vol. 2, Kyoto, Japan, August 16-18**, pp. 203–1–203–4. 41

[36] DRIKAKIS, D. & DURST, F. (1994). Investigation of flux formulae in shock wave turbulent boundary layer interaction. *International Journal for Numerical Methods in Fluids*, **Vol. 18**, pp 385–413. 41

[37] DRIKAKIS, D. & DURST, F. (1994). Numerical investigation of viscous compressible flows with seperation on parallel computers. *Proceedings of the German Aeronautics and Aerospace Congress*, **publisged by DGLR, ed. G. Buergener, Paper 94-C2-049, Vol. I**, pp 347–405. 41

[38] DRIKAKIS, D. & RIDER, W. (2005). *High-Resolution Methods for Incompressible and Low-Speed Flows*. Springer. 8, 36, 42, 45, 55, 64

[39] DRIKAKIS, D. & SCHRECK, E. (1993). Development of implicit navier-stokes methods on mimd multi-processor systems. *AIAA Paper 93-0062 (11 pages)*, **Proceedings of the**

31st AIAA Conference, Aerospace Sciences Meeting, Reno, Nevada, 11-14 January. 41, 56

[40] DRIKAKIS, D. & TSANGARIS, S. (1990). Multigrid scheme for the compressible euler equations. *Journal of Applied Mathematics & Mechanics (Zeitschrift fÃijr Angewandte Mathematik Mechanik; ZAMM)*, **Vol 70 (6)**, pp. 663–666. 41

[41] DRIKAKIS, D. & TSANGARIS, S. (1991). An implicit characteristic flux averaging scheme for the euler equations for real gases. *International Journal for Numerical Methods in Fluids*, **Vol. 12**, pp. 711–726. 41, 56

[42] DRIKAKIS, D. & TSANGARIS, S. (1992). Upwind schemes for the navier-stokes equations from subsonic through hypersonic speeds. *Journal of Applied Mathematics & Mechanics (Zeitschrift fÃijr Angewandte Mathematik Mechanik; ZAMM)*, **Vol. 72 (5)**, 1992. 41

[43] DRIKAKIS, D. & TSANGARIS, S. (1993). On the accuracy and efficiency of cfd methods in real gas hypersonics. *International Journal for Numerical Methods in Fluids*, **Vol. 16 (9)**, pp 759–775. 7, 8, 41, 54, 56, 76

[44] DRIKAKIS, D. & TSANGARIS, S. (1993). On the solution of the compressible navier-stokes equations using improved flux vector splitting methods. *Applied Mathematical Modelling*, **Vol. 17**, pp 282–297. 41

[45] DRIKAKIS, D. & TSANGARIS, S. (1993). Real gas effects for compressible nozzle flows. *ASME Journal of Fluids Engineering*, **Vol. 115**, pp 115–120. 41

[46] DRIKAKIS, D., HAHN, M., MOSEDALE, A. & THORNBER, B. (2009). Large eddy simulation using high resolution and high order methods. *Philosophical Transactions Royal Society*, **Vol.367**, pp 2985–2997. 42

[47] DRUGUET, M., CANDLER, G. & NOMPELIS, I. (2006). Comparison of physical models in computations of high-enthalpy double-cone flows. *AIAA Paper 2006-3419*. 95

[48] DRUGUET, M.C., CANDLER, G.V. & NOMPELIS, I. (2005). Effect of numerics on navier-stokes computations of hypersonic double-cone flows. *AIAA Journal*, **Vol. 43 (3)**, pp. 616–623. 8, 10, 11, 55, 92, 93, 95, 97, 120

[49] EBERLE, A. (1987). Characteristic flux averaging approach to the solution of euler's equations. *VKI Lecture Series, Technical report*. 52

[50] FAY, J. & RIDDELL, F. (1958). Theory of stagnation point heat transfer in dissociated air. *Journal of Aeronautical Sciences*, **Vol. 25(2)**, pp 73–85. 7

[51] FUJITA, K., ABE, T. & SUZUKI, K. (June 1997). Air radiation analysis of superorbital reentry vehicle. *AIAA Paper 97-2561*. 7

[52] GAITONDE, D.V., W.CANUPP, P. & HOLDEN., M.S. (Oct-Dec 2002,). Heat transfer predictions in a laminar hypersonic viscous/inviscid interaction. *Journal of Thermophysics and Heat Transfer*, **Vol.16(4)**, pp 481–489. 95

[53] GHISLAIN, T., YVES, B. & DAVID, E.Z. (2005). Numerical study of non-equilibrium weakly ionized air flow past blunt bodies. *International Journal of Numerical Methods for Heat and Fluid Flow*, **Vol. 15 (5/6)**, pp 588–609. 7

[54] GILCHRIST, A.R. & WILLIAMS, M.J. (1974). Pressure distributions and forces on agard models hb1 and hb2 at m=7.5. Tech. rep., Aerodynamics Note 346, ARL. 12, 64

[55] GNOFFO, A., PETER, GUPTA, N.R. & SHINN, J.L. (1989). Conservation equations and physical models for hypersonic air flows in thermal and chemical nonequilibrium. *NASA Technical Paper 2867*. 24, 25, 32

[56] GNOFFO, P. (2007). Simulation of stagnation region heating in hypersonic flow on tetrahedral grids. *AIAA Paper 2007-3960*. 7, 52

[57] GNOFFO, P.A. (1999). Planetary-entry gas dynamics. *Annual Review of Fluid Dynamics.*, **Vol. 31**, pp 459–494. 7, 11, 93, 94

[58] GNOFFO, P.A., WEILMUENSTER, J., II, H.H., OLYNICK, D.R. & VENKATAPATHY, E. (NASA-AIAA-97-2473, 1997). Computational aerothermodynamic design issues for hypersonic vehicles. *AIAA Paper*, **2473**, 1–35. 123

[59] GOKCEN, T. & PARK, C. (January 1991). The coupling of radiative transfer to quasi 1-d flows with thermochemical nonequilibrium. Tech. rep., AIAA Paper 91-0570. 7

[60] GOLOVACHOV, Y.P. (1995). *Fluid Mechanics and Its Applications: Numerical Simulation of Viscous Shock Layer Flows, Volume 33*. Kluwer Academic Publishers. 6, 19

[61] GOSSE, R. & CANDLER, G. (2008). Evaluation of carbon-carbon ablation models using a fully coupled cfd solver. *AIAA Paper 2008-3908*. 6

[62] GOULARD, R. (1958). On catalytic recombination rates in hypersonic stagnation heat transfer. *Jet Propulsion*, **Vol. 28 (11)**, pp. 737–745. 6

[63] GRAY, J.D. (July 1964). Summary report on aerodynamic characteristics of standard models hb-1 and hb-2. Tech. rep., Von Karman Gas Dynamics Facility ARO, AEDC-TDR-64-137. 12, 64, 67, 69

[64] GREAVES, J. & LINNETT, J. (1958). The recombination of oxygen atoms at surface. *Transactions of the Faraday Society,*, **Vol. 54**, pp.1323–1330. 7

[65] GREENDYKE, R. & GNOFFO, P.A. (1995). Convective and radiative heating for vehicle return from the moon and mars. *NASA-95-TM-110185*. 7

[66] GUPTA, N.R., YOS, J.M., THOMPSON, R.A. & LEE, K. (1990). A review of reactions rates and thermodynamic and transport properties for an 11-species air model for chemical and thermal nonequilibrium calculations to 30000k. Tech. rep., NASA refernce publication 1232. 24, 25, 30, 32, 153

[67] HALPERN, B. & ROSNER, D. (1982). Incomplete energy accomadation at catalytic surfaces. *Hetrogeneous Atmospheric Chemistry, Geophysical Monograph Series*, **Vol. 26**, pp. 167–171. 6

[68] HARDY, G.B. (1979). Space shuttle solid rocket booster. *AAS paper 79-274; Annual Meeting, Los Angeles, CA, Oct. 29-Nov. 1, 9790101*. 124

[69] HARLE, C., CAREY, G.F. & VARGHESE, P.L. (2000). Analysis of high speed non-equilibrium chemically reacting gas flows. part ii. a finite volume/finite element model and numerical studies. *International Journal for Numerical Methods in Fluids*, **Vol. 32**, pp 691–709. 157

[70] HARTEN, A., ENGQUIST, B., OSHER, S. & CHAKRAVARTHY, S. (1987). Uniformly high order accurate essentially non-oscillatory schemes. *J. Comput. Phys*, **Vol. 71**, pp. 231–303. 8

[71] HARTEN, A., ENGQUIST, B., OSHER, S. & CHAKRAVARTHY, S. (1987). Uniformly high order accurate essentially non-oscillatory schemes iii. *Journal of Computational Physics*, **71**, 231âĂŞ303. 51

[72] HARTUNG, L.C. (June 1991). Development of a nonequilibrium radiative heating prediction method for coupled flowfield solutions. Tech. Rep. AIAA 91-1406, AIAA. 7

[73] HARVEY, J.K., HOLDEN, M.S. & WADHAMS, T.P. (2001). Code validation study of laminar shock/boundary layer and shock/shock interaction hypersonic flow part b: Comparison with navier-stokes and dsmc solutions. Tech. Rep. AIAA 2001-1031, AIAA. 7

[74] HENRICK, A.K., ASLAM, T.D. & POWERS, J.M. (2005). Mapped weighted essentially non-oscillatory schemes: Achieving optimal order near critical points. *Journal of Computational Physics*, **Vol. 207**, pp 542âĂŞ567. 8, 50

[75] HILLIER, R. (2007). Shock-wave/expansion-wave interactions and the transition between regular and mach reflection. *J FLUID MECH*, **Vol 575, ISSN:0022-1120(doi)**, Pages:399–424. 7

[76] HIRSCHEL, E.H. (2005). *Basics of Aerothermodynamics*. Springer, New York. 3, 123

[77] HO, W., KOO, J., BRUNS, M.C. & EZEKOYE, O.A. (2007). A review of numerical and experimental characterization of thermal protection materials part iii. experimental testing. *AIAA paper 2007-5773*. 124

[78] HOLDEN, M. & WADHAMS, T.P. (2003). A database of aerothermal measurements in hypersonic flow in "building block" experiments for cfd validation. In *AIAA Paper 2003-1137*, Jan. 2003. 7, 135

[79] HOLDEN, M. & WADHAMS, T.P. (2003). A review of experimental studies for dsmc and navierstokes code validation in laminar regions of shock/shock and shock/boundary layer interaction including real gas effects in hypervelocity flows. *AIAA Paper 2003-3641*. 7, 92, 94, 104

[80] HOLDEN, M. & WADHAMS, T.P. (2006). Comparisons between measurements in regions of laminar shock wave boundary layer interaction in hypersonic flows with navier-stokes and dsmc solutions. In *RTO-TR-AVT-007-V3*, NATO Research and Technology Organisation. 7, 106

[81] HOLDEN, M.S. & WADHAMS, T.P. (2001). Code validation study of laminar shock/boundary layer and shock/shock interaction hypersonic flow part a: Experimental measurements. Tech. Rep. AIAA 2001-1031, AIAA. 7, 92

[82] HUANG, J., LIN, H. & YANG, J. (2009). Implicit preconditioned WENO scheme for steady viscous flow computation. *Journal of Computational Physics*, **Vol. 228**, pp 420–438. 64

[83] INGER, G. & MOS, J. (2008). Comparison of navier-stokes and dsmc prediction at speparation and reattachment. *AIAA Paper 2008-3892*. 7, 11, 93

[84] IVINGS, M.J., CAUSON, D.M. & TORO, E.F. (1998). On riemann solvers for compressible liquids. *International Journal for Numerical Methods in Fluids*, **28**, 395–418, cited By (since 1996): 10. 7, 51, 52, 53

[85] JIANG, G.S. & SHU, C.W. (1996). Efficient implementation of weighted eno schemes. *Journal of Computational Physics*, **Vol. 126**, pp 202–228. 8

[86] JONES, J.H. (1964). Pressure tests on the standard hypervelocity ballistic model hb-2 at mach 1.5 to 5. *von Karman Institute, AEDC-TDR-64-246*. 7, 12

[87] JONES, J.H. (November 1964). Pressure tests on the standard hypervelocity ballistic model hb-2 at mach 1.5 to 5. *von Karman Institute, AEDC-TDR-64-246*. 12, 64

[88] KARA, K., BALAKUMAR, P. & KANDIL, O.A. (2007). Effects of nose bluntness on stability of hypersonic boundary layers over a blunt cone. *AIAA Paper 2007-4492*. 8, 54

[89] KARA, K., BALAKUMAR, P. & KANDIL, O.A. (2007). Receptivity of hypersonic boundary layers due to acoustic disturbances over blunt cone. *AIAA Paper AIAA 2007-947*. 8

[90] KENDALL, R.M. & RINDAL, R.A. (June 1968). An analysis of the chemically reacting boundary layer and charring ablator. part v a general approach to the thermochemical solution of mixed equilibrium nonequilibrium, homogeneous or hetrogeneous systems. *NASA Paper CR-1064*. 125

[91] KIM, S., KIM, C. & RHO, O.H. (2001). Multigrid algorithm for computing hypersonic, chemically reacting flows. **Vol. 38(6)**, pp 856–874. 8, 54

[92] KIMMEL, N.A. (1984). Alternate nozzle ablative materials program. *NASA-CR-175658, JPL-PUB-84-58, NSA 1.26:175858, 19840901*. 124

[93] KNIGHT., D. (2000). Rto wg 10 : Test cases for cfd validation of hypersonic flight. *40th AIAA Aerospace Sciences, AIAA Paper 2002-0433*. 10, 12, 92

[94] KNIGHT, D. & LONGO, J. (2010). Assessment of aerothermodynamic flight prediction tools for shock interactions. *48th AIAA Aerospace Sciences Meeting and Exhibit, 4-7 January 2010, Orlando, FL, AIAA Paper 2010-1465*. xv, 92, 104, 106, 111, 117

[95] KOLGAN, V. (1972). Application of the minimum-derivative principle in the construction of finite-difference schemes for numerical analysis of discontinuous solutions in gas dynamics. *Transactions of the Central Aerohydrodynamics Institute,*, **Vol 3 (6)**, pp 68–77. 47

[96] KONTIS, K. (2007). Hypersonc induced interactions of plasma and non-plasma jets. *AFOSR Joint Program Review*, pp 6. 5. 7

[97] KONTIS, K., QIN, N., STOLLERY, J. & EDWARDS, J. (2000). Hypersonic performance of a lifting elliptic cone with and without strakes. *Journal of Spacecraft and Rockets*, **Vol.37 (1) ,ISSN 0022-4650**, pp21–27. 7

[98] KOO, J., HO, M. & EZEKOYE, O. (2006). A review of numerical and experimental characterization of thermal protection materials part i. numerical modeling. Tech. rep., American Institute of Aeronautics and Astronautics, AIAA Paper 2006-4936. 124, 125

[99] KOO, J.H., MILLER, M.J., LIN, S. & SCHNEIDER, M.E. (1992). A cost-effective approach to evaluate high-temperature ablatives for military applications. *Naval Engineers Journal*, **Vol.104(3)**, pp 166–177. 124

[100] KUCHI-ISHI, S., WATANBE, S., NAGAI, S., TSUDA, S., KOYAMA, T., HIRABAYASHI, N., SEKINE, H. & HOZUMI, K. (March 2005). Comparative force/heat flux measurement between jaxa hypersonic test facilities using standard model hb-2 (part 1: 1.27 m hypersonic wind tunnel results). *JAXA Research and Development, Rept. JAXA-RR-04-035E*. 67

[101] KUCHIISHI, S., WATANBE, S., NAGAI, S., S.TSUDA, KOYAMA, T., HIRABAYASHI, N., SEKINE, H. & HOZUMI, K. (March. 2006.). Comparative force/heat flux measurment between jaxa hypersonic test facilites using standard model hb-2 (part 2: High enthalpy shock tunnel results). *Japanese Aerospace Exploration Agency, Research and Development Report,*, **XA-RR-05-030E**. 64, 67, 73

[102] LANE, J.G. & SALMASSY, O.K. (1993). An evaluation of ablative materials for a lunar transfer vehicle aerobrake. *AIAA Paper 93-2791*. 124

[103] LANEY, C.B. (1998). *Computational Gasdynamics*. Cambridge University Press. 8, 44, 45, 51, 52, 53

[104] LEBEL, P.J. & RUSSELL III, J.M. (1965). Development of ablation sensors for advanced reentry vehicles. *20th Annual ISA Conference and Exhibit, Los Angeles, CA, Oct. 4-7*. 124

[105] LEVIN, D.A., CANDLER, G.V., COLLINS, R.J., ERDMAN, P.W. & ZIPF, E.C. (1994). Examination of theory for bow shock ultraviolet rocket experiments - i. *Journal of thermophysics and heat transfer*, **Vol.8(3)**, pp 447–452. 7

[106] LIU, G.N.K. (1973). *High Temperature Oxidation of Graphite by a Dissociated Oxygen Beam*. Ph.D. thesis, PhD Thesis, Massachusetts Institute of Technology, Department of Aeronautics and Astronautics. 126

[107] LIU, X., OSHER, S. & CHAN, T. (1994). Weighted essentially non-oscillatory scheme. *Journal of Computational Physics*, **Vol. 110**, pp 200–212. 8, 45, 50

[108] LONGO, J. (2005). Modelling of hypersonic flow phenomena. *NATO Paper RTO,RTO-EN-AVT-116*. 3

[109] LONGO, M.A.J. (2003). Aerothermodynamics a critical review at dlr. *Aerospace Science and Technology*, **7(6)**, 429–438. 104

[110] LUNDELL, W.R.M.J.J.W., J. H. (1964). Experimental investigation of a charring ablative material exposed to combined convective and radiative heating in oxidizing and non-oxidizing environments. *NASA-TM-X-54797, 19640101*. 7, 124

[111] McWhorter, B.B., Ewing, M.E., Bolton, D.E., Albrechtsen, K.U., Earnest, T.E., Noble, T.C. & Longaker, M. (2003). Real-time inhibitor recession measurements in two space shuttle reusable solid rocket motors. *AIAA 2003-5107, July 2003*. 124

[112] Milos, F.S. & Rasky, D.J. (1994). Review of numerical procedures for computational surface thermochemistry. *Journal of Thermophysics and Heat Transfer*, **Vol.8(1)**. 6, 29

[113] Milos, S.F. & Rasky, J.D. (Jan - March 1994). Review of numerical procedures for computational surface thermochemistry. *Journal of thermophysics and heat transfer*, **Vol. 8**, pp 24–34. 124, 125

[114] Mosedale, A. & Drikakis, D. (2007). Assessment of very high-order of accuracy in les models. *ASME Journal of Fluids Engineering*, **Vol.129 (12)**, pp 1497–1503. 50

[115] Mosedale, A.D. (2009). Modelling shock-induced instabilites, transition and turbulent mixing using high-order methods. *PhD Thesis, University of Cranfield*. 93

[116] Nagamatsu, H.T., Myrabo, L.N., Messitt, D.G. & Sheer, R.E.J. (2005). Summary of theoretical, experimental, and computational investigation of flow over flat plate to mach 25. Tech. rep., AIAA Paper 2005-506. 7

[117] Nasuti, F., Barbato, M. & Bruno, C. (1996). Material-dependent catalytic recombination modeling for hypersonic flows. *Journal of thermophysics and heat transfer*, **Vol. 10(1)**, pp 131. 6, 123

[118] Neumann, M., Tiyyagura, S., Wall, W. & Ramm, E. (2006). Robustness and efficiency aspects for computational fluid structure interaction. *Computational Science and High Performance Computing: Notes on Numerical Fluid Mechanics and Multidisciplinary Design*, **91/2006**, 99–114. 88

[119] Nompelis, I. (2004). *Computational Study of Hypersonic Double-cone Experiments for Code Validation*. Ph.D. thesis, University of Minnesota. 8, 10, 11, 12, 54, 93, 94

[120] Nompelis, I. & Candler, G.V. (2009). Numerical investigation of double-cone flows with high enthalpy effects. *The 6th European Symposium on Aerothermodynamics for Space Vehicles, SP-659*. 106

[121] NOMPELIS, I., CANDLER, G.V. & HOLDEN, M.S. (2003). Effect of vibrational nonequilibrium on hypersonic double-cone experiments. *AIAA Journal*, **Vol. 41(11)**, pp 2162–2169. 11

[122] NOMPELIS, I., CANDLER, G.V., HOLDEN, M.S. & WADHAMS, T.P. (2003). Computational investigation of hypersonic viscous/inviscid interactions in high enthalpy flows. 11

[123] NOMPELIS, I., CANDLER, G.V., MACLEAN, M., WADHAMS, T.P. & HOLDEN, M.S. (2005). Numerical investigation of high enthalpy chemistry on hypersonic double-cone experiments. *AIAA Paper 2005-0584*. 7, 11, 94

[124] OLEJNICZAK, J., CANDLER, G.V., WRIGHT, M.J., LEYVA, I. & HORNUNG, H.G. (1999). Experimental and computational study of high enthalpy double-wedge flows. *Journal of Thermophysics and Heat Transfer*, **Vol. 13(4)**, pp 431–440. 7

[125] OLIVEIRA, M., XIE, P., SU, J. & LIU, C. (2008). Modified weighted compact scheme for shock-boundary layer interaction and double cone. *AIAA Paper 2008-755*. 8, 9, 45

[126] ORAN, E. (1995). Aerothermochemistry for hypersonic technology-computational fluid dynamics and chemistry modeling. *von Karmen Institute for Fluid Dynamic, LS-1995-04*. 3

[127] PARK, C. (1985). *Calculation of Nonequilibrium Radiation in the Flight Regimes of Aeroassisted Orbital Transfer Vehicles*, vol. 96 of *Thermal Design of Aeroassisted Orbital Transfer Vehicles*, 395–418. AIAA, New York, progress in aeronautics and astronautics edn. 30, 154

[128] PARK, C. (1990). *Nonequilibrium Hypersonic Aerothermodynamics*. Wiley. 5, 7, 17, 27, 30, 32, 94, 154

[129] PARK, C. (1995). Aerothermochemistry for hypersonic technology- experimetal simulation and evaluation of chemical effects. *von Karman Institute, LS-1995-04*. 4, 7

[130] PARK, C. (July-September 2007). Numerical implementation of surface catalysis reaction, and sublimation. *Journal of Thermophysics and Heat Transfer*, **Vol. 7(3)**, pp 385–398. 6

[131] PARK, C. & MILOS, F.S. (January 1990). Computational equations for radiating and ablating shock layers. Tech. rep., AIAA Paper 90-0356. 6, 120

[132] PATIL, M., SWAMINATHAN, S. & MANDAL, J. (2006). Hypersonic viscous flow computations using energy relaxation method. *AIAA Paper 2006-583*. 7, 52

[133] PATIL, M., MANDAL, J. & SWAMINATHAN, S. (2007). Energy relaxation method for chemical non-equilibrium flow. *International Journal for Numerical Methods in Fluids*, **Vol. 54 (12)**, pp 1473 – 1494. 7, 52

[134] PETERSON, D.A. & MEYER, C.L. (1966). Experimental evaluation of several ablative materials as nozzle sections of a storable-propellant rocket engine. *NAS-TM-X-1223, 19660401*. 124

[135] QIU, J. & SHU, C. (2002). On the construction, comparison and local characteristic decomposition for high-order central WENO schemes. *Journal of Computational Physics*, **183**, pp 187–202. 46

[136] RANUZZI, G., GRASSO, F. & BISCEGLIA, S. (2005). Effects of the surface catalysis on high-enthalpy shock- wave/turbulent boundary- layer interactions. *AIAA Paper 2005-3219*. 6

[137] RUDY, D.H., THOMAS, J.L., KUMAR, A., GNOFFO, P.A. & CHAKRAVARTHY, S.R. (July 1991). Computation of laminar hypersonic compression-corner flows. *AIAA Journal*, **Vol 29 (7)**, pp 1108–1113. 6

[138] SARMA, G.S.R. (2000). Physico-chemical modelling in hypersonic flow simulation. *Progress in Aerospace Sciences*, **Vol 36 (3-4)**, pp 281–349. 3, 4, 5, 7, 94, 120, 121, 123

[139] SAXENA, S. & NAIR, M. (2005). An improved roe scheme for real gas flows. *AIAA Paper 2005-587*. 7, 52

[140] SCHNEIDER, S. (2001). Hypersonic laminar instability on round cones near zero angle of attack. *AIAA Paper 2001-0206*. 7

[141] SCOTT, C.D. (1980). Catalytic recombination of nitrogen and oxygen on high temperature reusable surface insulation. In edited by A.L. Crosbie, ed., *Progress in Astronautics and Aeronautics*, vol. 77, pp. 193–212, AIAA, New York. 5

[142] STEWART, D., J.V.RAKICH & LANFRANCO, M. (1982). Catalytic surface effects experiments on the space shuttle. vol. 82, pp. 248–272, AIAA, New York. 6

[143] STOLLERY, J. & C.PARK (1964). Computer solutions to the problem of vibrational relaxation in hypersonic nozzle flows. *Journal of Fluid Mechanics*, **Vol. 19, part 1**, pp. 113–123. 3

[144] TCHUEN, G., BURTSCHELL, Y. & DAVID, E.Z. (2005). Numerical study of non-equilibrium weakly ionized air flow past blunt bodies. *International Journal of Numerical Methods for Heat and Fluid Flow*, **Vol 15(5/6)**, pp 588–609. 8, 45

[145] THOMPSON, E., HENRY, K. & WILLIAMS, L. (June 20, 2005, viewed 6 May, 2009). It's official. X – 43A raises the bar to mach 9.6, media release, the HYPER-X program, nasa's aeronautics research mission directorate. http://www.nasa.gov/missions/research/x43-main.html. 2

[146] THORNBER, B. (2007). *Implicit Large Eddy Simulation For Unsteady Multi-Component Compressible Turbulent Flows*. Ph.D. thesis, University of Cranfield. 48

[147] TISSERA, S. & DRIKAKIS, D. (2010). Computational fluid dynamics methods for hypersonic flow around blunted-cones-cylider-flare. *Journal of Spacecrafts and Rockets*, **In print**. 64, 93, 104, 147

[148] TISSERA, S., TITAREV, T. & DRIKAKIS, D. (2010). Chemically reacting flows around a double-cone, including ablation effects. *AIAA Paper 2010-1285*. 120

[149] TISSERA, S., TITAREV, V. & DRIKAKIS, D. (2010). Real gas hypersonic flow modeling using high order methods. *Journal of Spacecrafts and Rockets*, **In Review**. 92, 104

[150] TITAREV, V.A. & TORO, E.F. (2004). Finite-volume WENO schemes for three-dimensional conservation laws. *Journal of Computational Physics*, **Vol. 201**, pp 238–260. 8, 46, 51

[151] TORO, E.F. (1999). *Riemann Solvers and Numerical Methods for Fluid Dynamics a Practical Introduction*. Springer-Verlag, Berlin. 46, 52, 53

[152] VAN LEER, B. (1979). Towards the ultimate conservative difference scheme.iv. a new approach to numerical convection. *J. Comput.Phys.*, **Vol. 23**, pp 276–299. 47

[153] VANCRAYENEST, B. & FLETCHER, D.G. (2005). Investigation of the thermochemistry of ablation of graphite for planetary entry applications. *AIAA Paper 2005-5062*. 124

[154] VINCENTI, W. & C.H. KRUGER, J. (1965). *Introduction to Physical Gas Dynamics*. Wiley, New York. 25

[155] VIVIANI, A. & PEZZELLA, G. (2007). Catalytic effects on non-equilibrium aerothermodynamics of a reentry vehicle. *AIAA Paper 2007-1211*. 6

[156] VOJVODICH, N.S. & WINKLER, E.L. (1963.). The influence of heat rating and test stream oxygen content of the insulation efficiency of charring materials. *American Institute of Aeronautics and Astronautics, NASA Paper TN D-1889*. 124

[157] WADHAMS, T.P. & HOLDEN, M. (2004). Summery of experimental studies for code validation in the lens facility with recent navier-stokes and dsmc solutions for two-and three dimensional separated regions in hypervelocity flows. In *AIAA Paper 2004-917*, Jan. 2004. 7, 94, 135

[158] WOLF, W.R. & AZEVEDO, J.L. (2006). Supersonic and hypersonic flow computations using higher-order non-oscillatory schemes. *AIAA Paper 2006-3169*. 8, 54

[159] ZHLUKTOV, S. & ABE, T. (1999.). Viscous shock layer simulation of airflow past ablating bunt body with carbon surface. *Journal of Thermophysics and Heat Transfer*, **Vol. 13 (1)**, pp 50–59. 6

[160] ZIEN, T.F. (2001). Thermal effects of particles on hypersonic ablation. *AIAA Paper 2001-2833*. 125

[161] ZIEN, T.F. (2004). Application of heat balance integral method to droplet freezing in melting ablation. *AIAA Paper 2004-167*. 125

[162] ZOLTAK, J. & DRIKAKIS, D. (1998). Hybrid upwind methods for the simulation of unsteady shock-wave diffraction over a cylinder. *Computer Methods in Applied Mechanics and Engineering*, **Vol. 162**, pp 165–185. 9, 41, 47, 76, 120